# DYNAMIC AGGREGATION AND DISPERSAL OF *ESCHERICHIA COLI* UNDER CYCLES OF FEAST AND FAMINE

BY

JASON MERRITT

DISSERTATION

Submitted in partial fulfillment of the requirements
for the degree of Doctor of Philosophy in Physics
in the Graduate College of the
University of Illinois at Urbana-Champaign, 2018

Urbana, Illinois

Doctoral Committee:

Assistant Professor James O'Dwyer, Chair
Assistant Professor Seppe Kuehn, Director of Research
Assistant Professor Thomas Kuhlman
Professor Nigel Goldenfeld
Associate Professor Rachel Whitaker

# Abstract

Microbes in nature are constantly subject to environmental fluctuations on varying timescales, and have developed a host of strategies for dealing with environmental stress. In particular, variation in nutrient levels is believed to impact community function and drive a dynamic equilibrium between planktonic and aggregated microbial populations in liquid environments. Although models of population dynamics cannot be adequately designed or tested in the absence of precise quantitative data, experiments quantitatively documenting the dynamics of large microbial populations in response to fluctuating environments with high-frequency measurement over long timescales are rare, with most studies relying on non-quantitative measurement techniques, measurements with low temporal resolution, or small population sizes.

We develop a custom continuous-culture device coupled to an epifluorescence microscope, permitting high-throughput ($> 10^7$ objects per system per experiment) quantitative fluorescence measurements of macroscopic populations of bacteria at the single-cell level with measurements as frequent as once per minute. Our design is stable over many weeks of operation and has fully automated control allowing us to perturb bacterial communities and measure the resulting dynamics. We find that populations of *Escherichia coli* propagated at slow but non-zero growth form large, free-floating cell aggregates, and that subjecting these populations to cycles of nutrient abundance (feast) and scarcity (famine) results in history-dependent dynamics whereby the planktonic populations appear to achieve increasing resilience to perturbation, as measured by the maximum apparent growth rate during periods of feast. By varying the frequency and amplitude of feasts we find a strong dependence of the maximum planktonic growth rate on both variables.

We find that these transiently high planktonic population growth rates do not result from cell division, but from patterns of aggregation and dispersal from aggre-

gated populations of *E. coli* which exhibit both history-dependence and sensitivity to nutrient levels. We present a simple model that accurately describes the majority of our data in terms of these aggregation dynamics, and confirm the model with measurements of aggregate sizes and control experiments in conditions similar to batch culture, in which aggregates do not form. We present additional results demonstrating a history-dependent effect whereby the lag phase of individual cells decreases with increasing amplitude or frequency of feasts.

Finally, we briefly present work involving modification of our custom continuous-culture devices to enable future experiments in our lab examining the dynamics of complex phototroph-heterotroph communities exhibiting fluorescence in multiple channels.

# Acknowledgements

I'd like to thank Professor Seppe Kuehn, my adviser and the lead researcher of our lab, for all his support and guidance over the years, and for the seemingly endless energy he has poured into ensuring the success not only of this project but the lab as a whole. I have never had the pleasure of working with anyone so dedicated to science, enthusiastic about the particulars of each project, or personally encouraging during even the most challenging periods of research. No one could ask for a better mentor or PI, and I'm proud to be the first doctoral student he graduates. I wish him the best as the lab continues to mature into the fantastic research group it deserves to be, and hope that all the future students lucky enough to come through this lab make the most of their opportunity.

I would also like to give particular appreciation to my labmates David T. Fraebel and Harry Mickalide for all their hard work over the years. We built this lab together, and even independent of specific contributions, none of our research - mine or anyone else's - would have been possible without them. I wish them easy graduations and smooth transitions into whatever projects or careers they choose next.

I'd like to thank all the members of my committee - Professors James O'Dwyer, Thomas Kuhlman, Nigel Goldenfeld, Rachel Whitaker, and Seppe Kuehn - for useful advice and for generously donating their time to carefully consider my research and attend a defense outside of the regular academic term. I'd also like to thank Professor Thomas Kuhlman for generously allowing me space in his lab early on, when our own was still months away from finishing construction. Much of what I know about biological experimental technique was learned from his students during that time.

A significant number of researchers have made direct, personal contributions to the work presented in this dissertation. Beyond conceiving the project and direction

This material is based upon work supported by the National Science Foundation under Grant Nos. PHY 0822613 and PHY 1430124.

of research and making himself constantly available for discussion, my adviser Professor Seppe Kuehn developed the model of aggregation presented here, and made key contributions throughout the prototyping of our continuous-culture systems, from explanations of experimental technique to familiarity with vendors of critically important components. Our systems would not be nearly as robust or impressive without his guidance. I thank David T. Fraebel for the use of agar plate imaging setups he designed and constructed with the help of a former undergraduate member of our lab, Diane Schnitkey. Harry Mickalide is solely responsible for finding and designing a way to modify our hardware for culturing photosynthetic organisms, and was immensely helpful throughout the process of upgrading my systems to match his designs. Kaumudi Prabhakara worked with me to find a way to adapt our microscopes for multiple-color fluoresecence imaging. Husayin Tas provided a key insight regarding liquid flow design early on, and an undergraduate briefly in our lab, Joseph Varikooty, made the rpm meter used to calibrate our stir plates. Additional contributions to this project were less specific, but no less useful, and I'd like to thank my current and former labmates Karna Gowda, Connie Phong, Chandana Gopalakrishnappa, Luis Miguel de Jesús Astacio, Derek Ping, and Daniel Grober, as well as current and former Kuhlman Lab members Nick Sherer and Hyuneil Kim, for insightful discussions, suggestions, and support.

While the number of non-faculty UIUC employees supporting this research is far too vast to list here, I would like to thank a small number whose contributions stood out in particular. Staff Clerk Cheryl Sabas is by far the fastest and most efficient purchaser I have ever worked with, and without her tireless work early on when I was submitting new orders at times every day when prototyping, my project easily could have been delayed by months. Throughout her tenure here, former CPLC Administrative Assistant Sandra Patterson provided critical support in guiding me and our lab through university systems, bureaucracy, and travel arrangements for conferences. Physics/MRL Research Lab Shop Supervisor Ernest Northen taught me all the machining skills needed to construct my systems, and was always available with creative solutions and assistance when I was stuck. Visiting CPLC Laboratory Coordinator Elizabeth Ujhelyi's help in recent years has ensured our lab has working equipment and enabled members of our lab to focus on science. Last but not least,

Physics Administrative Aide Wendy Wimmer has been an invaluable resource as my time at the university has come to a close, and is in part responsible for ensuring I graduate without losing my head.

I'd like to thank Rabbi Dovid Tiechtel of Illini Chabad for working to create a welcoming atmosphere and for his work supporting Jewish life on campus.

Finally, I'd like to thank my wonderful, loving parents, Jack and Janice Merritt, grandparents Charles and JoAnn Merritt, grandmother Carol Witt, and my dear departed grandfather Bernard Witt *z"l*. Without all of your examples, guidance, and support, not only would this project not have been possible, I wouldn't have made it here in the first place. Thank you all so much for everything, and for being so understanding when I've been busy. I'd also like to thank my sister Rachel Kelly for being so supportive and for inspiring me to work harder. I wish I had been able to visit all of you more often over the years, and I hope to see everyone soon.

*To my parents*

# Table of Contents

# Chapter 1

# Introduction

Microbial communities in nature are constantly subject to environmental fluctuations over a wide range of timescales [1, 2], from seconds to days, months, or even years. These fluctuations may be regular and predictable, such as varying water levels in intertidal zones [3], varying temperatures and light levels over the course of a day [4], or longer-term patterns such as weather and temperature cycles over the course of months [5, 6]. They also include perturbations which may be sudden, dramatic, or unpredictable, such as the rapid inflow of nutrients or toxins into a local ecosystem [7] or competitive invasion by a foreign species [8]. As a result, natural organisms have evolved a wide range of strategies to maximize their chances for survival in changing environments. Large perturbations such as nutrient pulses are also known to impact community function and structure [9], but little quantitative data exists exploring precisely how such perturbations drive population responses, particularly when the response is history-dependent [10]. In this work, we use cyclic perturbations (feast-famine cycles) in continuous-culture to explore the amplitude- and frequency-dependent population dynamics and community structure of *Escherichia coli*.

## 1.1 Fluctuating environments

Even in a controlled laboratory setting, fully eliminating environmental fluctuations is nearly impossible. For example, common techniques for propagation of microbial species include growth on plates, in batch culture, and in constant-flow continuous-culture devices (chemostats). Growth on plates and batch culture necessarily involves nutrient depletion as the direct result of microbial feeding and reproduction, ultimately triggering stress responses [11] and eventually starvation [12]. The degree of the environmental change experienced is magnified in the presence of multiple

substrates for growth, such as the presence at inconsistent concentrations of the many amino acids in the commonly used lysogeny broth (LB) growth medium, as microbial populations deal not only with time-varying nutrient concentrations, but also changes in the metabolic machinery required to process different substrates or metabolites [13,14]. While constant-flow continuous-culture conditions mitigate these effects, experiments have demonstrated that even clonal populations rapidly differentiate into subpopulations with competitive advantages over the initiating strain [11] or distinct ecological niches [15]. To the extent that new strains and subpopulations modify their own environment [15], the long-term maintenance of constant chemical or environmental conditions is not possible even in chemostats.

A large body of research studying these effects already exists. Specifically in LB growth medium, the order in which *E. coli* preferentially consumes different substrates is known [16], and a larger, more general body of work examines bacterial stress response [17, 18], the basic biological parameters determining growth rates [19, 20], and commonly observed effects, such as the existence of lag phase, resulting from successive growth in nutrient-limited and nutrient-rich conditions [21, 22]. As mentioned above, numerous studies exist characterizing long-term mutation and differentiation in chemostats. However, because fluctuations in these conditions are driven in large part by microbial growth or are otherwise poorly controlled, such studies cannot always fully characterize the response of microbial populations in response to externally-imposed fluctutations. For example, the existence of a lag phase in growth of *E. coli* under diauxie on growth medium containing both glucose and lactose has long been known [14]. However, more recent work by Lambert and Kussell with direct, externally-imposed control over environmental fluctuations has demonstrated that this well-known effect disappears under conditions of nutrient cycling between glucose and lactose [23]. This work demonstrated phenotypic adaptation to the controlled fluctuating conditions, owing both to shorter-term dynamic 'memory' whereby regulatory networks continue to respond to experienced external stimuli for some time even after their removal, and to cross-generational effects where stable proteins created in response to the stimuli are passed on to daughter cells which have not directly experienced them. Fine external control over environmental parameters has therefore proven extremely valuable in characterizing and understanding microbial

responses to environmental fluctuation and perturbation.

Even where such control exists, however, previous work frequently focuses not on population-level strategy and response, but on phenomena over much shorter or much longer timescales. For example, the immediate response of of microbes or genetic networks in response to perturbation may be considered - common in studies of chemotaxis [24], where decisions occur on the timescale of seconds. Alternatively, other work often focuses specifically on evolution under conditions of environmental fluctuation; for example, Richard Lenski has done work characterizing the fitness of strains of *E. coli* evolved for 2000 generations under daily alternating temperature conditions [25]. This work successfully demonstrated the long-term evolution of increased fitness over the ancestral strain at both alternated temperatures [26]; however, no data characterizing the populations exists for timescales below one day, and relative fitnesses could only be assessed via direct competition and plating. In such experiments, while potentially interesting population-level response occurs, the lack of instrumentation recording it, and the fact that data which was recorded may be incomplete or non-quantitative, means the population dynamics frequently either cannot be adequately understood or even studied at all. As a result, commonly-used models of populations in continuous-culture conditions frequently neglect history-dependent effects and are generally inadequate for accurately predicting community dynamics and behavior outside of steady-state conditions [10]. High-resolution quantitative data is therefore expected to help improve our models of population dynamics in fluctuating systems [27].

## 1.2 Microbial response to environmental fluctuation

Microbes have a wide array of strategies for dealing with stress and environmental perturbations, ranging from individual-level responses [23, 28, 29] to environmental change to strategies with greater advantages at the population level, such as bet-hedging [30]. In general, predicting the population response to changes is difficult; for example, the *rpoS* stress response network in *E. coli* affects processes throughout the cell, and the result of the interplay between this general response and the physical or chemical changes brought on by specific changes in the environment is

not obvious [17, 18]. In some species it is also theoretically possible that an artificial environmental change could trigger a specific evolved response irrelevant to the laboratory environment. Furthermore, some of the better understood microbial responses, such as those governing chemotaxis [31], are unlikely to be relevant in our particular study, due to rapid mixing in our experiments eliminating clear nutrient gradients. However, regardless of the sometimes opaque underlying mechanics, a number of microbial behaviors possibly relevant to nutrient-level perturbations are common across many species and have plausible explanations.

For example, lag phase, the delay in growth of microbial species upon introduction to nutrients, is well-studied though not fully understood. A phenomenological model developed by Baranyi [32], positing lag phase as a waiting period for cells to accumulate or produce sufficient amounts of an unknown critical substance limiting growth, has proved useful in various contexts and can be modified easily to accord with the observation that duration of lag phase is correlated with the duration of starvation [21]. Work also exists suggesting that lag phase following prolonged starvation - and a concomitant reduction in cell size - has to do with the accumulation of biomass [22], and evidence that bacterial cells must reach a certain ribosome-protein ratio to achieve steady-state growth [19, 20] but inactivate and degrade ribosomes during slow growth and starvation [33, 34] provides a possible mechanism. As a result, various lag-related effects may be expected to impact bacterial growth under fluctuating nutrient conditions.

Phenotypic switching may also be expected to be relevant. For example, 'persisters' - slow-growing, near-dormant cells which show enhanced resistance to environmental stressors such as antibiotics and can stochastically revert to 'normalcy' - are known to occur at 100- to 1000-fold higher abundance in stationary-phase cultures [35], and therefore may be expected to be more prevalent in general under conditions of nutrient deprivation [30, 36, 37]. Because persisters grow little if at all, high abundances of persisters could theoretically confound population-level growth rate measurements due to the difficulty in quickly distinguishing a subpopulation of persisters from normal cells without destructive or invasive treatment. Separately, changes in the population supporting more rapid switching between phenotypic states suited either for feast or famine conditions could increase population resilience to fluc-

tuations, as was demonstrated in the case of glucose-lactose nutrient cycling [23].

Finally, cellular aggregation may be expected to play an important role in population-level responses. Microbes, including *E. coli*, are known to commonly aggregate both into free-floating cell assemblages [38] and dense biofilms [39]. While cells in biofilms, like persisters, tend to grow slowly and resemble stationary-phase cells [40], they are also shielded from a variety of environmental stressors [41] and may benefit from various cellular products, such as metabolites, excreted from neighboring cells [42]. In continuous-culture systems, or any system where microbial washout can occur - including the mammalian gut that serves as one of *E. coli*'s natural habitats [1] - biofilm formation can also provide a selective advantage by allowing cells to avoid washout and remain near food sources. As a result, selection for biofilm formation is a known consequence of long-term chemostat operation [43, 44]. However, in *Vibrio cholerae*, recent work has demonstrated that while strains which constitutively form biofilm have a competitive advantage on surfaces over strains which can regulate biofilm production, under perturbations which vary nutrient flow and seed new environments with the planktonic component of an old environment - conditions intended to simulate the natural environment of *Vibrio* - wild-type strains which are plastic in their ability to form biofilm retain a competitive advantage over constitutive biofilm producers [45]. As *E. coli* also experiences experiences sharply varying nutrient concentrations in the mammalian gut and also faces potential disturbance and introduction to new environments [1], plasticity in biofilm production can also be expected to play a significant role early on in *E. coli* continuous-culture population dynamics under nutrient variation, although the specific response we ultimately observe in *E. coli* - aggregation in response to nutrient deprivation - is the opposite of the strategy employed by *Vibrio* [45]. More generally, it is believed that particulate nutrient concentrations, along with other environmental factors, may drive a dynamic equilibrium between planktonic and aggregated populations in natural ecosystems [46]. However, a lack of quantitative data characterizing the nature of this dynamic equilibrium renders modeling the exact relationship difficult, particularly as a dynamic response over short timescales.

## 1.3 History of continous-culture devices

In 1950, Novick and Szilard presented the first description of a chemostat [47] - a continuous-culture device designed to propagate bacteria indefinitely under constant chemical conditions by maintaining steady flow of fresh media into, and bacterial culture out of, a fixed volume. While most laboratory bacterial studies measure growth on a fixed supply of nutrients, such as plates or batch culture - possibly with successive inoculations into new plates or flasks, as in the Lenski long-term *E. coli* evolution experiment [48] - the continuous-culture experimental framework permits studying microbial growth and behavior under conditions that would be difficult or impossible to achieve in batch culture. As a result, the number of continuous-culture designs and their range of applications has increased dramatically since 1950, permitting not only the study of microbial populations under constant chemical conditions, but also under conditions of constant growth in a turbidostat [49], constant antibiotic inhibition in a morbidostat [50], or a host of other environments in continuous-culture chambers ranging in size from microfluidic devices [51, 52] to large bioreactors [53].

Due to the flexibility of continous-culture systems and an already long history of using real-time environmental feedback in response to measurements, the idea of perturbing microbial communities propagated in continuous-culture is not new. For example, microfluidic devices with nutrient switching have been used in targeted metabolic studies [23], and results-oriented civil engineering studies have used bioreactors to demonstrate variable nutrient loading schedules provide a selective advantage to the floc-forming bacteria used in wastewater treatment [53]. Continuous-culture propagation of photosynthetic organisms with artificial day/night cycles [54–56] represents one of the clearest and most common examples of cyclic perturbation of a continuous-culture system. Our own continuous-culture design differs from such existing designs primarily due to its measurement capabilities.

Most experiments in continuous-culture devices, especially those housing macroscopic populations, have long relied on measurement techniques which are non-quantitative or suffer from poor time resolution. For decades the primary method of measuring continuous-culture dynamics was manual sampling, followed by techniques like plating, filtration, or other techniques to estimate population abundance [57–59]. Manual sampling is labor-intensive and demands infrequent measurement - typically

on the timescale of many hours for long experiments [57], or tens of minutes for short, targeted measurements of specific events [58] - and is difficult to scale up to many systems. These techniques have been used to make long-term observations such as changes in the frequency of bacteriophage T5-resistant *E. coli* [15], and even some dynamical observations, such as apparent predator-prey cycles in *E. coli*-T4 communities [57] and the failure of the Monod equation for bacterial growth to adequately describe growth rates following nutrient up-shift in bioreactors [58]. However, the poor time resolution and high noise in these measurements makes predictive modeling of population dynamics difficult and interpretation of data ambiguous (see, for instance, Fig. 1 of Ref. [15]). More recently, fully online measurements have come into use, such as optical density measurement, now commonly used in systems with automatic feedback like turbidostats or the morbidostat developed in the Toprak lab [50, 60]. Optical density measurements allow rapid estimates of microbial density and growth rates and are therefore extremely useful - our own systems output a record of optical density - but are affected by a host of factors beyond actual population size, such as cell size and morphology. Critically, the spatial structure of the microbial population is likely to be either invisible to this measurement or difficult to separate out from the rest of the signal. Our own experiments found optical density measurement at constant planktonic cell density to be inconsistent over periods of days, and found the measurement to be strongly correlated during early growth to real abundances of planktonic cells, rather than the true population abundance, which includes cells in large free-floating cell aggregates which potentially make up more than half the biomass of our communities.

At the other end, existing continuous-culture designs that do permit quantitative measurement usually suffer from other drawbacks. For example, there has recently been a proliferation in advanced microfluidic continuous-culture designs, such as the 'mother machine' developed by the Jun lab [61] to observe an *E. coli* bacterium in a channel inheriting the old pole of its mother cell over hundreds of generations, the 'chemoflux' device used by Lambert and Kussell [23] to observe population dynamics under glucose-lactose nutrient cycling, and the chip-based bioreactor developed by the Quake lab [51] which enables the long-term observation of semicontinuous planktonic growth by using a complex system of valves and tubes to isolate and clean small

segments of biofilm. These designs permit observation of population dynamics at the single-cell level and have already been used to produce high-quality quantitative data; however, the microbial population size under consideration in microfluidic devices is orders of magnitude smaller than in a standard macro-scale chemostat or bacterial community in nature, may be subject to greater noise, and complex microfluidic devices - particularly those made from Polydimethylsiloxane (PDMS), which have a typical lifespan on the order of 50-100 hours - often suffer from aging effects. Other quantitative measurement techniques which do not rely on microfluidic devices also have downsides; for example, flow cytometry [62] is expensive and challenging to automate, and digital holography [63, 64] is computationally expensive and cannot separate fluorescently labeled strains.

Our own solution - custom, coupled epi-fluorescence microscopes - is cheap and straightforward enough to permit operating complete replicate systems in parallel, has the capacity to observe properties such as spatial structure and motility which can be invisible to other measurement techniques, and can readily be modified to support imaging of multiple fluorescent proteins at differing magnifications. Our design has proven robust to long-term operation over a period of many days or weeks, and is capable of automated high-throughput quantitative measurements at the single-cell level - with at least $10^7$ fluorescent objects directly imaged on average per system in each experiment - despite maintaining a macroscopic population of $\sim 10^9$ cells. Most importantly, it has allowed us to successfully investigate some of the questions raised in the preceding sections, including the nature of history-dependent population dynamics in cycles of feast and famine, and the impact of aggregated subpopulations on such dynamics as they undergo regular patterns of accumulation and dispersal.

## 1.4 Summary of contents

A brief outline of the structure of the dissertation follows. First, in Chapter 2, we present a detailed description of our continuous-culture systems, including the measurement capabilities of our continuous-culture devices and the specifications of our microscopes. We also provide an overview of the software powering our systems, and a description of the algorithms used to generate and analyze our abundance time

series. In Chapter 3, we introduce the washout event perturbation used in our experiments, and present results from a preliminary series of experiments designed to test the long-term stability of our systems under operation both under steady-state chemostat operation and feast-famine cycles with washout events. We demonstrate a history-dependent effect where the planktonic population's apparent resilience to washout from the system - as measured by its ability to rapidly recover - increases with the number of successive washout events, and show that both the onset and extent of aggregation in our systems is correlated to slow but non-zero growth. We also present the results of control experiments demonstrating that our measured planktonic abundances in the microscope are directly proportional to cell densities as measured by plating, and showing that the aggregation we observe does not depend on the mutations introduced in our strain or on the presence of the antibiotic used in our media. These experimental results and the bulk of the work presented in these chapters were first published in *Scientific Reports* in 2016 [65].

In Chapter 4, we present the main experimental work of this project - cyclic feast-famine experiments driving frequency- and amplitude-dependent population dynamics - demonstrating that apparent planktonic population growth rates far in excess of biologically plausible values in our media are caused by the presence and dispersal of aggregated populations of cells. We present a model of aggregation and dispersal which sufficiently explains the majority of our data through the accumulation and maturation of free-floating cell aggregates and biofilm during slow growth under famine conditions, coupled with the rapid dispersal of aggregated populations into planktonic cells under feast conditions. We confirm the predictions of this model by analyzing the size distributions of cell aggregates under different experimental conditions, and with control experiments under 'repeated batch culture' (basal dilution rate $D = 0$) conditions. The experimental results and model presented in this chapter were first published in *Physical Review Letters* in 2018 [66].

Finally, in Chapter 5, we outline the planned direction of future experiments, and briefly summarize the work done to expand the capabilities of our systems in anticipation of these experiments. We additionally include a number of detailed technical appendices intended to allow others to expand on our continous-culture designs and reliably reproduce our experimental results.

# Chapter 2

# Custom continuous-culture device

This chapter contains material from published work by Jason Merritt and Seppe Kuehn[1], used with permission of the authors.

This work was partially supported by the Center for the Physics of Living Cells, the National Science Foundation Physics Frontier Center (PHY 0822613 and PHY 1430124), the Carl R. Woese Institute for Genomic Biology, and the Department of Physics at the University of Illinois at Urbana-Champaign. The dissertation author was the primary experimental investigator of this work.

Contributions: Seppe Kuehn and Jason Merritt contributed to the design of the apparatus, and the analysis and interpretation of the experimental results. Jason Merritt constructed the apparatus and wrote the custom software used in the experiment.

Acknowledgements: Bacterial strain under study was created by Doeke Hekstra at Rockefeller University. Morbidostat design from Erdal Toprak's lab [60] provided inspiration for continuous-culture device design.

## 2.1 Introduction

To carry out experiments in fluctuating conditions, we constructed custom, low-cost continuous-culture devices capable of propagating macroscopic ($\sim 10^9$ cells) cultures of *E. coli* for periods of weeks while automatically sampling, imaging, and segmenting cells via a coupled epifluorescence microscope. As discussed in Section 1.3, the key advantage of these systems over existing designs is the ability to sustain long-term, high-throughput quantitative measurements of large populations at the level of single cells, while also being able to make observations of spatial structure in the form of

[1] Merritt, J and Kuehn, S. Quantitative high-throughput population dynamics in continuous-culture by automated microscopy. *Scientific Reports* **6**, 33173 (2016).

free-floating cell aggregates.

We present an overview of our continuous-culture design, followed by more detailed specifications of the custom hardware and software involved in running our experiments. We also provide details of the algorithms used in segmenting fluorescent cells in images taken by our microscopes, and automatically converting this data into time series. A detailed set of appendices at the end of the main text, referenced in this chapter, provide additional technical information needed to construct additional systems.

## 2.2 Overview of continuous-culture device

We constructed six replicate continuous-culture devices (Fig. 2.1(a)). Each system houses a 20 mL culture in a glass vial in a custom machined aluminum block. The continuous dilution of the culture is accomplished by two computer-controlled peristaltic pumps which add fresh media and remove organisms and spent media. The volume of the culture is fixed by the height of the outflow line relative to the bottom of the vial. The culture vial is in thermal contact with the aluminum block, which is temperature controlled via computer-controlled PID feedback to a thermoelectric heating-cooling element (Peltier). The optical density of the culture is monitored using an infrared light-emitting diode (LED) and photodetector mounted in the aluminum block. A magnetic stir bar and commercial inductive stir plate mix the culture.

During continuous-culture, a third peristaltic pump draws samples once per minute from the culture vial and passes it through a micron-scale glass capillary (Fig. 2.1(a)). A custom single-color epi-fluorescence microscope images cells as they pass through the capillary before being returned to the culture vial. Within the imaging volume, the sample is illuminated by filtered light from a high-power LED. The resulting fluorescence is captured by a 20x objective and imaged by a charge-coupled device (CCD) image sensor. We found glass capillaries connected directly to silicone tubing with medical epoxy to be far more robust than PDMS microfluidic devices. Metal extrusions supporting tubes that pass samples from the culture vial to the microscope were necessary to damp vibrations. Bubbles infiltrate our imaging line, but only transiently remain in the capillary and the system remains resilient to their presence

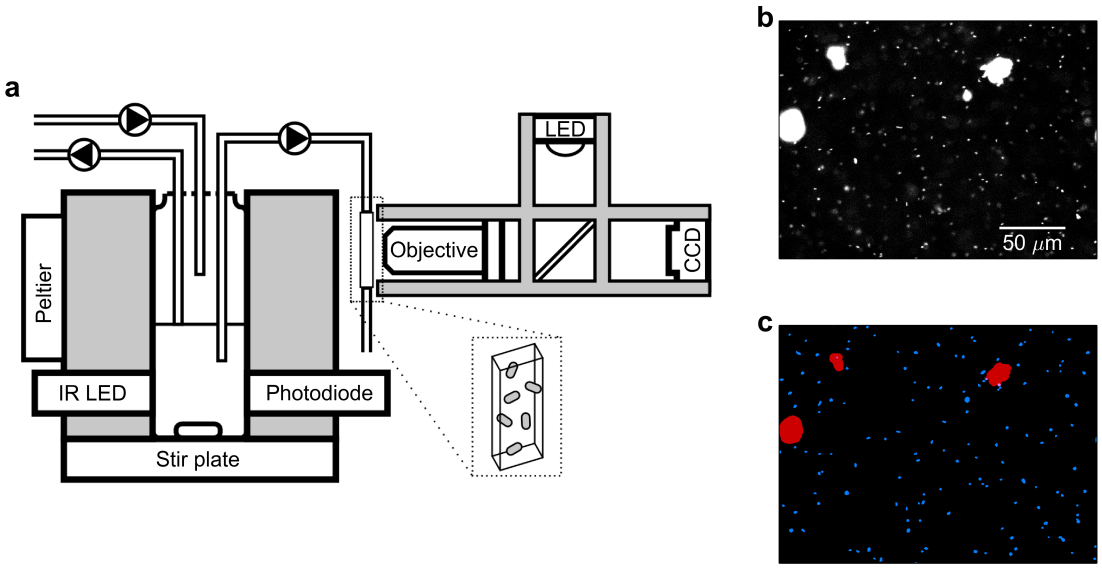


Figure 2.1: Microscope-coupled continuous-culture device. (a) Continuous-culture device and associated epi-fluorescence microscope. System temperature is set by a Peltier element and feedback to a thermometer (not shown), and optical density is measured by an infrared LED and photodiode in an absorbance geometry. The culture vial is stirred with an inductive stir plate, fed by a nutrient inflow line, and the culture volume is set by the outflow line. A separate microscope imaging line pumps culture samples into a thin rectangular glass capillary (inset) centered on the microscopes focal plane for imaging. The fluorescence microscope uses an epi-fluorescence geometry with a high-powered LED, dichroic mirror, objective, and CCD camera. (b) Example image from device during operation, showing single cells and large cell aggregates or clumps from *E. coli* constitutively expressing red fluorescent protein (*dTomato*). Contrast and brightness have been increased to show out-of-focus as well as in-focus objects. (c) Segmented image showing regions determined to be in-focus cells (blue) and clumps (red) by our custom image segmentation software (see Section 2.4).).

over periods of weeks. The total volume of the tubing between the culture vessel and the capillary is small (∼0.5 mL) to minimize the population held outside the vial and facilitate rapid sampling of cells from the culture.

Image acquisition occurs after a short pulse from the peristaltic pump passes a fresh sample through the capillary. When fluid flow slows (approximately 20 seconds) we acquire 5 images in one second with an exposure time of 25-150 ms depending on the experiment. The images are segmented in real-time by custom software (Fig. 2.1(b),(c)). To segment the images, a difference of Gaussians filter (http://scikit-image.org/) detects bright objects, followed by local thresholding in a small region around each object and a region growing technique modified from Lindebergs blob detection algorithm [67]. The segmentation routines cannot distinguish between in-focus and out-of-focus objects, so segmented objects are further classified using a support vector machine (SVM) trained on a manually-classified set of in-focus and out-of-focus cells. Separately, objects much too large to be individual cells including filamentous cells and large cell aggregates are detected by global moments-preserving thresholding [68] on the entire image (https://github.com/fiji/Auto_Threshold). Finally, low-quality images are rejected automatically by thresholding on statistical properties of the spatial distributions of objects in the imaging volume (see Section 2.4.4).

## 2.3 Custom hardware

### 2.3.1 Machined parts, system mounting, and measurement electronics

Custom machined parts (eMachineShop) designed to fit our culture vials were used to mount our systems to optical tables (Fig. 2.2), with additional parts machined separately for mounting various other pieces of equipment to the systems. For temperature measurement, we used EI1034 Temperature Probes with signal amplification from LJTick-InAmps (LabJack). Thermometers were independently calibrated using a high-accuracy digital thermometer. For optical density measurements, we used absorption geometry with TSAL6100 infrared (IR) emitters and BPV10NF IR photodiodes (Digi-Key) epoxied into nylon screws and mounted in our machine parts. Full details of machined parts are available in Appendix A, and complete electronics

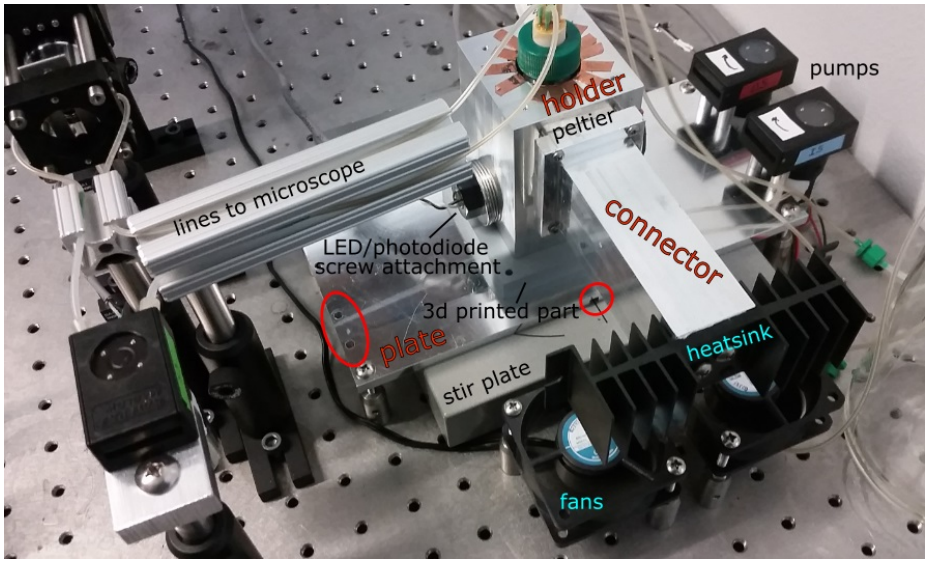


Figure 2.2: Continuous-culture device setup. Primary structural elements are holder (Fig. A.1), connector (Fig. A.2), and plate (Fig. A.3), with modifications to plate highlighted. A peltier heat pump, heatsink, fans, and temperature probe (opposite, not shown) provide temperature control, and IR LED/photodiode screw attachments in the sides provide an OD measurement via transmission through culture. Cimarec i Mono inductive stir plate provides constant stirring and Watson Marlow 400F/A peristaltic pumps control liquid flow through the system. Lines supported by T-slotted aluminum extrusions (Fig. A.4(d)) draw bacterial culture into path of microscope (Fig. 2.4). 3D printed part produced by Illinois MakerLab added to systems later, to house a white LED for growth of photosynthetic organisms.

box schematics are available in Appendix B.

### 2.3.2 Continuous-culture device control

Interfacing between a computer and control electronics was accomplished using a LabJack U3-LV DAQ device (LabJack) mounted along with related electronics systems in a custom electronics box (Fig. 2.3). All systems except the camera were controlled by custom Python software using LabJackPython. Control of pumps and LEDs was accomplished through a low-cost 8-channel relay module (Kootek). Heating and cooling for thermal control of the culture was accomplished by driving a 12711-5L31-03CQ thermoelectric heating cooling element (Custom Thermoelectric) with a power supply and a VNH2SP30 motor driver (Pololu). Camera control was managed by directly interfacing with the camera using the FlyCapture software development kit (SDK, Point Grey).

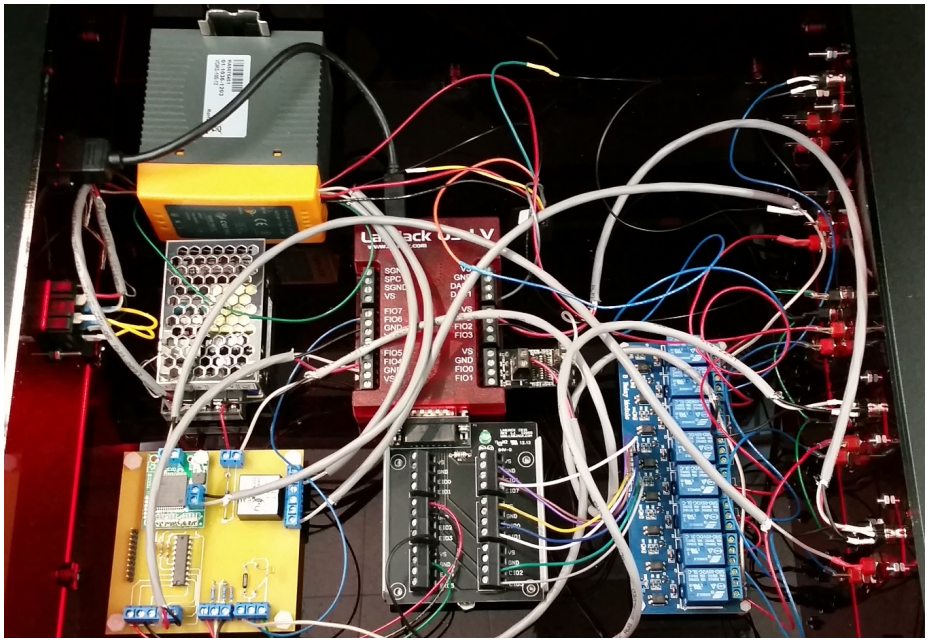

Figure 2.3: Electronics box for continuous-culture devices, with power supplies, relay modules, custom circuit board and LabJack DAQ devices.

### 2.3.3 Liquid handling and stirring

Our continuous-culture device design is similar to that of Toprak *et al.* [50], and we used 40 mL CG-4902-08 glass vials (ChemGlass) to house the 20 mL culture. All liquid connections to the cultures (inflow, outflow, microscope imaging lines) used combinations of 1 mm ID platinum-cured silicone tubing (VWR), 1.6 mm OD PEEK tubing (Fisher Scientific), and plastic connectors and luer fittings (Nordson Medical). Tubes were mounted into the culture vials using a custom 3D-printed autoclavable nylon 'cap' (Stratasys). We use 400F/A single-channel peristaltic pumps (Watson-Marlow) with relay modules to control liquid flow, with custom 'tube elements' to fit the pumps: 1.02 mm ID silicone tube elements for liquid inflow, 1.42 mm ID silicone tube elements for outflow, and 0.76 mm ID silicone tube elements for the microscope imaging line. Full details for the design and construction of caps and tube elements is available in Appendix C. At an acquisition frequency of once per minute the 0.5 mL microscope line is completely replenished at least every 10 minutes, a timescale short compared to the dilution rate of the continuous-culture device. For stirring, we used motor-free inductive Cimarec i Mono Direct stir plates (Fisher Scientific) calibrated using a custom Hall probe. All cultures were stirred at 800 rpm.

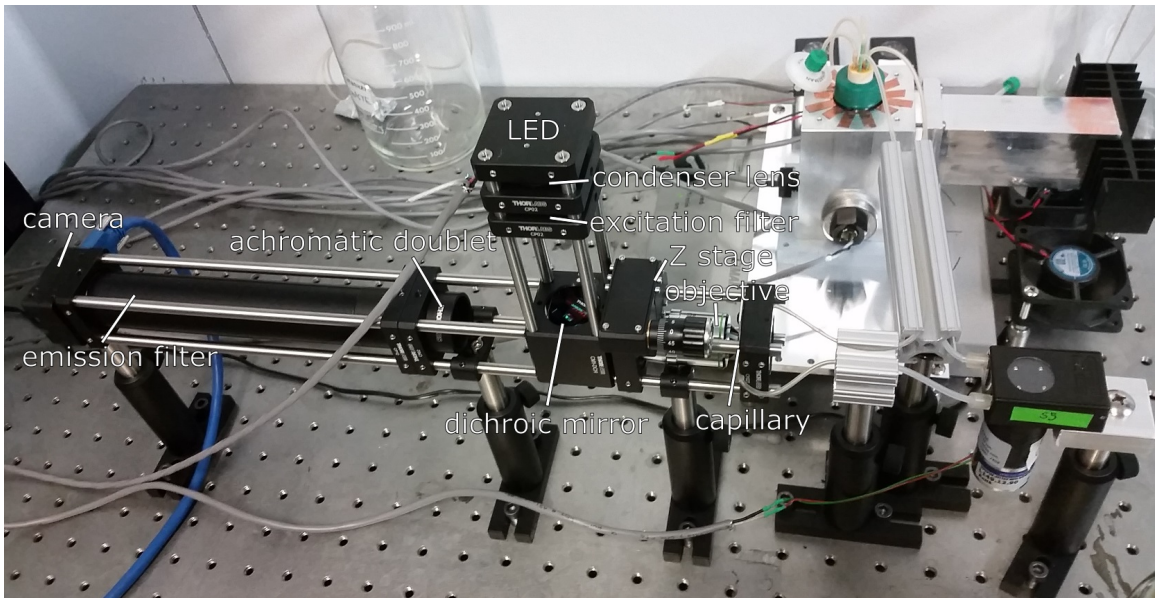


Figure 2.4: Single-color epifluorescence microscope design. Glass capillary containing imaging volume is attached to a capillary insert (Fig. D.1(e)) mounted on a machined capillary block (Fig. A.4(a)) at the end of the microscope. High-power Thorlabs M565D2 lime LED is mounted to LED mount shown in Fig. A.4(b).

### 2.3.4 Microscope design

Six identical custom single-color epi-fluorescence microscopes (Fig. 2.4) were constructed using Thorlabs optomechanics, lenses and stages in a 30 mmcage system mounted to an optical table, with an MA845 20x, 0.65 NA objective (Meiji Techno) mounted in an SM1Z linear stage (Thorlabs) for focusing. The field of view was approximately 240 µm×160 µm. Excitation illumination was provided by a high-power lime M565D2 LED (Thorlabs) controlled by a relay module and filtered using 49004 *dTomato*-appropriate filter-dichroic sets (Chroma). Illumination from the LED was collimated using a 0.79 NA ACL25416U-A aspheric condenser lens, and images were produced from the infinity corrected objective using an AC254-200-A-ML achromatic doublet (Thorlabs). Images were captured by mono-color CM3-U3-13S2M-CS CCD cameras (Point Grey/FLIR) controlled over USB 3.0.

### 2.3.5 Microscope imaging line vibration damping

Imaging problems caused by rapid micron-scale liquid oscillations in the microscope imaging line were solved by allowing the lines to sit slightly stretched along aluminum

T-slotted extrusion frames (visible in Figs. 2.2, 2.4) mounted to the optical table using special fasteners (McMaster-Carr) and optical posts.

### 2.3.6 Microscope imaging volume: capillary design

All capillaries used were borosilicate rectangular 5015 VitroTubes (inner cross-section: 0.05×1.00 mm, VitroCom). Capillaries were shortened with a diamond scribe and affixed to a black-anodized machined aluminum plate using OD2002 medical epoxy (Epoxy Technology) cured in an oven at 150 °C. Additional OD2002 epoxy was used to secure the capillary ends to the inside of standard silicone tubing and cured at the same temperature, followed by using a layer of 730 medical epoxy (Epoxy Technology) cured at 121 °C to ensure the tube-capillary-plate joint remained rigid to prevent the capillary from snapping. Capillaries were robust to repeated autoclaving. The aluminum plate was affixed to the microscope by mounting on a machined Thorlabs part of the correct dimensions to fit the microscope's 30 mm cage system. A complete protocol for capillary insert production is available in Appendix D.

## 2.4 Custom software

We developed substantial custom software for controlling the continuous-culture devices and analyzing their output, a diagram of which is presented in Fig. 2.5. The vast majority of this software runs under Python 2.7, with control over the continuous-culture devices themselves entirely controlled by calls to the LabJack DAQ device through LabJackPython. Control over the microscope cameras was handled through launching small C applications with device access through the FLIR/Point Grey FlyCapture SDK, and spline fitting (discussed in Chapter 3) was carried out using the R splines package via method calls from the rpy2 Python interface.

### 2.4.1 Experimental control and data acquisition software

The primary continuous-culture control software relies on the LabJackPython software for hardware control and a Python port of the Arduino PID Library developed by Brett Beauregard for temperature control. The program allows the user to define

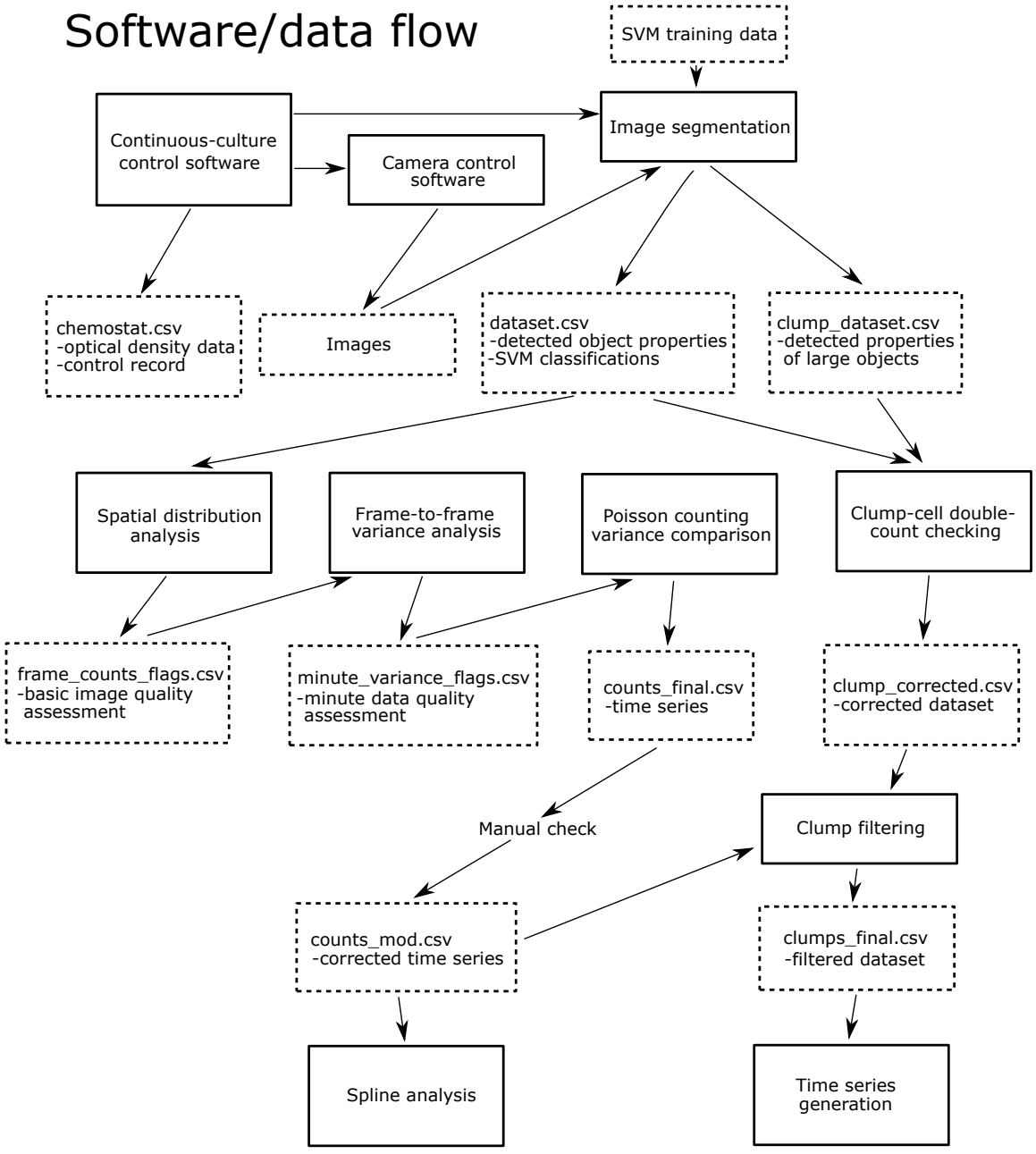


Figure 2.5: Flow of software (solid lines) and input/output data (dashed lines).

simple looping control patterns for pump control (dilution rate) as well as temperature, although our experiments ran at a constant 30 °C. The program requires basic system-level calibration information for temperature control - specifically, PID constants, the temperature probe voltage corresponding to 30 °C, and the local voltage/temperature slope near 30 °C - and outputs a record of this information and all user-defined control settings. Furthermore, once a minute the program updates a CSV file with information about the system, such as optical density and temperature readings, and about the control signals being sent to the hardware, such as the PWM output setting the heat pump duty cycle and the location in the pump and temperature control cycles. Regardless of user settings, the pumps controlling liquid inflow and outflow have assigned maximum duty cycles (87 % for the input pump, 97 % for the output pump) to ensure the output pump always runs longer than the input pump, and to ensure the optical density measurement each minute occurs when no liquid is being added to or removed from the system.

The continuous-culture control software automatically launches several additional processes. At the beginning of each experiment, a C program is launched performing a soft reset of the camera and passing it user-defined initialization settings. Once a minute, when the microscope LEDs are turned on, a separate C program is launched which triggers the rapid acquisition of the 5 images (or 'frames') which will constitute that minute's microscope data. Finally, several minutes after the start of the experiment, a separate image segmentation process is launched and automatically begins analyzing the recorded images to generate preliminary datasets. The image segmentation code uses an SVM relying on a hand-labeled training set of previously-detected objects, and is run simultaneously with the experiment because the data analysis takes time comparable to the data acquisition rate. The image segmentation code includes its own built-in timer to prevent it from running ahead of the camera output. A version of the image segmentation code without this built-in delay, as well as the associated image quality analysis programs, is available online at https://github.com/JMerrittSci/ChemostatImageProcessing/.

### 2.4.2 Feature detection and cell segmentation preparation

Using the scikit-image and NumPy packages, all images from the microscope are passed through a nearest-neighbor median filter to remove hot pixels, followed by a bilateral mean filter to smooth the image while preserving sharp boundaries between regions of different brightness. Images are then passed through a difference of Gaussians filter to detect the locations of bright, cell-sized objects. Local subimages of the image are isolated around each detected object. The bottom third of the intensity range of each subimage is discarded as noise, and the remainder of the intensity range is divided into 14 equal-width intensity bins (Fig. 2.6). 14 binary masks are constructed, corresponding to pixels with intensity values that fall within each bin. These masks are subjected to a binary erosion to remove isolated pixels, followed by a binary dilation to smooth edges. Next, all the masks for a subimage are layered, with higher-intensity masks on top, to generate a new 15-color subimage representing a simplified, smoothed approximation of the subregion's object. Finally, the subimage is divided into regions of connected equal-intensity pixels, and each region is assigned a list of all neighboring regions.

### 2.4.3 Subimage analysis and cell identification

The 15-color subimage analysis follows a modified form of Lindeberg's algorithm [67]. Regions from each subimage which are local maxima, defined as being adjacent to no regions of greater brightness, are designated as blob 'seeds.' Any seeds located on the border of the subregion are viewed as representing objects other than those detected by the difference of Gaussians filter, and are treated the same as other seeds for the remainder of the subimage analysis but ultimately discarded. Seeds form blobs by flooding outwards, absorbing neighboring, lower-intensity regions, starting with the brightest regions in the image and ending with those 1 intensity value above background. Regions which would be absorbed by two separate blobs are assigned competitively to whichever initial blob seed is closer to the region's centroid. After this process finishes, masks are made of each blob other than those with seeds on the image border, and applied against the original image.

A series of features for machine learning are calculated for each blob, including

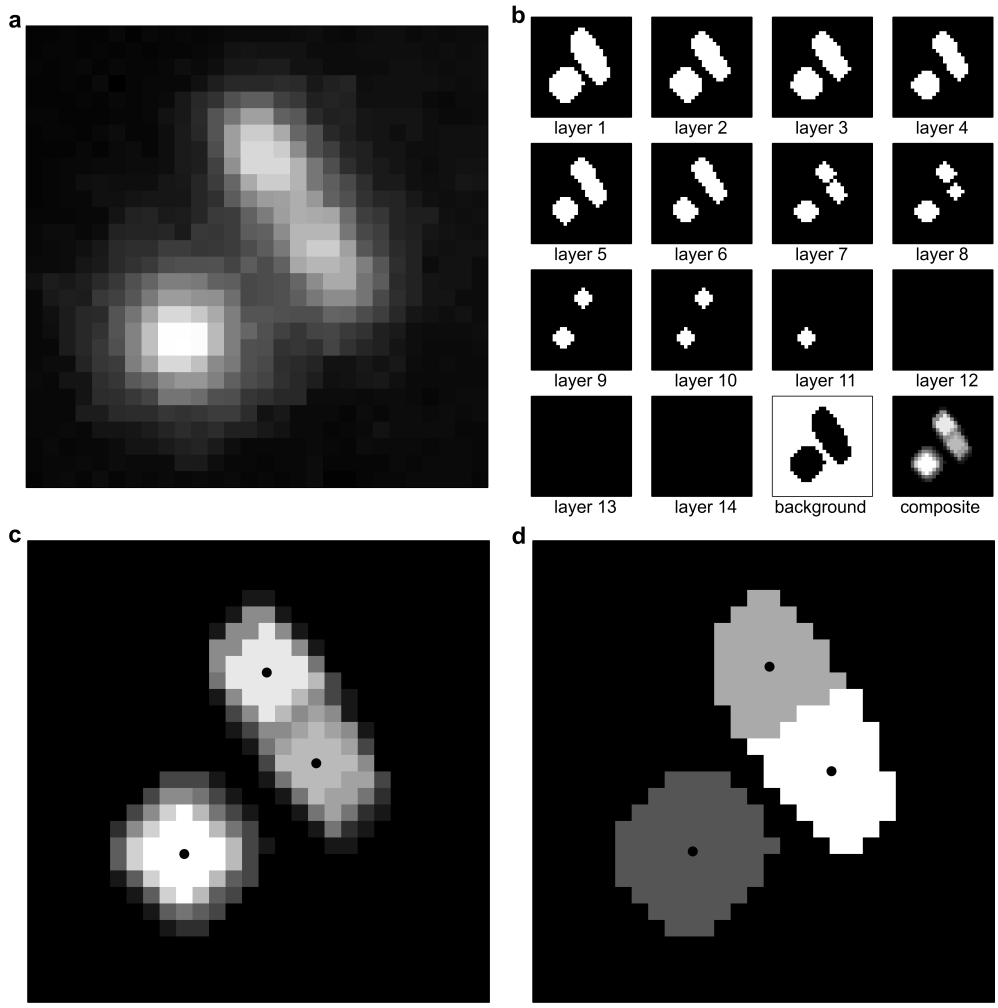


Figure 2.6: Subimage segmentation of detected features in images. (a) Real subimage data, having undergone a median filter and bilateral mean filter for smoothing. (b) Individual and composite masks representing different brightness thresholds. Each individual mask separately undergoes a binary erosion and dilation to remove small features and smooth edges. (c) Composite mask, with black dots indicating centers of blob seeds. (d) Blob seeds expanded to create blob masks (black dots indicate mask centroids).

blob size, shape, and intensity. Using scikit-learn, a support vector machine (SVM) fed with a previously-generated hand-curated training set containing thousands of detected objects reads in the blob features and assigns each blob a label as noise, a single cell, or, more rarely, two cells. 'Two cell' labels represent situations in which partly overlapping cells could not be distinguished as different objects during the subimage analysis, but can still be distinguished from single-cell objects on the basis of their combined spatial features. Our SVM uses a radial basis function (RBF) kernel with empirically-determined fitting parameters $C = 10^5$ and $\gamma = 10^{-3}$, and the training set - incorporating images from all growth stages from all replicate systems - was found by cross-validation to have at minimum 90 % accuracy in label assignment at all growth stages except from the first day of each experiment, when cells are too dim to detect reliably. Because the first washout event in each experiment starts at the beginning of the third day, the reduced SVM accuracy during the first day does not affect our results.

### 2.4.4 Image quality control: cell spatial distribution analysis

To evaluate the quality of individual images, we calculate the center of mass $(\mu_x, \mu_y)$ of all the cells in-frame and assume cell locations are uncorrelated and uniformly distributed along both the x and y axes. For a uniform distribution of N cells along the x dimension in an image of width $W$ the expected standard error of the mean is $\sigma_{x,theory}(N) \equiv \sqrt{\frac{W^2}{12N}}$. If we assume the center of the image to be the origin and use the Q-function to approximate the odds of having the mean be located at least a distance $|\Delta\mu_x|$ from the center (in either direction) along the x-axis we calculate an approximate probability $P_x(\mu_x, N) = 1 - erf[\frac{|\Delta\mu_x|}{\sigma_{x,theory}(N)*\sqrt{2}}]$. Calculating the probability along the y-axis the same way, the total probability of getting an image with the center of mass of the cells as far from the center of the image as we actually get is approximated by $P = P_x P_y$. Under this approximation, we discard images with a result extreme enough to have a probability below 0.0001 %. This is a lenient threshold; only 1 in 1 million images would be expected to yield a result this extreme based on chance alone. Therefore, images rejected under this threshold alone are nearly always faulty in some way, most often due to containing large bubbles that significantly skew the distribution of cells.

### 2.4.5 Minute data quality control: frame-to-frame variance analysis

Because the spatial distribution analysis only rejects images with poor quality due to skewed distributions of cell positions, we do an additional quality control pass over each minute's worth of data to check internal consistency. All frames taken within the same minute should be of a slow-moving sample and acquired over the span of approximately one second; as a result, we expect to detect similar numbers of cells in each image.

We denote the number of cells detected in image $j$ of the $i^{th}$ minute of the experiment as $N_i^j$, where $j \in \{0 \dots 4\}$. We discard all $N_i^j$ if more than two images in the image set from minute $i-1$ were discarded or if $\sigma_j^2(N_i^j) > a\langle N_i \rangle_j$ where $\sigma_j^2$ denotes the variance in $N_i^j$ for all $j$ for a given minute $i$, and $\langle N_i \rangle_j$ denotes the average across $j$. The factor $a$ was determined empirically and was set to 3.2. Although $\sigma_j^2(N_i^j)$ should not be Poisson-distributed due to temporal correlation, acceptable variances due to counting noise still depend on $\langle N_i \rangle_j$, and were determined empirically by plotting $\sigma_j^2(N_i^j)$ against $\langle N_i \rangle_j$ for all $i$ as shown in Fig. 2.7. The large-variance images removed by this step tend to have suffered image segmentation failure, often due to fast-moving, poorly-imaged samples in the microscope.

### 2.4.6 Abundance time variation quality control: Poisson variance comparison

Because the image and minute data quality control steps listed above are conservative, we additionally check the quality of an individual minute's data by comparing it to data from previous images, under the assumption that the actual density of a bacterial culture cannot change quickly on the timescale of minutes. This processing step removes time points that were not excluded in previous processing steps but where imaging failed. As above, $\langle N_i \rangle_j$ denotes the average cell counts of all frames $j$ taken during a minute $i$. Starting with the first five minutes, we keep a rolling set $S_i$ of five average counts from five earlier minutes which passed the criteria specified below, defined as $S_i = \{\langle N_{k_1} \rangle_j, \langle N_{k_2} \rangle_j, \langle N_{k_3} \rangle_j, \langle N_{k_4} \rangle_j, \langle N_{k_5} \rangle_j\}$ for minutes indexed by $k_1, k_2, k_3, k_4, k_5 < i$.

Each minute's average counts $\langle N_i \rangle_j$ are compared against $S_i$ as described below

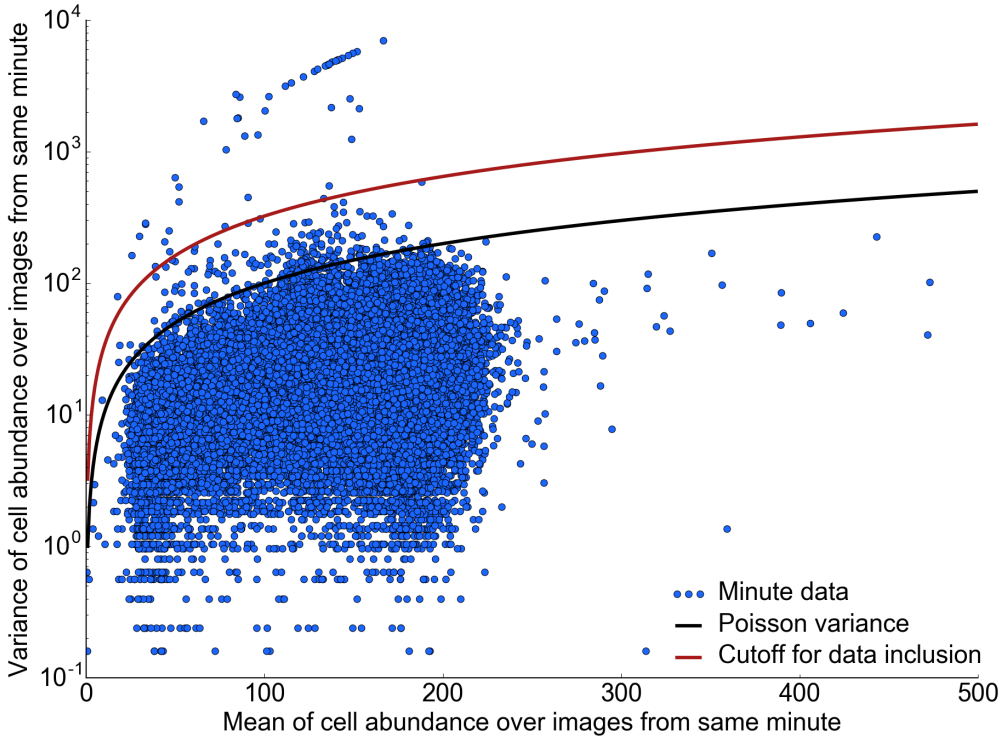


Figure 2.7: Distribution of cell count variances in individual minutes. As frames within minutes are correlated, variance is generally lower than Poisson counting variance (black line). Minutes with variances higher than the red line are rejected as low quality data, with threshold chosen conservatively to include points near the primary cloud of data.

and combined with the elements of $S_i$ (removing the earliest element of $S_i$ in the process) to create the new set $S_{i+1}$. If a minute's data fails to pass the criteria stipulated below it is discarded. To prevent rejecting data for long stretches of time, a minute's average abundance $\langle N_i \rangle_j$ is allowed into $S_{i+1}$ regardless of whether it passes the criteria defined below if the oldest element of $S_i$ is from at least ten minutes earlier (e.g. $\langle N_{i-10} \rangle_j$).

$\langle N_i \rangle_j$ is compared to mean of the elements of $S_i$ and the theoretical Poisson standard deviation expected from that mean, $\sigma_i = \sqrt{mean(S_i)}$. $\langle N_i \rangle_j$ is retained if $|\langle N_i \rangle_j - mean(Si)| < 3\sigma_i$ or, if previous image quality control steps determined the minute's data met the slightly stricter threshold of $\sigma_j^2(N_i^j) < 2.9\langle N_i \rangle_j$, the slightly more lenient condition $|\langle N_i \rangle_j - mean(Si)| < 4\sigma_i$. In a typical experiment, <5 % of the minutes in an experiment are discarded during this step, as shown in Fig. 2.8.

Note that because this algorithm still allows some poor quality data through, particularly when many recent minutes' worth of data had already been discarded, the final data sets are checked by hand. Rapid and apparently impossible density fluctuations (such as a very high cell density dropping to zero in two minutes) are checked by direct comparison to images from the original experiment, and minutes containing images with clear problems such as large but undetected bubbles are discarded to create the final time series. In a typical experiment, fewer than ten such questionable fluctuations need to be checked by hand. A description of this manual time series cleanup, as well as a description of the imaging problems demanding it, is available in Appendix E.

### 2.4.7 Cell aggregate image segmentation

Because cell aggregates are large and bright enough to be dominant features of the images in which they appear, image segmentation for aggregates is significantly faster and simpler than segmentation and quality checking for cells. Using a free implementation of Tsai's statistical moment-preserving threshold [68], a binary mask of the entire image is constructed preserving statistically important objects, including aggregates wherever they appear. Disconnected regions of this mask are collected as possible cell aggregates or 'clumps,' and small objects which should be detected as cells are immediately discarded by a size threshold. Next, suspected aggregates are

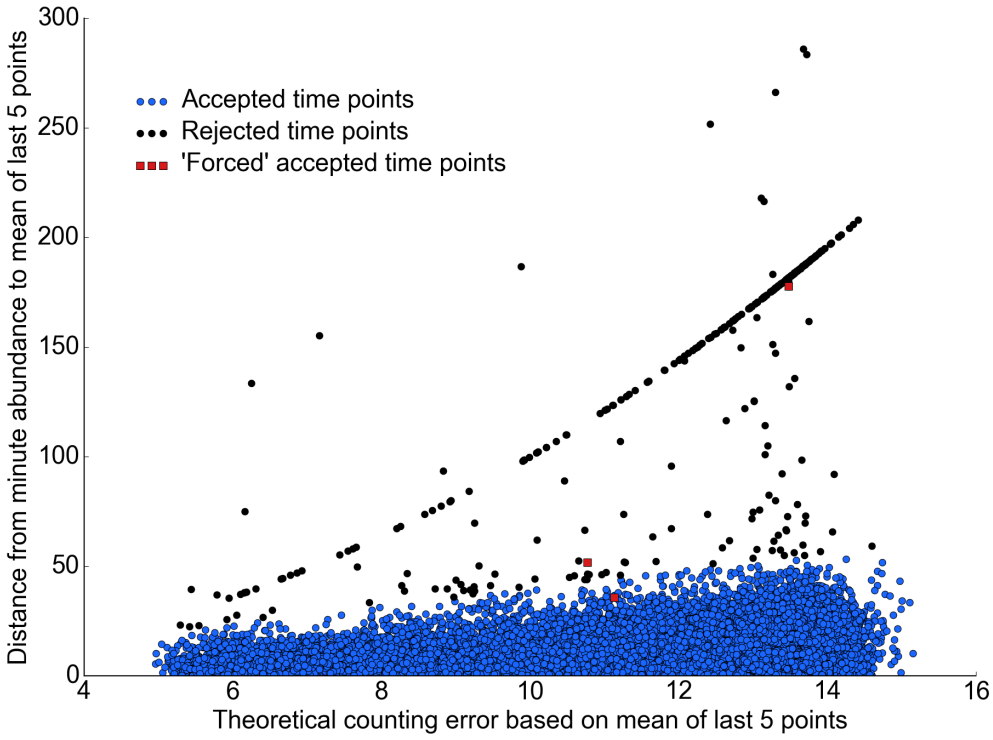


Figure 2.8: Counting error minute-level quality assessment. All points represent a minute of data from a full dataset, with the y-axis showing the actual distance of that minute's detected number of cells from the mean of the last 5 known 'good' points. Blue points correspond to minutes accepted having a deviation from the mean low enough to realistically follow previous time points. Black points correspond to rejected minutes, with the apparent 'curve' of black points representing minutes where counts suddenly dropped to zero after the sudden appearance of a bubble in the imaging volume. Red squares correspond to points which have deviations from the mean high enough to be rejected, but are provisionally included in the time series due to no other points recently being accepted into the time series.

checked against locations and properties of detected cells, and aggregates which substantially overlap with cells are discarded as being locally-dense collections of cells. Because the vast majority of aggregates are large, dense objects, very few aggregates are discarded during this step. Finally, intensity information corresponding to remaining clump candidates is collected and any objects meeting set intensity thresholds are initially counted as aggregates, which has the effect of discarding unusually bright single cells which appeared large due to being out of focus. During the last step, aggregates from minutes of data which were already discarded in the cell segmentation quality checking steps as low quality are also ignored. Finally, remaining aggregates can be used to generate statistical information, such as distributions of clump sizes, as well as time series of clump abundances.

# Chapter 3

# Preliminary experiments

This chapter contains material from published work by Jason Merritt and Seppe Kuehn[1], used with permission of the authors.

This work was partially supported by the Center for the Physics of Living Cells, the National Science Foundation Physics Frontier Center (PHY 0822613 and PHY 1430124), the Carl R. Woese Institute for Genomic Biology, and the Department of Physics at the University of Illinois at Urbana-Champaign. The dissertation author was the primary experimental investigator of this work.

Contributions: Seppe Kuehn and Jason Merritt contributed to the conception and design of the experiment, the design of the apparatus, the analysis and interpretation of the experimental results, and the creation and review of the manuscript. Jason Merritt constructed the apparatus, carried out the experiments, and wrote the custom software used in the experiment.

Acknowledgements: Bacterial strain under study was created by Doeke Hekstra at Rockefeller University. Morbidostat design from Erdal Toprak's lab [60] provided inspiration for continuous-culture device design. Preliminary work relied on generous use of space and equipment by Thomas Kuhlman's lab.

## 3.1 Introduction

In this chapter we present results from preliminary experiments designed to test the capabilities of the custom continuous-culture devices described in detail in Chapter 2, as well as laying the groundwork for the frequency- and amplitude-varying experiments discussed in Chapter 4. The experiments confirm the long-term stability of our systems and demonstrate a relationship between slow, but non-zero, growth and

[1] Merritt, J and Kuehn, S. Quantitative high-throughput population dynamics in continuous-culture by automated microscopy. *Scientific Reports* **6**, 33173 (2016).

the appearance of free-floating cell aggregates in *E. coli*. A set of control experiments confirm that our results are independent of the presence of the antibiotic used and the exact mutations in our constructed fluorescent strains, and confirm the reliability of our planktonic cell counts with independent measurements of cell density from plating. Finally, we present an overview of the spline-based algorithms used to analyze the recovery of planktonic abundances following the population reduction accompanying our basic applied perturbation, the washout event.

The washout events in our systems, discussed in more detail below, result in most of the bacterial culture being replaced with fresh media, causing both a significant drop in bacterial population size and a rapid upshift in glucose concentration. Variable nutrient levels are believed to impact community function [9], and cyclic nutrient upshifts and downshifts are present in a variety of contexts, such as concentrations of dissolved organic carbon shifting in relation to water level in intertidal zones [3], and concentrations of glucose and other sugars in the mammalian gut varying over the course of the day in response to host feeding [69, 70] and release of stomach content into the intestine [69]. The washout events in our experiments also specifically mimic flushing, a process where water flows in nature rapidly flush accumulated dissolved organic carbon in soil into bodies of water [71]. We show the cyclic application of washout events in our systems results in a history-dependent population response, where planktonic cell abundance recovers more rapidly from washout over successive washout events.

## 3.2 Chemostat stability experiment

We first tested the long-term stability of our continuous-culture system and imaging apparatus by running three replicate systems at a constant dilution rate (chemostat operation, $D = 0.08\,\mathrm{h}^{-1}$) for 550 hours. We performed these experiment in M63 minimal media with low glucose concentrations (0.04 % w/v, 2.2 mM) and chloramphenicol at $12.5\,\mu\mathrm{g\,mL}^{-1}$, using a strain of *E. coli* expressing red fluorescent protein (*dTomato*) constitutively from the chromosome. These and other experiments were carried out with temperature control at 30 °C in a room also environmentally controlled at 30 °C (Darwin Chambers). Full experimental protocols for chemicals used

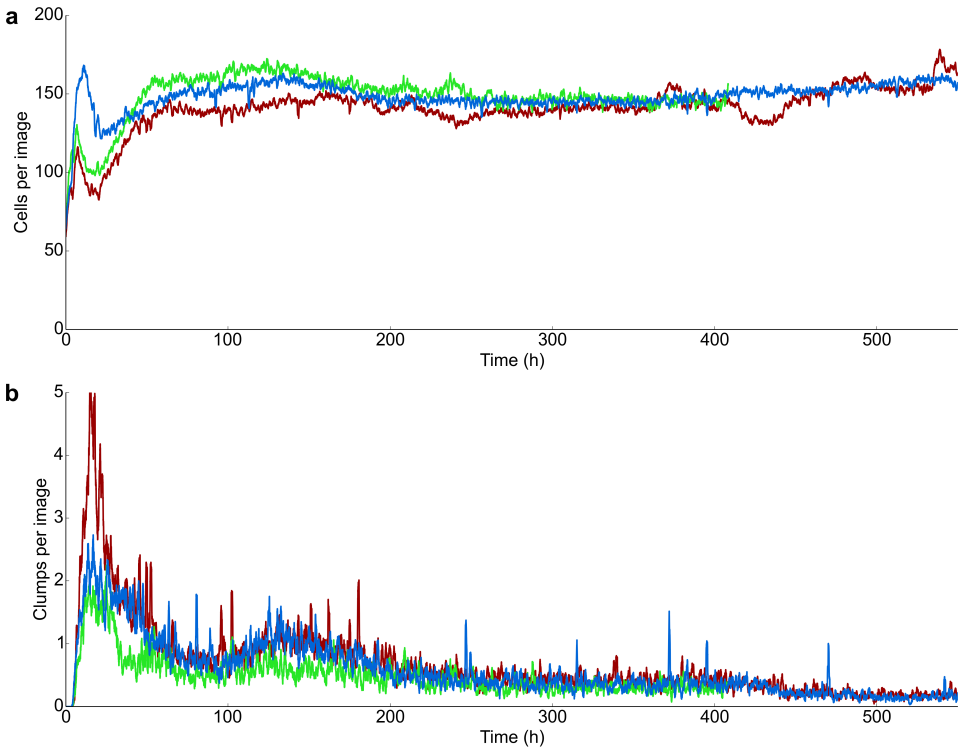


Figure 3.1: Long-term steady-state chemostat experiment. (a) Single-cell abundances, not including aggregates, from image segmentation in three replicate steady-state chemostat ($D = 0.08\,\mathrm{h}^{-1}$) over a 23-day experiment. Data shown is smoothed by a rolling average with a one-hour window. One system was stopped after ∼16 days due to imaging problems. (b) Clump (cell aggregate) abundances for three replicate systems during the same experiment shown in (a). Data shown is smoothed by a rolling average with a one-hour window.

and experiment setup are available in Appendix F. We found the abundance dynamics across replicates to be reproducible (Fig. 3.1), demonstrating the long-term stability of our continuous-culture devices and microscopy.

## 3.3 "Washout event" perturbation

We next moved to use these systems to study long-term abundance dynamics in communities of *E. coli* in fluctuating nutrient conditions, where the population alternates between periods of chemostat operation at the basal dilution rate (famine conditions [11] at $D = 0.08\,\mathrm{h}^{-1}$, doubling time $t_d = 8.66\,\mathrm{h}$) and rapid "washout events" where 90-99 % of the population is replaced with fresh medium over the course of one to two hours (feast conditions). Washout events simultaneously reduce the population by a factor of 10 to 100, depending on the amplitude, and increase the substrate (glucose) concentration from a few micromolar [72] to approximately 2 mM, resulting in periods of rapid growth as the population recovers to its steady state abundance (Fig. 3.2(a)). Immediately after the washout event the dilution rate of the continuous-culture device returns to $0.08\,\mathrm{h}^{-1}$.

Throughout the cycles of feast and famine we performed automated imaging once per minute on samples drawn from the growing bacterial population. During periods of famine we observed both planktonic (single-cell) populations and aggregated cells (Fig. 2.1(b)). From the size of the aggregates (discussed in more detail in Chapter 4; see Fig. 4.14) we estimate that, at steady state, the numbers of planktonic and aggregated cells are of the same order ($1 \times 10^8$ $\mathrm{mL}^{-1}$). During washout events the planktonic population declines by 10- to 100-fold and the number of aggregates falls to nearly undetectable levels. Subsequently, with the continuous-culture device operating at the basal dilution rate, the planktonic population rapidly returns to its steady state value. The population of aggregates remains low (<0.1 per image) until the planktonic population growth rate declines below $0.2\,\mathrm{h}^{-1}$ and then begins to recover (Fig. 3.2(d)).

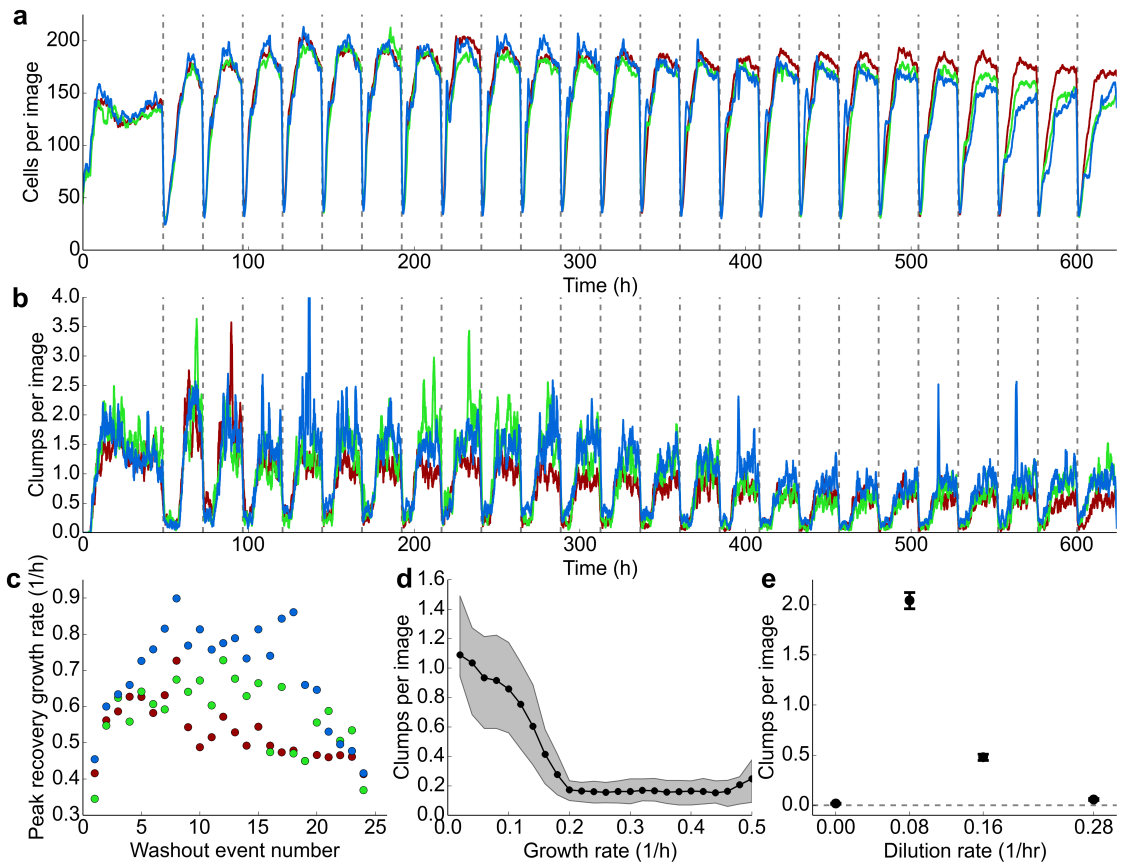


Figure 3.2: Long-term 24 h-period experiment with 1 h washout events. (a) Single-cell abundances, not including aggregates, from image segmentation in three replicate continuous-culture devices over a 26-day experiment. Data shown is smoothed by a rolling average with a one-hour window. Each dashed vertical line represents a washout event where ∼90 % of the culture is pumped out and replaced with fresh media. (b) Cell aggregate or 'clump' abundances for three replicate systems during the same experiment shown in (a). Data shown is smoothed by a one-hour rolling average. (c) Peak population recovery rates (Fig. 3.7) increase quickly after the first washout event, but eventually decline. Peak growth rates are calculated during single-cell population recovery (see Section 3.7) following the washout events shown in (a). Error bars from fit are smaller than markers. (d) Following a washout event, aggregate abundances remain low until the specific growth rate of the single-cell population slows to approximately $0.2\,\mathrm{h}^{-1}$. Graph shows data from recovery after all washout events in one system, before the next washout event begins, sorted into equal-width growth rate bins. Shaded region show central two-thirds of aggregate abundance data in each bin. (e) Separate experiments were carried out to determine aggregate abundances after a population reaches steady state at a constant dilution rate, rather than during recovery after a washout event. Data represents a time average of aggregate abundances between 40 and 48 hours after a populations introduction to constant dilution conditions, and error bars show the standard error of the mean for data in this period.

## 3.4 Feast-famine stability experiment

We formalized a basic experimental protocol for feast-famine experiments, also followed in our later experiments, where bacteria in the continuous-culture devices are initially exposed to a 48-hour acclimatization period at the basal dilution rate ($D = 0.08\,\mathrm{h}^{-1}$) before perturbation with washout events begins. In our first experiment in fluctuating conditions, we applied washout events every 24 hours for a period of 26 days in three replicate continuous-culture devices.

We observed that the resilience of the population to the perturbation, defined as the maximum rate of recovery from washout events (Fig. 3.7), depends on the history of past perturbations (Fig. 3.2(c)). In particular, the resilience of the population increases approximately 50 % over the first 34 washout events. Since the nutrient concentrations must be nearly identical after each washout event, this behavior cannot be ascribed to variable nutrient concentrations in the culture during the recovery. Further, this increasing resilience is apparent after just 16 generations (120 hours) which is very likely too fast for a mutation to fix. For example, a mutant with a selection coefficient $s = \frac{r_m - r_{WT}}{r_{WT}} = 1.4$ (where $r_m$ and $r_{WT}$ are the mutant and wild-type growth rates respectively) would reach a relative abundance of approximately 0.5 on this timescale. A selection coefficient of 1.4 is 10 to 100 times larger than typically observed for bacterial chemostats [44]. Previous studies of *E. coli* under glucose starvation conditions have shown that *rpoS* mutants can reach high abundance on the timescale of 10 generations, but such mutants do not arise in the MG1655 genetic background used here [73]. However, at long times (>200 h), genetic diversity likely becomes significant [73], and this diversity may account for the decline in resilience and increasing variation across replicate communities we observe at longer times (Fig. 3.2(c)).

Therefore, we conclude the time-dependent resilience we observe over the first 6 days of the experiment is driven by non-genetic changes in the population. Such changes may include metabolic adaptation to the fluctuating environment that is uniform across the population such as history dependent lag-phase [74]. Another possibility is the presence of a slow-growing subpopulation, such as persisters [30, 36]. If a large fraction of the population is slow-growing prior to the first washout event, and subsequently declines with repeated washout events this could account

for increasing resilience [36]. Finally, the dynamics could be driven by patterns of dispersal from aggregated populations. Discriminating between these possibilities required measurements at the single-cell level and further experiments documented and discussed in Chapter 4.

## 3.5 Growth rate dependence of aggregation

Our instrument also reveals growth rate dependent aggregation (Fig. 2.1(b)). To our knowledge the presence of aggregates in slow-growing populations of *E. coli* has not been previously reported, likely due to the difficulty in discerning their presence using standard techniques such as plating and optical density measurements. These cell aggregates or 'clumps' typically contain at least tens of cells and can make up approximately half of the biomass present in a community (see Section 4.6.1). We observe surprising aggregation dynamics over the course of a washout event (Fig. 3.2(b),(d)). Immediately after a washout event aggregates remain at low abundance as the planktonic cell abundances increase rapidly (growth rates $>0.3\,\mathrm{h}^{-1}$). When the growth rate of single cells declines to approximately $0.2\,\mathrm{h}^{-1}$, we observe a rapid rise in the presence of aggregates (Fig. 3.2(d)).

We performed additional short-term experiments to investigate the growth rate dependence of aggregation. In a chemostat the growth rate must equal the dilution rate at steady state [44]. We operated the continuous-culture devices as chemostats at different dilution rates (growth rates): $D = 0$ (batch culture), $0.08\,\mathrm{h}^{-1}$ ($t_d$ =8.6 h), $0.16\,\mathrm{h}^{-1}$ ($t_d$ = 4.3 h) and $0.28\,\mathrm{h}^{-1}$ ($t_d$ =2.5 h) without applying washout events and quantified the abundance of cell aggregates after the abundance of single cells reached steady state (40-48hours, Fig. 3.3). These measurements revealed a surprising non-monotonic dependence of aggregation on growth rate (Fig. 3.2(e)). We observe no aggregation as a batch culture enters stationary phase (zero growth), a peak in the number of aggregates at $D$ =$0.08\,\mathrm{h}^{-1}$ and a steady decline in the number of aggregates in the chemostat up to $D$ =$0.28\,\mathrm{h}^{-1}$ (for description of control experiments see Figs. 3.3, 3.4).

Cellular aggregation in the form of attached biofilms or wall growth has been widely observed in chemostats [44]. It is possible that the aggregates we observe result from

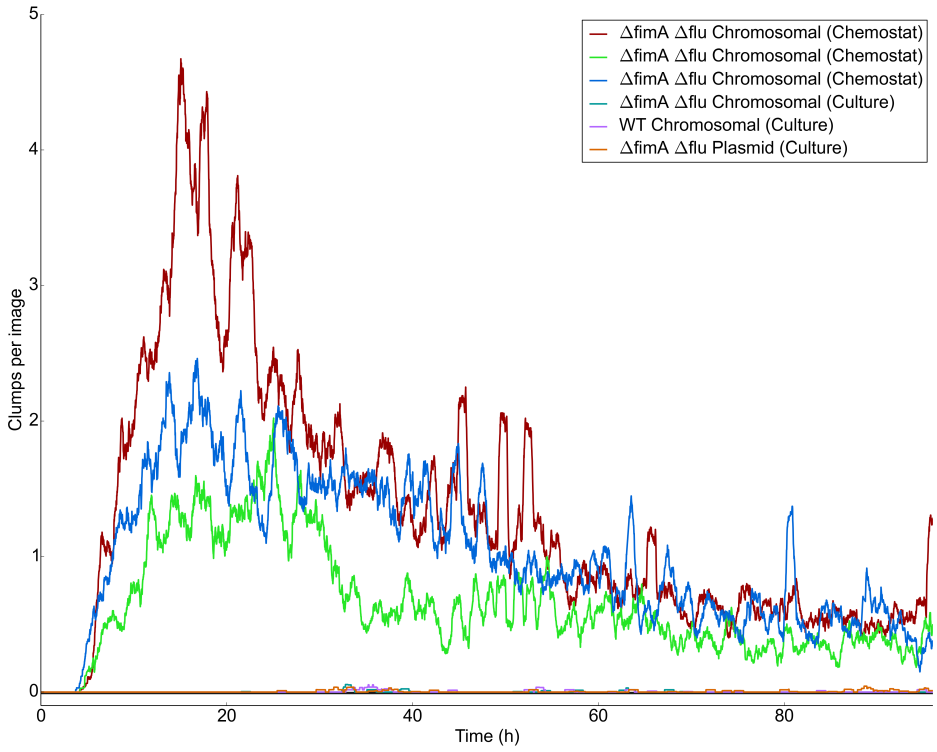


Figure 3.3: Cell aggregation in batch culture vs. chemostat conditions. Cell aggregation of *E. coli* expressing *dTomato* constitutively from the chromosome or a plasmid in batch culture and chemostat conditions ($D = 0.08\,\mathrm{h}^{-1}$, Fig. 3.1). Cell aggregates almost never form in batch culture even after four days, and most of the few aggregates detected in batch culture are likely false positives due to overlap and exceptionally bright planktonic cells.

the release of attached biofilms; however, the aggregates in our experiments manifest within the first generation, are suppressed at higher growth rates (where adhesion is more likely [44]), and decline in abundance over time, making wall growth an unlikely source. Also, for the experiment in Fig. 3.2(a) we observe minimal adherence to the vial walls, tubing and capillary after 26 days of continuous culture. We performed additional experiments to show that aggregates formed at slow growth rates with or without selective antibiotics (our *dTomato* expressing strain is chloramphenicol resistant) and mutants with reduced adhesion ($\Delta fimA$, $\Delta flu18$; see Fig. 3.4). We conclude that aggregation is triggered by the onset of very slow but non-zero growth rates (Fig. 3.2(e)).

Aggregates constitute surprising spatial structure present even in clonal populations under controlled environmental conditions. This structure has a complex, non-monotonic dependence on the growth rate of the population (Fig. 3.2(e)) and likely has important ecological implications since clusters of cells have elevated antibiotic resistance [41] and resemble stationary-phase cells [40].

## 3.6 Density calibration

To relate the number of cells per image (Fig. 3.2(a), Fig. 3.1) to the density of cells in the continuous-culture device, a culture of *E. coli* expressing *dTomato* ($Cm^R$) constitutively from the chromosome was grown to stationary phase in M63 minimal media with 0.06 % glucose and 12.5 µg mL$^{-1}$ chloramphenicol. Samples of this culture, which did not contain aggregates, were diluted to varying concentrations over an approximately 200-fold range in phosphate-buffered saline. A small portion of each sample was plated, with the remainder of the sample put in the continuous-culture device and imaged for 30 minutes. The colonies on the plates were counted 24 hours later, then again after another 24 hours to check for the presence of slow-growing cells. Finally, the number of colonies converted to cell density was plotted against the 30-minute average of the number of cells detected by image processing (Fig. 3.5) and a linear regression was performed on these data which yielded an estimate of the imaging volume: $2.96 \pm 0.03 \times 10^{-7}$mL.

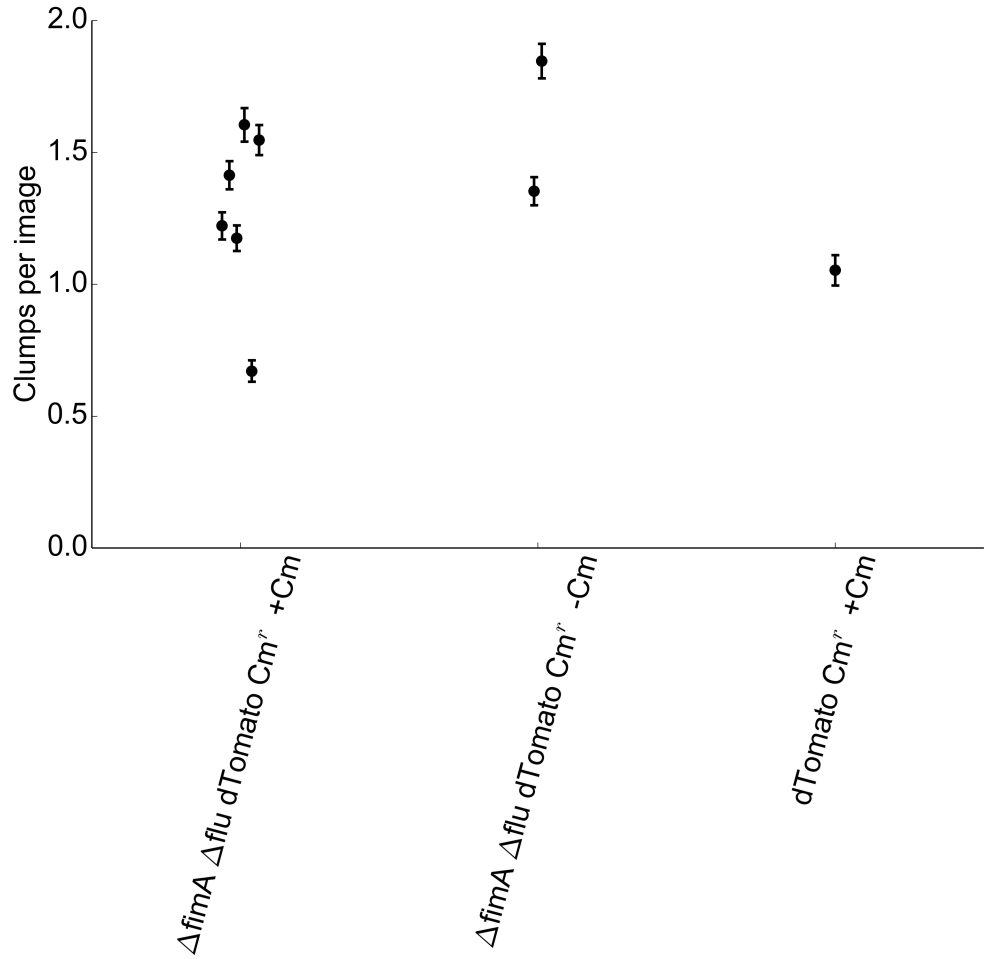


Figure 3.4: Cell aggregation dependence on antibiotic and genotype. All strains used are chloramphenicol resistant ($Cm^r$). "*dTomato* $Cm^r$" denotes MG1655, HK022 att::(*cat* $P_{\lambda R}$-*dTomato*) *hsdR*. In all repeated washout experiments the medium contained chloramphenicol to reduce the risk of contamination. Here we confirm that the presence of this antibiotic did not induce aggregation, and that the $\Delta flu$ and $\Delta fimA$ mutations did not cause aggregation. Estimates of average aggregate abundance per image determined by averaging across the last 8 hours of a 2 day period of constant dilution at $D = 0.08\,\mathrm{h}^{-1}$. We do not see a significant change in the amount of cell aggregation depending on the presence of $Cm$ (Welch's t-test, $p = 0.28$) or the $\Delta flu$ and $\Delta fimA$ mutations (probability of observing number of aggregates at least as far from the mean as in *dTomato* $Cm^r + Cm$ given the observed number of aggregates in $\Delta flu$, $\Delta fimA$ *dTomato* $Cm^r + Cm$ is 0.48, two-tailed test). The plasmid strain (MG1655 $\Delta fimA$, $\Delta flu$ *PZS*3R dTomato*) produces a similar number of aggregates in the same conditions (Fig. 3.2(e)), but is not shown here because the increased brightness of the strain artifically raises the number of detected aggregates if the same thresholds are used. The outlier in the $\Delta fimA$ $\Delta flu + Cm$ condition was caused by a sudden drop in the number of detected aggregates in one system after ∼30 hours (shown in Fig. 3.3).

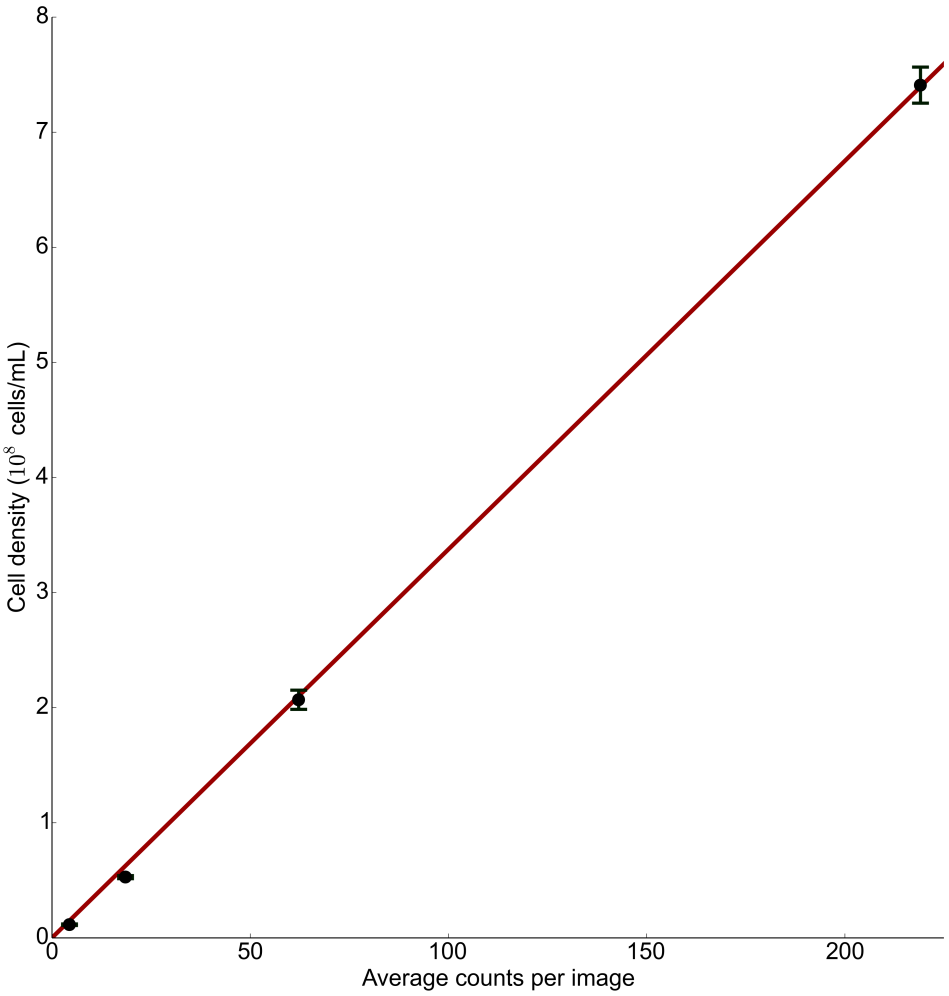


Figure 3.5: Density measurement calibration. Calibration curve to convert cells/image to actual culture density. Counts per image for samples taken from cultures with densities determined by plating. By linear regression we calculate a conversion factor of $3.375 \pm 0.027$ x $10^6$ (cells/mL)/(counts/image).

## 3.7 Growth rate spline analysis

To recover the growth rate data reported above, we defined $n(t_i) = \langle N_i \rangle_j$, the average over all images $j$ taken during minute $i$. Growth rates are determined by fitting $log(n(t))$ using smoothing cubic spline functions from the splines package of R, accessed from Python via rpy2. To obtain accurate instantaneous growth rate estimates, the dilution rate $D(t)$ must be added back in; however, because $D(t)$ changes instantaneously in our experiments at the start and end of washout events, the derivative of $n(t)$ does not exist at those points, making smoothing splines a poor choice for directly fitting the data. Instead, to get a smooth curve for spline fitting, we subtract the effect of dilution out of our data by instead fitting to $log(n(t)) + \int_0^t D(t)dt$ (Fig. 3.6(a)), which is equivalent to modeling our population as growing to arbitrarily high density, rather than continuously being diluted out of the system. However, naively changing $D(t)$ when the dilution rate changed in the experiment was also found to introduce significant artifacts into our fits (Fig. 3.6, left column) resulting from a delay between the dilution rate changing in the experiment and the change in dilution rate being detectable in the microscope due to the minutes-long delay between cells being sampled from the system and reaching the microscope imaging volume. Accounting for this delay resulted in the removal of these artifacts (Fig. 3.6, right column).

To determine appropriate fits, for each washout event, the counts data was split into 10 cross-validation sets, with the fits using *spar* (R smoothing parameter) values ranging from 0.5 to 1.0 performed on training sets composed of 90 % of the total data and tested against the remaining 10 %. If the spline fit is defined by $s(t)$, the quality of each fit was determined using the cost function $C(spar) = \sum(n(t) - s(t))^2 + 0.04\sum(s''(t))^2$, and the *spar* value resulting in the mean lowest value of $C$ over each of the cross-validation sets was recorded. This entire process was repeated a total of 10 times, with the final value of *spar* saved for the washout event being the average optimum value over all 10 runs.

Finally, bagging (bootstrap aggregation) using the value of *spar* found above was used to generate the final spline fits. Specifically, 100 random bootstrap training sets were constructed from the washout event's data, and the final bagged fit value was taken to be the average predicted value at each time point over all bootstrap fits.

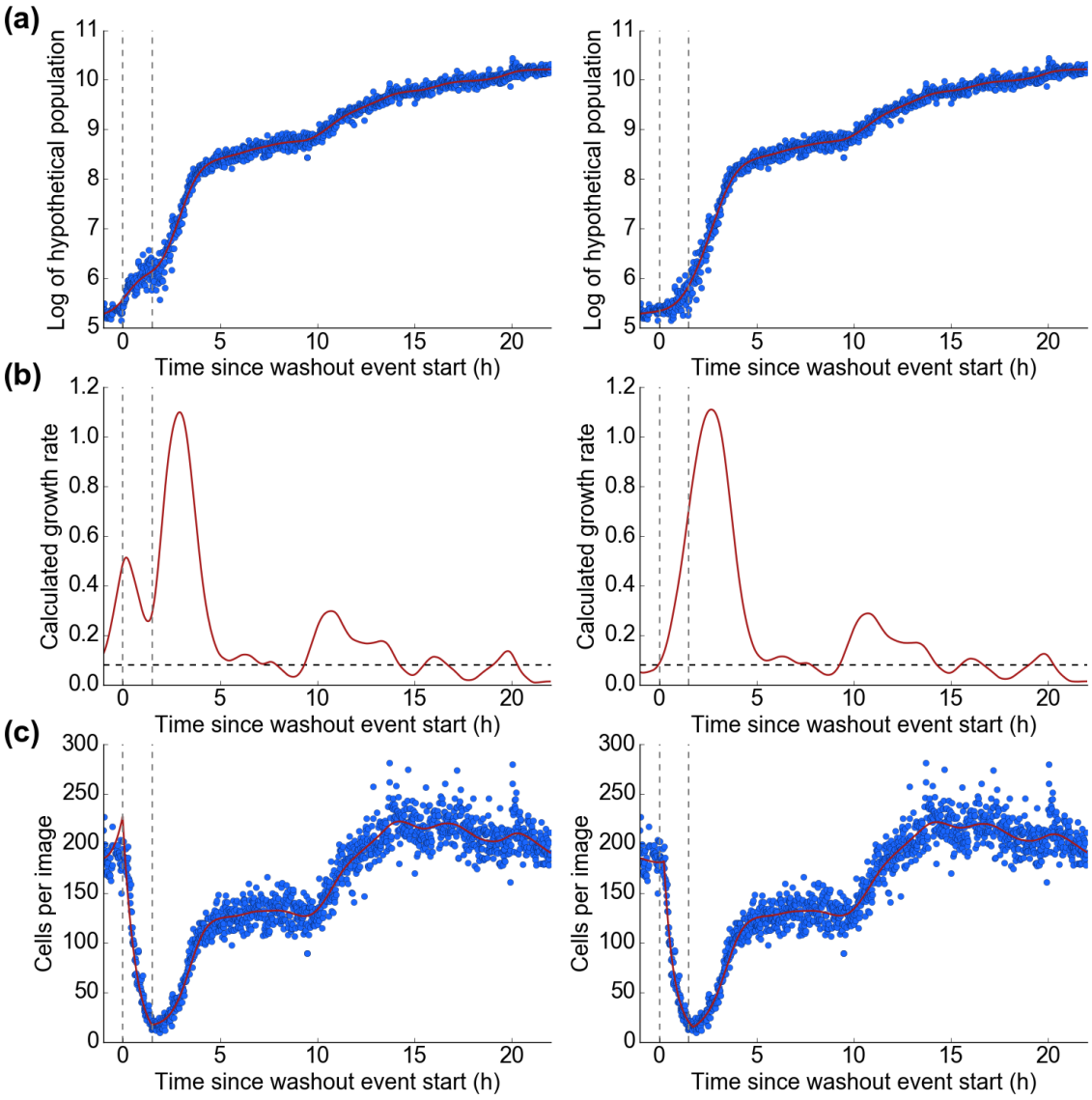


Figure 3.6: Spline fitting and imaging delay correction. Left column: uncorrected spline fits. Right column: spline fits corrected to account for delay between cells being drawn from culture and arriving in microscope imaging volume. (a) Actual spline fits to data, with data adjusted to remove effect of dilution. Dashed lines correspond to washout event start and end, in experiment time. (b) Calculated growth rates based on spline fits, with visible distortion in calculated growth rates when dilution rate changes in uncorrected fits. Horizontal dashed line corresponds to the basal dilution rate outside of washout events. (c) Spline fits with effect of dilution added back in and plotted against actual cell counts from data.

The means and variances over the bagged spline fits was also used to estimate the time-dependent specific growth rate $r(t)$ during the recovery from each washout event as shown in Fig. 3.7, and subsequently to estimate the number of generations up to time T in an experiment by $N_g(T) = \frac{1}{ln(2)} \int_0^T r(t)dt$.

### 3.7.1 Optical density spline analysis

In instances where cells are too dim to image reliably, optical density data can also be used to generate estimates planktonic population growth rates. Our spline analysis of optical density data is largely identical to our analysis of single-cell data, and as optical density measurements occur simultaneously with changes in system dilution rate, artifacts due to time-delayed measurements are never present. However, optical density data suffers from more complicated problems. Because growth rate estimation depends on a logarithm, data used for growth rate estimation cannot be 'floating'; specifically, growth rate estimation is sensitive to the value corresponding to zero density. However, focusing the microscope in our systems requires a high minimum density of cells to start an experiment, making measurement of this value at the beginning of an experiment impossible. Furthermore, the voltage corresponding to 'zero density' appears to change over the course of the experiment as the vial is moved to check for overflow and possibly due to confounding factors such as wall growth.

To work around these issues, we assume that the 'zero density' voltage changes slowly - at least over the course of many hours - and use the effect of the washout events to estimate the zero density voltage. Specifically, because there is a delay before the population growth rate of cells changes following nutrient upshift, the measured optical density during a washout event roughly approximates exponential decay towards zero population. Fitting to this curve therefore gives us a locally-accurate estimate of the 'zero density' at the end of each washout event. The difference between this voltage value and our actual measured optical density during recovery therefore allows us to accurately estimate growth rates. The maximum recovery growth rates found via this method, as discussed in Chapter 4, closely approximate planktonic population growth rates determined from microscope images in experiments where cells were bright enough to image, allowing us to use optical density growth rates as a proxy for planktonic growth rates in experiments where cells are too dim to detect.

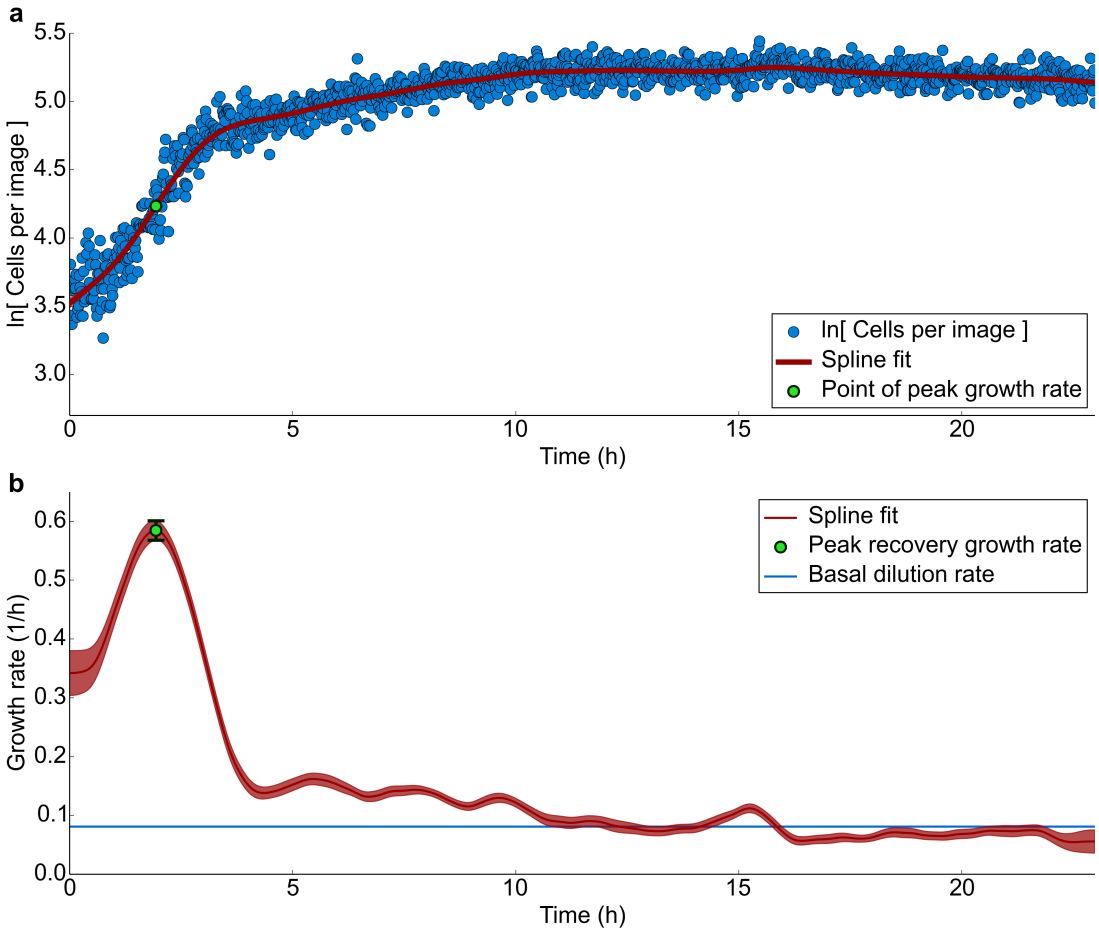


Figure 3.7: Peak recovery growth rate estimation using bootstrap aggregation. (a) Natural log of number of detected single cells, not including aggregates, per image from a continuous-culture device just after a washout event occurred (Washout event ends at time $t = 0$). The red line is a spline fit determined by bootstrap aggregation. (b) Note that for exponentially growing populations $\frac{dln(N(t))}{dt} = r$ where $r$ is the growth rate. The spline regression results in an estimate of $\frac{dln(N(t))}{dt}$ for the fit shown in (a). The shaded region shows the standard error of the distribution of spline fit derivatives at each point. The basal dilution rate of the chemostat (the growth rate at steady state) is shown by the blue line.

# Chapter 4

# Frequency and amplitude dependent population dynamics during cycles of feast and famine

This chapter contains material from published work by Jason Merritt and Seppe Kuehn[1], used with permission of the authors.

This work was partially supported by the Center for the Physics of Living Cells, the National Science Foundation Physics Frontier Center (PHY 0822613 and PHY 1430124), the Carl R. Woese Institute for Genomic Biology, and the Department of Physics at the University of Illinois at Urbana-Champaign. The dissertation author was the primary experimental investigator of this work.

Contributions: Seppe Kuehn and Jason Merritt contributed to the conception and design of the experiment, the analysis and interpretation of the experimental results, and the creation and review of the manuscript. Seppe Kuehn determined the model and parameters used to explain the results. Jason Merritt carried out the experiments and wrote the custom software used in the experiment.

Acknowledgements: Plate imaging systems used to measure lag-times by time to colony appearance were designed and constructed by David T. Fraebel. Bacterial strain under study was created by Doeke Hekstra at Rockefeller University. Experimental preparation relied on generous use of equipment by Thomas Kuhlman's lab.

## 4.1 Introduction

It is believed that nutrient concentrations drive a dynamic equilibrium between planktonic and aggregated populations in nature [46], and studies have demonstrated that plasticity in biofilm production plays a significant role in the overall population dynamics of bacteria [45]. With the large aggregated bacterial populations observed during slow but non-zero growth in the preliminary experiments described in Chapter

[1]Merritt, J and Kuehn, S. Frequency- and amplitude-dependent microbial population dynamics during cycles of feast and famine. *Physical Review Letters* **121**, 098101 (2018).

3, it is possible for the dynamics of aggregation and dispersal of aggregate populations to dominate the population response to shifts in nutrient levels before significant growth occurs. Through cyclic application of periods of nutrient excess (feast) and starvation (famine), we confirm that the dynamics of *E. coli* under slow growth are primarily determined by growth and history-dependent patterns of aggregation and dispersal.

We vary the frequency and amplitude of the nutrient fluctuations and observe a strong dependence of the abundance dynamics on both variables. We find that nutrient fluctuations with higher frequency and amplitude drive faster abundance dynamics in planktonic populations. Further, populations subjected to nutrient fluctuations on timescales shorter than 2 days exhibit memory on a timescale that exceeds a generation time. We present a simple model in agreement with our data showing that these phenomena arise from history and substrate dependence in the dispersal of aggregated or adherent bacterial populations. We confirm this model with size measurements of free-floating cell aggregates observed in our microscopes and by showing the observed history-dependent dynamics disappear in the absence of aggregation. Finally, we document a concomitant frequency and amplitude dependence in the lag-phase duration of bacterial populations, as measured by growth of colonies on LB-agar plates.

Our results confirm the importance of the role aggregated cells play in microbial communities, with the ability to both persist under famine conditions and act as cell reservoirs under feast conditions, rapidly dispersing to the fast-growing planktonic phenotype. Furthermore, the unique capabilities of our systems provide insight into dynamic bacterial spatial structure that would be invisible using standard continuous-culture measurement techniques.

## 4.2 Results

Our epi-fluorence microscope-coupled continuous-culture devices continue to image fluorescently labeled *E. coli* at the single-cell level under cycles of feast and famine (Fig. 4.1(a)). We use the same strains and growth conditions described in Chapter 3: a strain of *E. coli* expressing *dTomato* constitutively from the chromosome grown

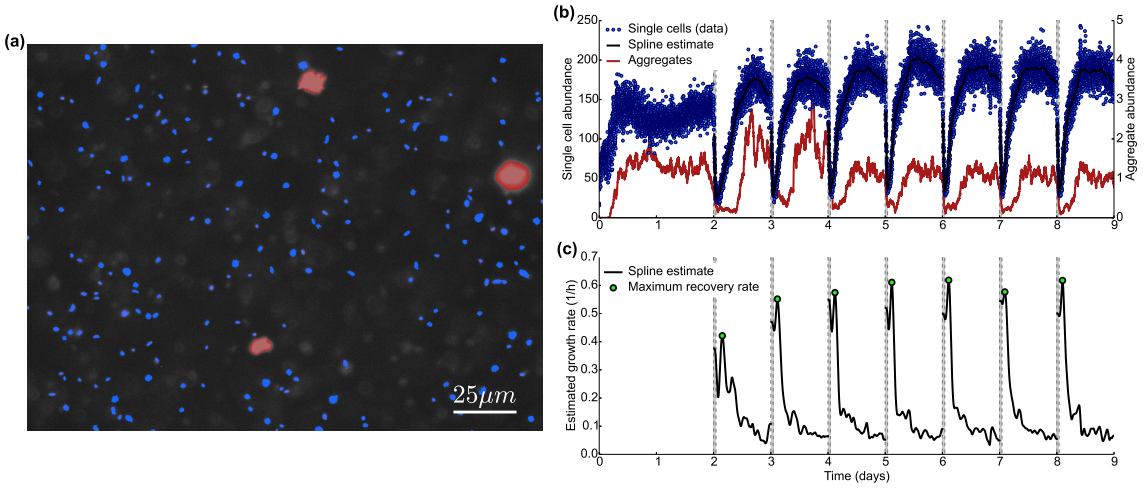


Figure 4.1: *E. coli* abundance dynamics in fluctuating nutrient conditions. (a) Example epi-fluorescence image showing single cells (blue) and aggregates (red) detected by image processing. (b) Number of planktonic cells (blue points) and cell aggregates (red line) detected per image by automated measurement, with aggregate abundances smoothed by a 1 hour rolling average. Dashed vertical lines indicate regions of time where a washout event occurred (1 hour duration). Black lines indicate spline estimates of planktonic population abundances. (c) Instantaneous growth rate for planktonic population estimated from the spline fits shown in (b). Green dots indicate maximum growth rate during recovery.

in M63 minimal medium at 30 °C with low levels of carbon (0.04 % w/v, 2.2 mM glucose), acclimated to the conditions of slow but continuous growth at $D = 0.08\,\mathrm{h}^{-1}$ (doubling time $\tau_d = 8.66\,\mathrm{h}$) for 48 hours prior to the application of the first washout event. We operate six continuous-culture devices in parallel.

During recovery from washout we measure the instantaneous growth rate of the planktonic population. We find this time dependent growth rate exhibits a peak early in the recovery (Fig. 4.1(c)) and report this maximum recovery growth rate (green points in Fig. 4.1(c)).

To study the frequency dependence of the observed abundance dynamics we performed 1 hour washout events which reduced the population by 10-fold with periods ranging from every 72 h to every 24 h from the start of one washout event to the next. We find that the rate of recovery of the planktonic population following a washout event increases the more frequently washout events occur (Fig. 4.2(a)). The change in recovery rate occurs rapidly (by the second washout event), so we conclude that the change in population dynamics is the result of phenotypic processes rather than genetic mutations sweeping through the population (see Chapter 3).

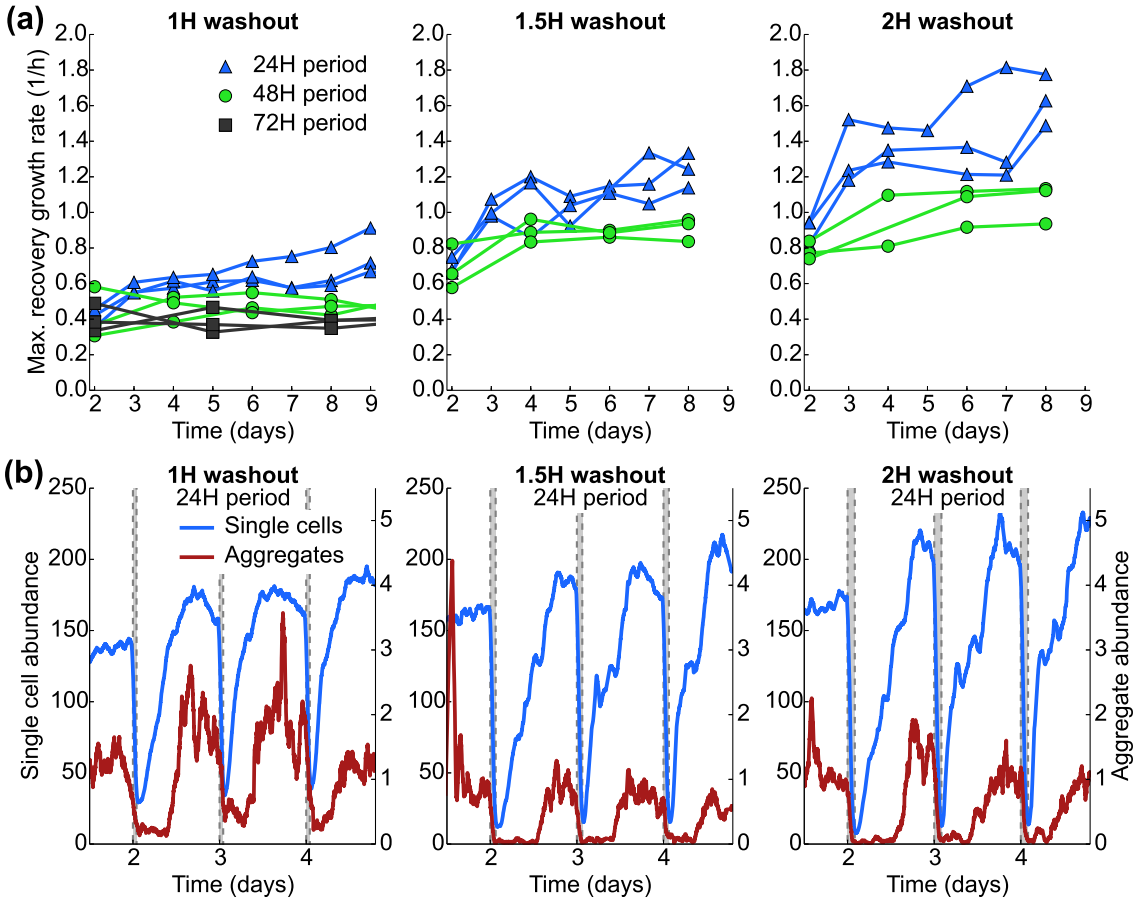


Figure 4.2: Frequency and amplitude dependent abundance dynamics. (a) Maximum growth rates of planktonic populations observed during recovery from a washout event for washouts that occurred every 72 hours (black), 48 hours (green) and 24 hours (blue) with durations varying from 1 hour (1/10 dilution, left panel), 1.5 hour (1/30 dilution, middle panel) and 2 hour (1/100 dilution, right panel). For each condition three independent replicates are shown. Legend in left panel applies to all panels in (a). (b) Example per-image abundances of planktonic populations ($N$) and aggregates ($A$) for systems experiencing washouts every 24 hours with amplitudes of 1 (left), 1.5 (middle) and 2 (right) hours respectively. Each abundance time series is smoothed with a 1 hour rolling average.

We next performed a series of experiments where the amplitude of the washout event was varied. Washout events of larger amplitude occur over a longer period of time, resulting in a larger fraction of the population being washed out and a modestly higher final substrate concentration ($\sim$2.2 mM rather than $\sim$2 mM). We performed washout events with durations of 1.5 h and 2 h and periods of 24 h and 48 h. We find that larger amplitude washout events result in substantially faster growth during the recovery (Fig. 4.2(a)), with maximum recovery rates as high as $1.4\,\mathrm{h}^{-1}$. This rate exceeds previously measured biomass growth rates for *E. coli* in glucose minimal media by at least a factor of four [19], suggesting that our measured planktonic population growth rate cannot be the result of cell division alone. Both the frequency and amplitude dependent dynamics observed via imaging were corroborated by concurrent optical density measurements (Section 4.7). Fig. 4.2(a) is the central finding of this chapter.

One possible explanation for slow growth rates in low frequency perturbation conditions is the presence of phenotypic heterogeneity in the population such as dormant or persistent cells increasing their relative abundance with increasing famine duration [36]. To test this hypothesis we sampled continuous-culture populations every 12 hours over a 60 hour period of famine and used a previously developed assay to detect persistent cells by measuring the time for colonies to appear on agar plates [21]. We found no evidence of persisters in our experiment at relative abundances greater than approximately 1 % regardless of the famine duration. Instead, the time for colonies to form on agar plates was approximately normally distributed regardless of when we sampled the population from the continuous-culture device. However, we did observe a monotonic dependence of the average time to colony formation (lag time) with the duration of the famine, as well as a decrease in the time to colony formation with increasing washout amplitude (Figs. 4.5, 4.10). These results show that the average time for cells to resume growth after a famine decreases with both the frequency and amplitude of environmental perturbations.

We next considered the role cell aggregation plays in the dynamics shown in Fig. 4.2. We performed experiments where the basal dilution rate between washout events was set to zero. In this condition populations do not continually grow between washout events but enter stationary phase as they would in batch culture. Previ-

ous measurements showed that in batch culture lag phase duration also increases with starvation duration [21]. However, the maximum rate of recovery from washout events for planktonic populations in this condition is uniformly slow (maximum recovery rates $\sim 0.3\,\mathrm{h}^{-1}$), with no frequency or amplitude dependence (Fig. 4.19). Critically, we observe little or no aggregation in batch culture conditions, with the entire population being planktonic (see Chapter 3 and Fig. 4.12). This result strongly suggests that the presence of aggregated cells is necessary for the high maximum recovery rates shown in Fig. 4.2. Under this premise, fast recovery rates exhibited by planktonic populations would be driven by the dispersal of aggregated or potentially adherent cells in the community.

## 4.3 Discussion

In light of these results, we sought a model to describe the frequency and amplitude dependent abundance dynamics we observe in bacterial populations growing in fluctuating nutrient conditions which captured the formation and dispersal of aggregated populations. Our model considers populations of planktonic cells $N(t)$ and cells in free floating aggregates or adhered to the vessel $A(t)$. We assume planktonic cells grow at a rate determined by the instantaneous substrate concentration $S(t)$. Aggregates have a characteristic size of approximately 100 cells which we determined from imaging (see Section 4.6.1). Given the large difference in apparent growth rates for planktonic populations between 1 hour and 2 hour washout events we reasoned that the dispersal rate of $A$ should increase with higher levels of available substrate $S$, an assumption which is supported by the literature [75] and our observation that the size of aggregates decreases after washout events (Fig. 4.15). To capture the history dependent recovery rates we assume that the rate of dispersal also depends on the duration of the famine, with longer famines resulting in lower dispersal rates, possibly due to maturation [76]. Finally, we assume that the $A$ population consumes no substrate since bacteria in biofilms have been shown to be in stationary phase [40], and consider global rates of aggregation and dispersal over the entire aggregated population. From these assumptions we construct the following dynamical model:

$$\dot{N} = \mu(S)N - DN - \alpha_1(1 - f(S))N + \alpha_2 \frac{Q}{1+Q} f(S) A Y_{NA}, \tag{4.1}$$

$$\dot{A} = \alpha_1(1 - f(S)) \frac{N}{Y_{NA}} - \alpha_2 \frac{Q}{1+Q} f(S) A - D_{eff} A, \tag{4.2}$$

$$\dot{S} = (S_r - S)D - \frac{\mu(S)}{y} N. \tag{4.3}$$

Here $\mu(S) = \frac{\mu_m S}{K+S}$, $D$ is the dilution rate of the continuous-culture device, and $\alpha_1$ is the rate of $A$ formation from planktonic cells, modulated by substrate levels via $f(S)$. $\alpha_2$ is the rate of $A$ dispersal and is modulated by substrate levels and $Q$, a variable that describes maturation of $A$ by reducing dispersal as the duration of starvation increases. $Q$ increases when nutrients are replete ($\dot{Q} = aQ$ for $S > S_c$) and decreases when nutrients are scarce ($\dot{Q} = aQ$ for $S < S_c$) in an autocatalytic fashion. We chose autocatalytic dynamics for this variable because it is likely driven by a synthesized molecular species [77] or gene products [40] but the exact nature of the dynamics is not critical for the model. $f(S)$ captures the increase in aggregate dispersal rate with substrate levels and is a monotonic increasing function of $S$ ($0 \leq f(S) \leq 1$, $f(S_r) = 1$) which we take to be linear above some threshold $S_{th}$ (see Section 4.9). $Y_{NA}$ is the characteristic size of the aggregates ($\sim$100 cells) and $y$ is the growth yield for *E. coli* on glucose. $D_{eff} = \rho D$, with $0 \leq \rho \leq 1$, provides a proxy for populations adhered to the vessel and therefore not removed by dilution.

Our data permits us to constrain many of the model parameters, including the rate of aggregation ($\alpha_1$), and the rates of accumulation and degradation of $Q$ ($a$ and $b$), $\mu_m$, $K$, and $y$ have been measured previously [78]. We make analytical arguments to estimate the dispersal rate $\alpha_2$ (Section 4.9). The substrate concentrations $S_c$ and $S_{th}$ are not known, but our conclusions are not contingent on the specific values of these parameters, and all other parameters are under experimental control. A full description of the model and detailed reasoning for the parameters used in our simulation is given in Section 4.9.

We numerically integrated Equations (4.1), (4.2) and (4.3) and computed the maximum recovery rate as a function of the frequency and amplitude of nutrient fluctuations. We find that the model recapitulates the core features of our experimen-

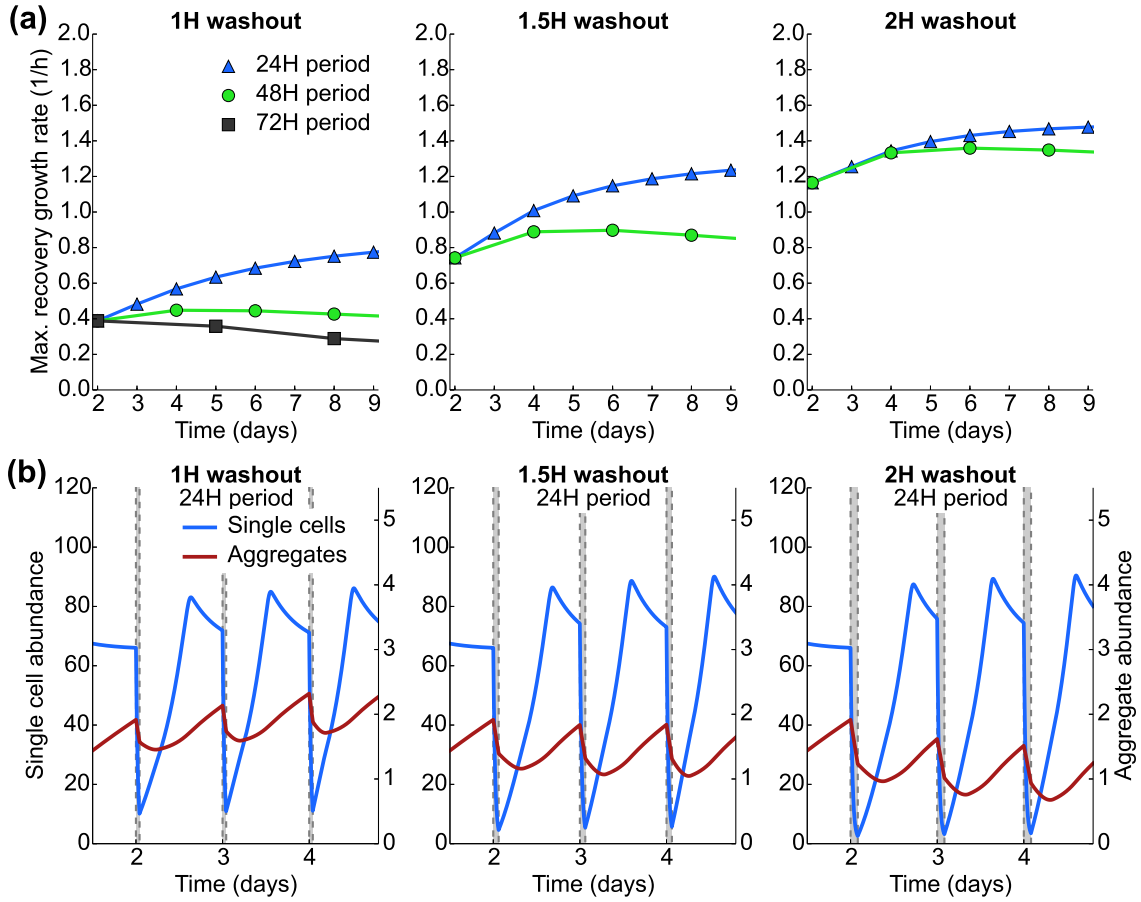


Figure 4.3: Simulated abundance dynamics. Numerical integration of a model describing planktonic ($N$) and aggregated or adherent ($A$) population dynamics. Panels are identical to Fig. 4.2. (a) Shows the maximum growth rate of planktonic populations computed during recovery from a washout event for washouts that occurred every 72 hours (black), 48 hours (green) and 24 hours (blue) with durations varying from 1 hour (1/10 dilution, left panel), 1.5 hour (1/30 dilution, middle panel) and 2 hour (1/100 dilution, right panel). (b) Simulated abundance dynamics of planktonic populations ($N$) and aggregates ($A$) for systems experiencing washouts every 24 hours with amplitudes of 1 (left), 1.5 (middle) and 2 (right) hours respectively.

tal observations, namely the frequency and amplitude dependence of the planktonic population abundance dynamics (Fig. 4.3). The model shows that the dispersal of aggregated or adherent populations can drive the very high planktonic population growth rates we observe experimentally.

We have shown that aggregation or adherent populations respond to increases in nutrient concentrations in a frequency and amplitude dependent fashion. In contrast to recent studies of chemotaxis driven aggregation [77], the dynamics we observe occur despite the fact that our strain lacks the *flu* gene which encodes an adhesion factor (*Ag43*) known to drive aggregation at 37 °C. We suspect that the adhesion dynamics are driven by curli-mediated cell-cell adhesion, which is known to occur at the lower temperature used in this study (30 °C) [77, 79].

It is increasingly clear that non-planktonic bacterial populations are central to metabolic [41], evolutionary [80] and ecological processes [81] in a range of habitats. Our study demonstrates that the statistical properties of environmental fluctuations have strong impacts on the lifestyle of bacterial populations which in turn drive rapid changes in abundance dynamics. In the future, it will be important to investigate the eco-evolutionary origins of the frequency and amplitude dependent dynamics observed here.

## 4.4 Strains and growth conditions

All liquid media used was M63 minimal media with 0.04% (w/v) glucose and 12.5 µg mL$^{-1}$ chloramphenicol. Plates were lysogeny broth (LB) plates, also with 12.5 µg mL$^{-1}$ chloramphenicol. Every phase of each experiment was carried out at 30 °C. Initial flask cultures were grown in shakers operating at 200 rpm, and all continuous-culture devices were constantly stirred at 800 rpm.

Our *E. coli* strain was created by D. Hekstra at Rockefeller University: MG1655 $\Delta fimA$, $\Delta flu$, HK022 att:: ($catP_{\lambda R}$-$dTomato$) $hsdR$.

## 4.5 Lag-time measurement

To measure the lag-time for populations growing in our continuous-culture devices we followed a method described elsewhere [21]. Briefly, cells were sampled from continuous-culture and plated on LB agar plates. Plates were then incubated and continuously imaged. Image processing was used to determine the time to colony formation and the rate of colony growth.

### 4.5.1 Plate preparation protocol

We initially recorded considerable variability in our plating data due to the sensitivity of *E. coli* colonies to the conditions of the plate, such as initial temperature and water content due to evaporation and condensation. To standardize our methodology and ensure the consistency of our results, we developed the following protocol for preparing plates for imaging.

LB-agar (1.5 % w/v, with chloramphenicol) is poured at 50 °C into 100 mm diameter plates 10 days before the first plate is imaged, using a sterilized graduated cylinder to measure out 18 mL per plate. Shortly after solidifying, plates are inverted and left on a lab bench top at room temperature for 2 days, then individually sealed in parafilm and transferred to a refrigerator at 4 °C for 7 days, by which time the plates are assumed to have reached an environmental steady state. Starting on the $7^{\text{th}}$ day, plates are taken out of the refrigerator as needed 24 hours before they are scheduled to be imaged. The plates taken from the refrigerator have their parafilm removed and are placed in an incubator at 30 °C to thermalize at the temperature of the experiment for 24 hours. Finally, samples from the continuous-culture devices are spread onto these plates, and the plates are grown and imaged at 30 °C.

Plates were imaged every 5 or 10 minutes for 24 hours using a commercial webcam housed in a light tight box. An LED strip controlled by a relay was used to illuminate the plates only during imaging ($\sim$1 second for each acquisition).

### 4.5.2 Colony image processing

Depending on the experiment, an image of each plate was taken every 5 or 10 minutes. Circular regions of interest (ROIs) were determined by hand for each imaged plate

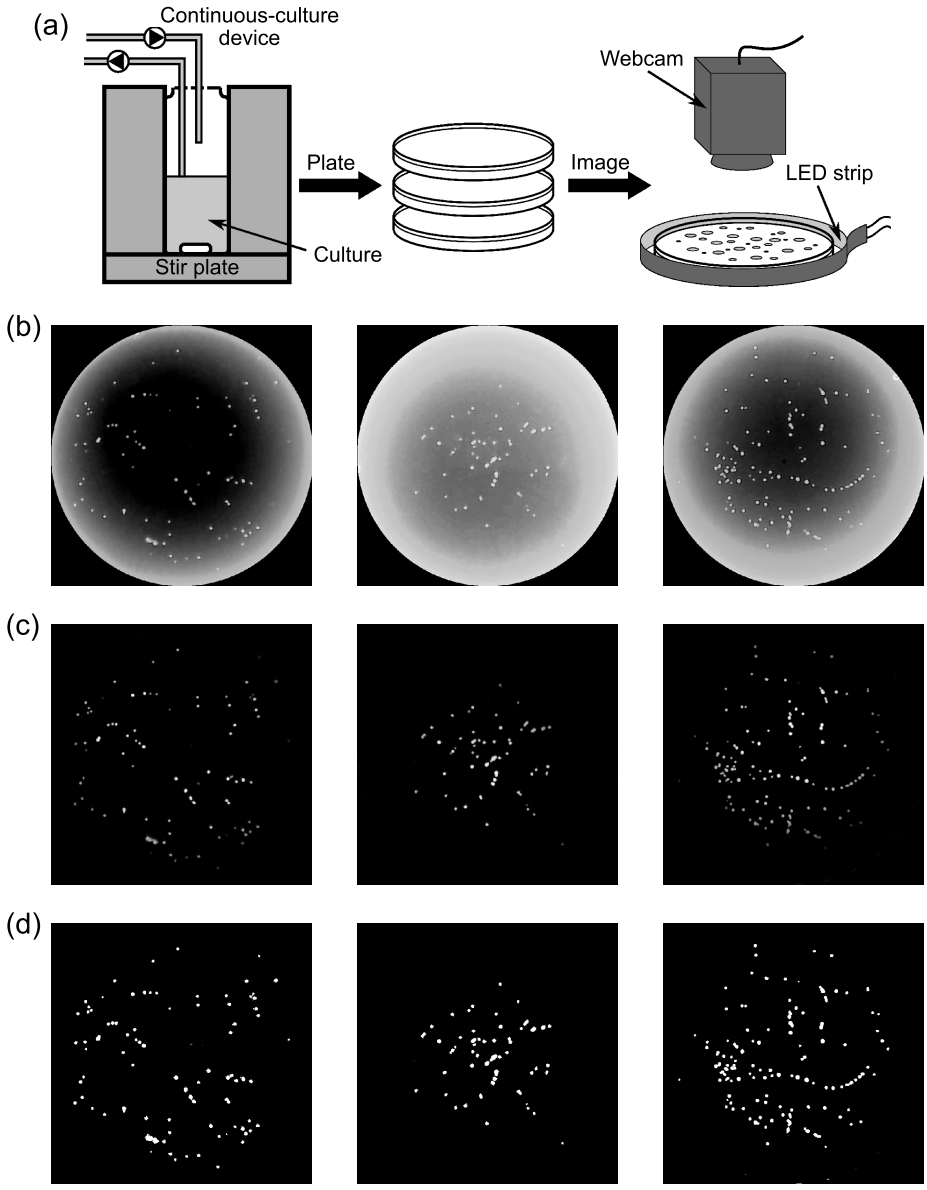


Figure 4.4: Plate imaging technique. (a) Schematic of the measurement. Cells are sampled manually from a continuous-culture device and plated. A webcam images plates housed in an environmental chamber maintained at 30 °C. (b) Circular regions of interest (ROIs) from images of three example plates. Note that intensity increases towards plate boundaries due to plates being lit from the sides by LED strips. (c) Background-subtracted versions of the images shown in (a). (d) Thresholded versions of the images shown in (b), showing detected colonies.

(Fig. 4.4(b)). These ROIs were background-subtracted using a median filter on at least 10 images, taken over a period of 100 minutes, before the first colonies appeared in any experiment (Fig. 4.4(c)), and were then globally thresholded using a fixed value across all experiments (Fig. 4.4(d)). ROI size was controlled by hand to exclude light reflection artifacts near the edge of each plate without excluding any colonies on the plates.

For each thresholded image, SCIKIT-IMAGE functions were used to find and record all information about all connected regions above the threshold (including both colonies and artifacts). Next, detected objects appearing in the same location were associated across sequentially acquired images to allow size tracking in time. Since imaging artifacts do not persist across multiple images they are filtered out at this step. Finally, only colonies which did not merge with other colonies during growth are included in the final analysis, because colonies very near each other on the plate affect each others' growth. However, for colonies evenly distributed on a plate, previous work by Levin-Reisman *et al.* [21] showed no effect on the growth of neighboring colonies as long as the total number of colonies on the plate remained below 200. We stay below this threshold in our experiment.

The first image in which a colony appeared was used to define its 'time to colony appearance' (Fig. 4.5(b)), which we found generally followed a normal distribution (Fig. 4.6). Our data indicated that colony area increased linearly in time over the first 70 minutes of detection (Fig. 4.7); therefore, the colony rate of area increase (Fig. 4.5(c)) was determined by a linear fit to the colony's size over the first 70 minutes after its appearance.

Because our plate illumination results in a background brightness gradient increasing radially from the center of the plate (Fig. 4.4(b)), we checked the time to colony appearance and colony growth rate in our experiment against the background brightness of their location on the plate (Fig. 4.8(a)) and found an increase in time to colony appearance and a decrease in colony growth rate for colonies growing in regions where the background intensity of the plate exceeds a pixel intensity of 100. Our reported qualitative trends for these variables, shown in Fig. 4.5, remain intact with these colonies discarded (Fig. 4.8(c)).

Total numbers of colonies were also counted by hand from the physical plates for

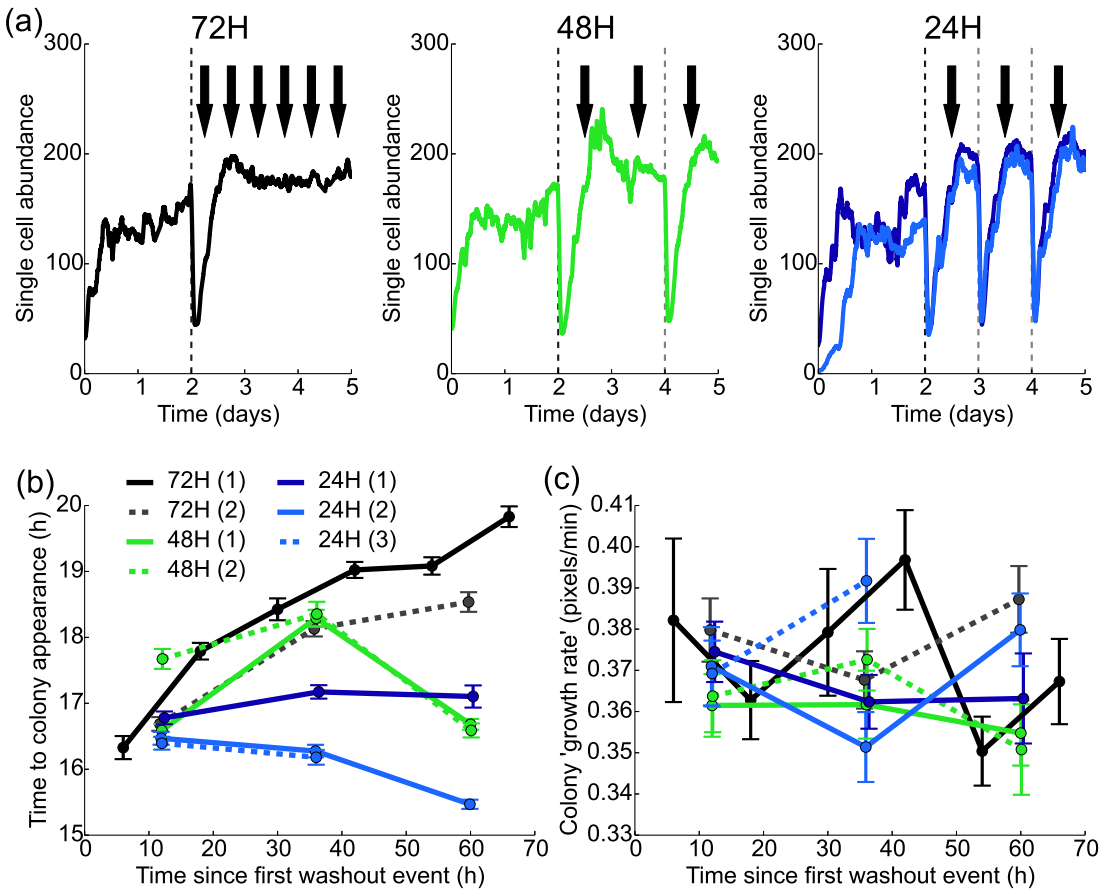


Figure 4.5: Lag-phase duration depends on washout event frequency. (a) Single cell abundance (cells per image) time series for four primary data sets. Dashed lines indicate washout events, and arrows indicate time points when sampling occurred. (b) Mean time to colony appearance for populations experiencing 1 h washout events at periods from 72 h to 24 h as a function of time since the first washout events. The legend indicates (period, replicate number). Experiment '24 (3)' ended before the final time sampling point due to computer failure, and experiment '48 (2)' was performed before the plate preparation protocol was finalized and exhibited some signs of resulting aberrations in data due to plates losing moisture through evaporation. Uncertainties indicate standard error of the mean. (c) Mean colony growth rate measurement, using colony rate of area increase over the first 70 minutes of colony detection in webcam images (Fig. 4.7) as a proxy. Error bars in all panels indicate standard error of the mean.

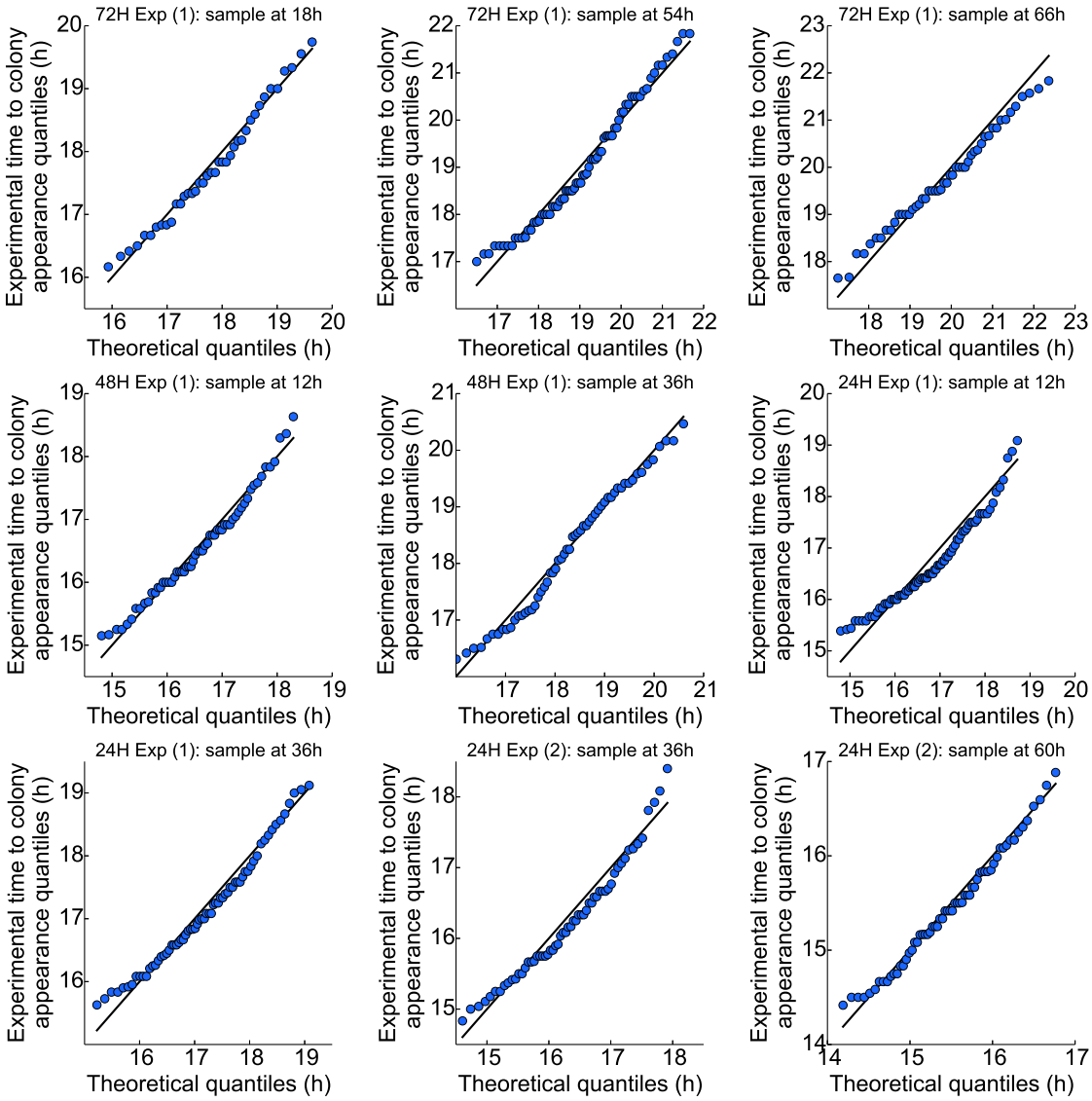


Figure 4.6: Lag-phase duration is normally distributed. Quantile-Quantile (qq) plots of time to colony appearance for plates from various time points and experiments in Fig. 4.5. Each panel includes colonies from two plates. Theoretical distributions are in each case normal distributions with the sample mean and standard deviation from the associated experimental dataset. The black line is a reference representing an experimental distribution perfectly matching a normal distribution; points show the real quantiles of the experimental dataset matched to the quantiles of the theoretical distribution. In each graph, quantiles are evenly spread over the range 0.05 to 0.95.

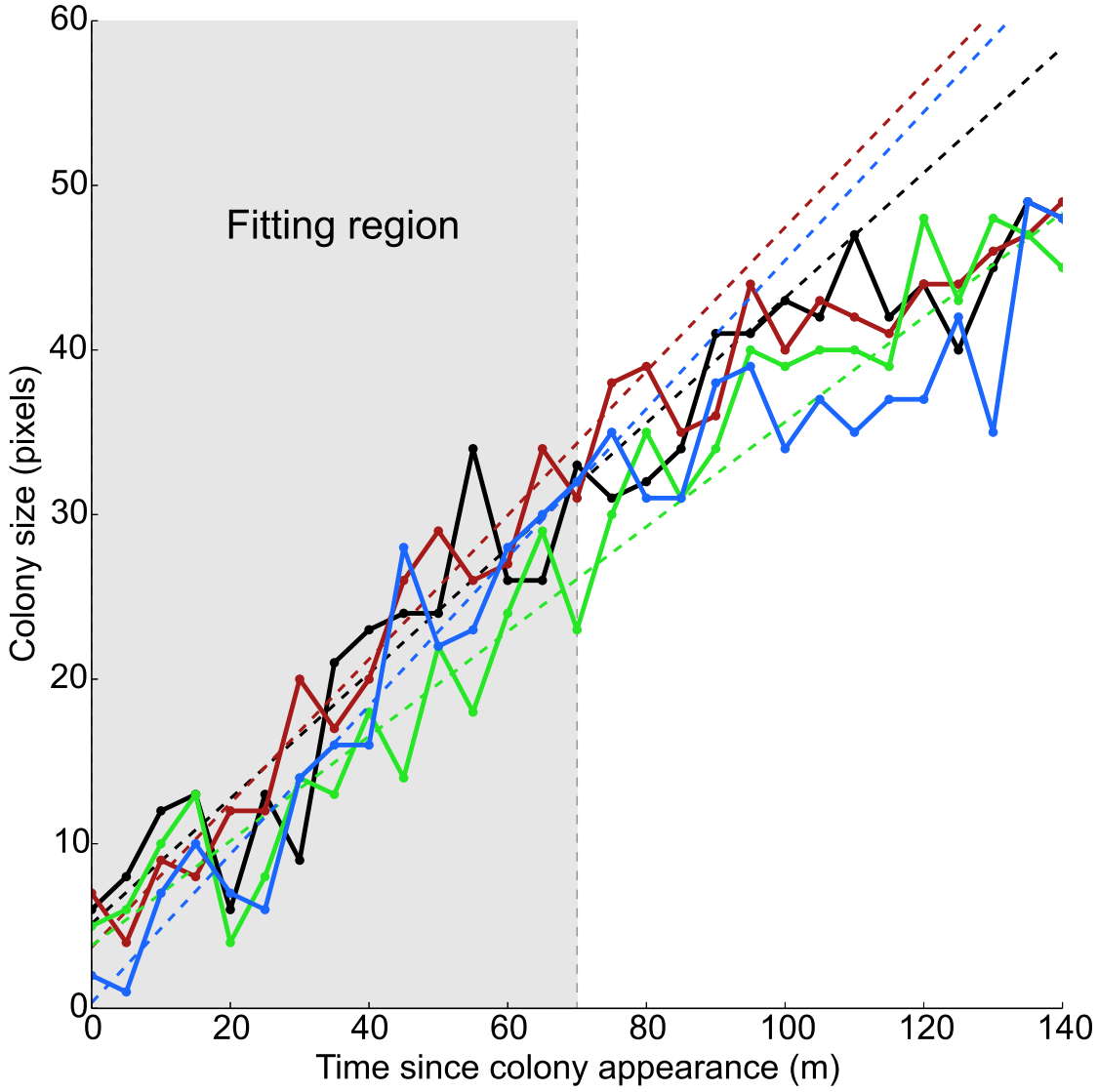


Figure 4.7: Colony growth rate measurement. Growth in colony area following initial detection of colony on plates in webcam images for four representative colonies. Colony growth is roughly linear in time over the first 70 minutes.

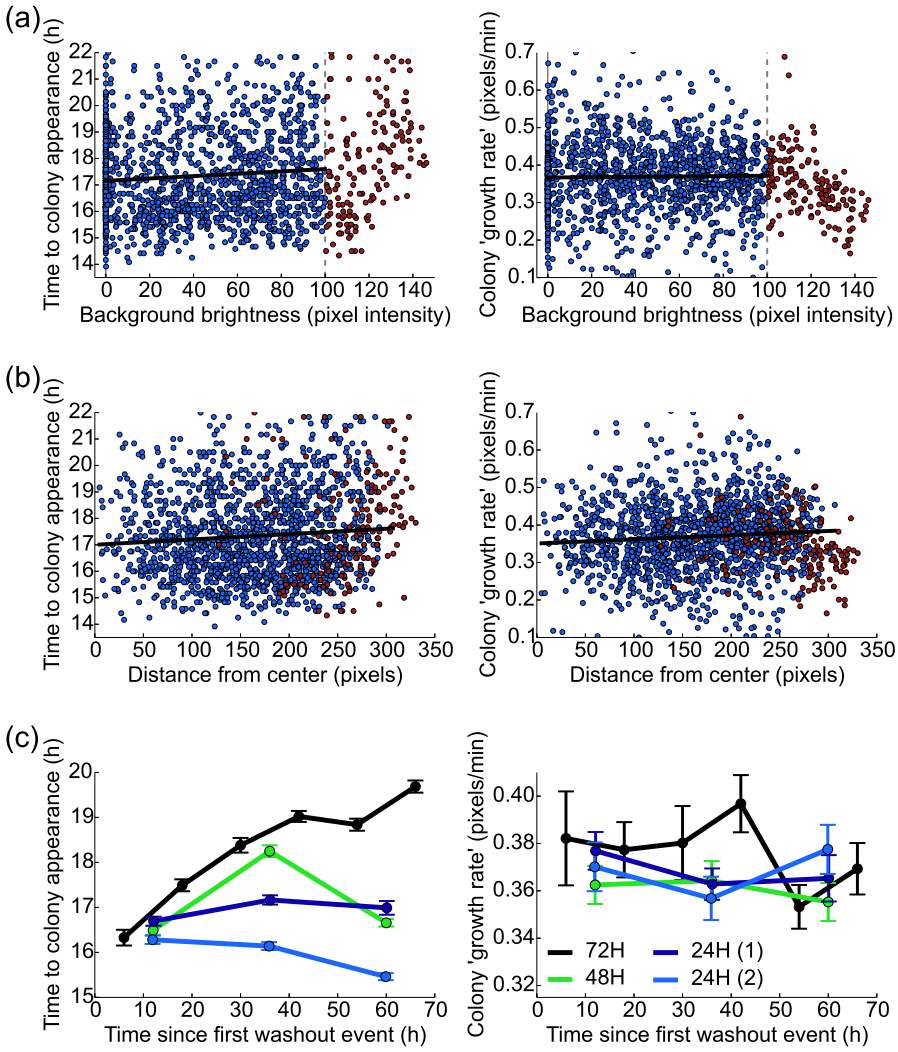


Figure 4.8: Effect of background brightness and colony position on measured colony parameters. (a) Time to colony appearance and colony growth rate plotted against background plate brightness at colony location. When the local background brightness exceeds a pixel intensity of 100 it begins to affect the accurate detection and measurement of colonies. Linear fits shown are calculated only over colonies with a background brightness of less than 100, and yield slopes of $(4.45 \pm 1.33) \times 10^{-3}$ h (pixel intensity)$^{-1}$ (left) and $(4.78 \pm 7.99) \times 10^{-5}$ pixels min$^{-1}$ (pixel intensity)$^{-1}$ (right). (b) Time to colony appearance and colony growth rate plotted against distance from center of plate. The location of colonies on the plate has a minor effect on the measured parameters when colonies growing at bright locations are separated out. Linear fits shown are calculated over only colonies with a background brightness of less than 100, and yield slopes of $(2.02 \pm 0.65) \times 10^{-3}$ h pixels$^{-1}$ (left) and $(1.11 \pm 0.39) \times 10^{-4}$ min$^{-1}$ (right). (c) Modified versions of primary data sets from Fig. 4.5(b),(c) using only colonies below the plate brightness threshold in (a), showing that the qualitative trends are unaffected.

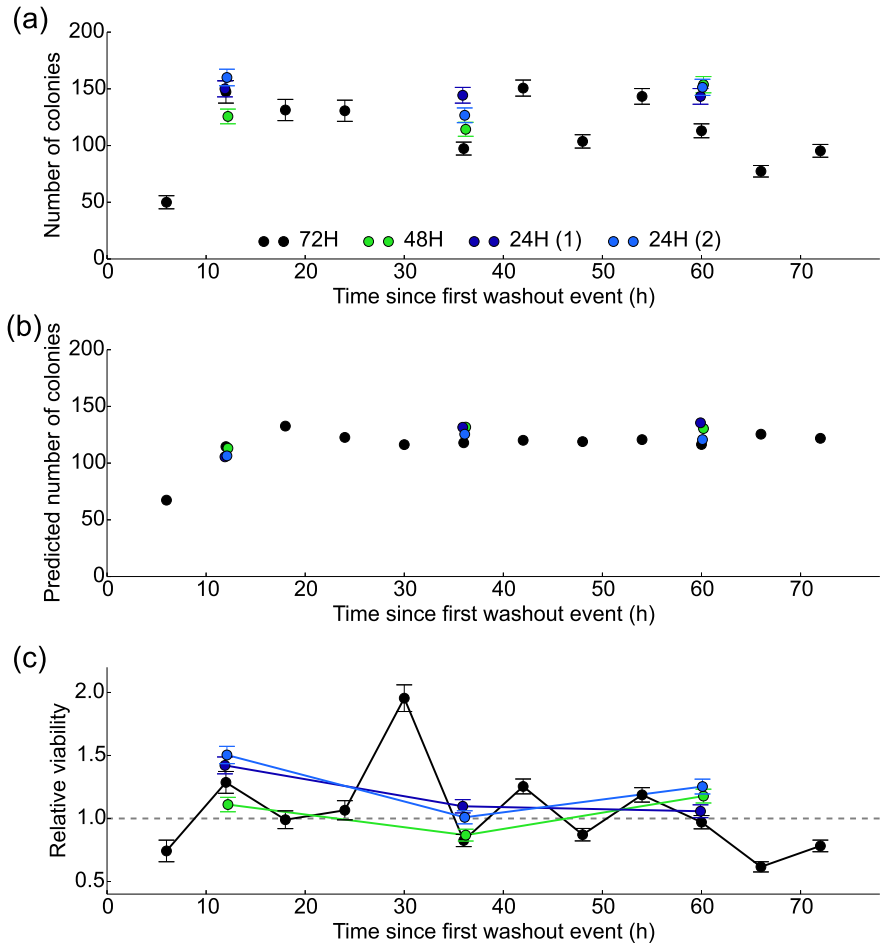


Figure 4.9: Cell viability as a function of starvation duration. (a) Average number of colonies counted over three plates by hand from the data sets in Fig. 4.5(b) plotted with solid lines. The number of colonies per plate in our experiment corresponds to colony-forming units in a 100 µL sample from a $5 \times 10^5$-fold dilution of our system cultures into phosphate-buffered saline. Counts shown here include additional plates not imaged by webcam, as well as additional time points. Note that the total cell abundance in the continuous-culture device is also varying in time as shown in (b) and Fig. 4.5, and the low number of colonies at the 6 hour time point is predicted by the smaller population in the continuous-culture device at that time. The high number of colonies at 30 hours is attributed to a single plate (not imaged by webcam) with over 4 times the expected number of colonies, possibly the result of inadvertently spreading a cell aggregate over the plate. Uncertainties shown assume Poisson counting error in colony counts. (b) Predicted number of colonies at the sampling time points based on cells per image in microscope data and earlier calibration (Section 3.6) yielding a conversion factor of 1.48 cells per image corresponding to 1 colony per plate. (c) Relative viability of cells over time, defined as the measured number of colonies divided by the number of colonies predicted by the number of cells per image, showing no decline in cell viability until at least 60 hours after the first washout event.

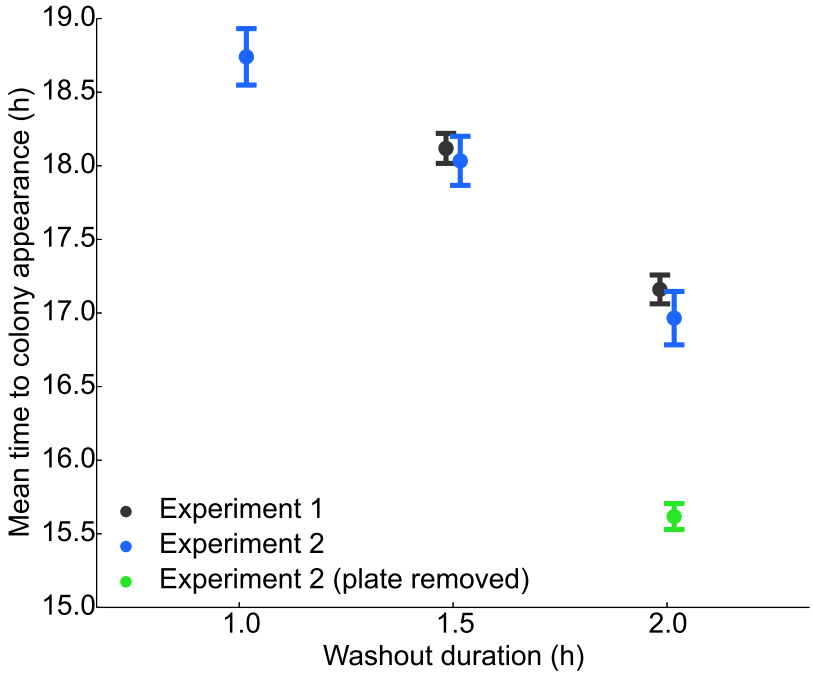


Figure 4.10: Lag-phase duration depends on amplitude of washout events. All cells were sampled 12 h following the start of the first washout event in a system which experienced a washout event with duration between 1 h and 2 h. The 'plate removed' data point refers to the removal of a single plate which appeared to have a dramatically different distribution of times to appearance as compared to other plates from the same experiment, most likely due to unexpected evaporation of the plate. Note that due to substantial modifications to the imaging apparatus between experiments, quantitative comparisons to Fig. 4.5(b) are not valid.

statistics on cell viability over time (Fig. 4.9).

### 4.5.3 Lag-time measurements: frequency dependence

Lag-time measurements were carried out as described above in continuous-culture devices with 1 h washout events at washout schedules of 24 h, 48 h, and 72 h, with multiple sampling times over a period of 72 h following the first washout event (Fig. 4.5(a)). We observe an increase in lag-time - as measured via average time to colony appearance - with increasing duration of starvation (Fig. 4.5(b)).

### 4.5.4 Lag-time measurements: amplitude dependence

Lag-time measurements were also carried out at a single point, 12 hours after the beginning of the first washout event, in systems undergoing 1 h, 1.5 h, and 2 h washout

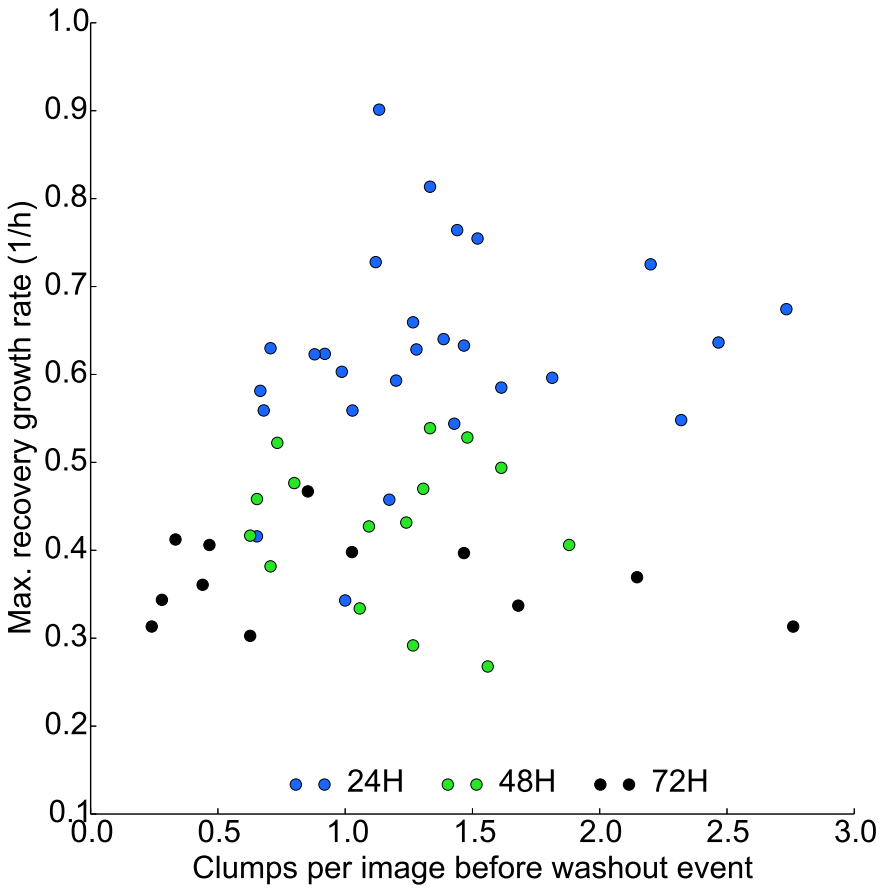


Figure 4.11: Number of aggregates prior to washout event plotted against spline-estimated maximum growth rate during recovery in 1 h washout event conditions. The number of aggregates prior to a washout event is estimated by an average over 15 minutes of data immediately before the washout event.

events (Fig. 4.10). These experiments were carried out in a modified imaging apparatus that permitted higher throughput plate imaging. This resulted in different illumination profiles of the plates and therefore quantitative changes in the minimum detectable colony size. As a result, direct numerical comparisons to Fig. 4.5(b) are not possible, but the average times to colony appearance from this set of experiments indicates a decrease in lag time with increasing washout amplitude (Fig. 4.10).

## 4.6 Cell aggregation measurements

Our systems exhibit complex dynamics in the form of cell aggregation into large free-floating aggregates following the recovery after a washout event (see Chapter 3).

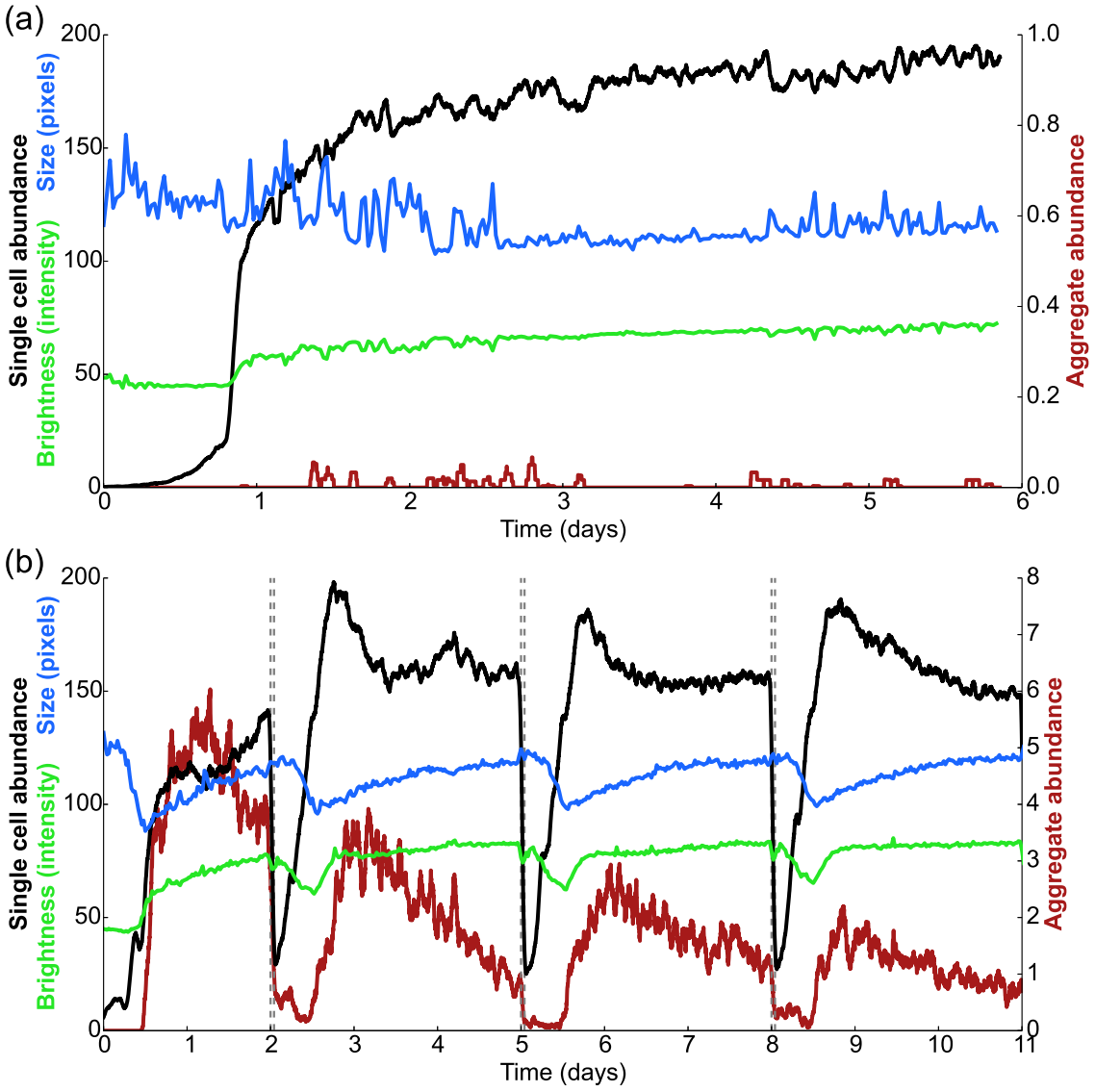


Figure 4.12: Dynamics of cell size. Per-image single cell abundance, aggregate abundance, mean cell size (in pixels) and mean cell brightness (in pixel intensity) plotted for (a) a population growing in batch culture ($D = 0$) and (b) a continuous-culture system with a washout event schedule of 72 hours. Axis label colors correspond to colors of traces. Single cell and aggregate abundances are each smoothed with a 1 hour rolling average. Cell size decreases in batch culture but increases in continuous-culture even in starvation conditions; a cell size of 100 pixels corresponds roughly to an area of $3.1\,\mu m^2$ in the focal plane. Pixel intensity is in the range 0-255, and the population mean cell brightness is calculated as a population average over the mean brightness of each individual cell. Note that the apparent spike in cell abundance prior to $T = 1$ d as the pixel intensity increases above 50 is an artifact due to population brightness increasing to the point all cells are detected. Prior to this sudden increase, only bright cells are counted; after the increase, cells remain bright enough to be correctly segmented for the remainder of the experiment in all continuous-culture conditions.

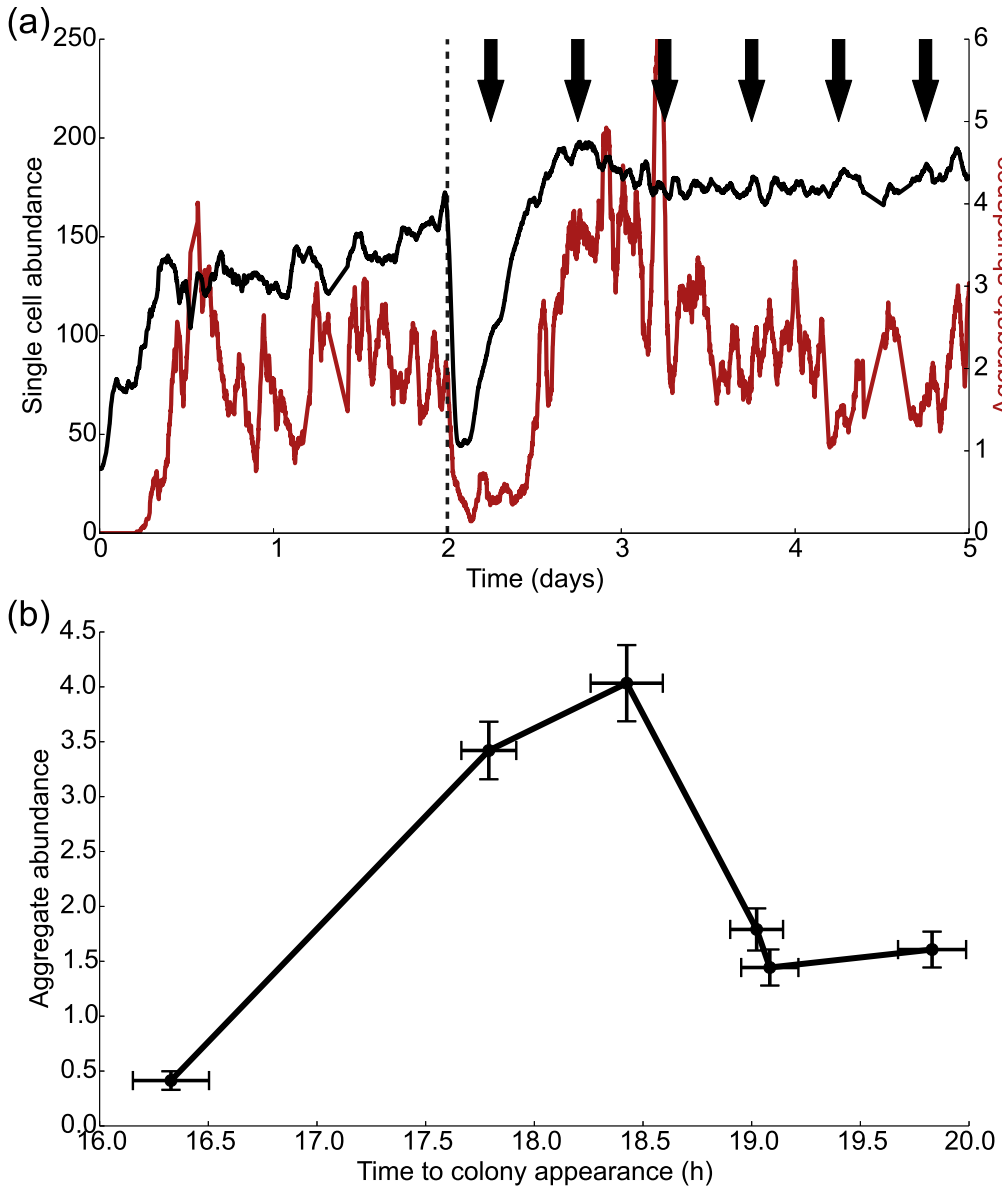


Figure 4.13: (a) Single cell and aggregate per-image abundances during the 72 h experiment shown in Fig. 4.5(a). Single cell and aggregate abundance are each smoothed with a 1 hour rolling average. Black arrows indicate sampling times. (b) Number of aggregates vs. mean single-cell lag time, using time to colony appearance on plates in webcam images as a proxy for lag time. Number of aggregates shown is averaged over one hour of data centered on the sampling time. The time to colony appearance is monotonic increasing with sampling time, and the variation in aggregate abundance shows the growth and decline of the aggregate population following recovery from a washout event, similar to the experiment shown in (Fig. 4.12(b)). Indicated uncertainties are standard error of the mean.

Statistics on aggregate abundances are complicated by very low abundances ($\sim$1 per image), and our estimated measured aggregate abundances do not appear to have a simple relationship with population recovery rates (Fig. 4.11), individual cell size (Fig. 4.12), or lag-phase (Fig. 4.13).

### 4.6.1 Distributions and dynamics of aggregate sizes

We studied the distribution of object sizes for all objects detected by our image processing algorithm. We constructed binned probability histograms of the size of all objects detected during the 9 day experiment window, with logarithmic bins of object area and each bin normalized by the total number of objects. These histograms contained two peaks, one corresponding to planktonic cells and one corresponding to aggregates (Fig. 4.14). From these histograms we note that the characteristic cross-sectional area of aggregates in our images is approximately 29 times greater than that of single cells - the latter have an average size (in the plane of focus) of approximately $4.15\,\mu m^2$ (135 pixels), with aggregates having a size of approximately $121\,\mu m^2$ (3910 pixels). This gives an estimate of the number of cell volumes contained in an aggregate volume of $(\frac{121}{4.15})^{1.5} = 157$ cell volumes per aggregate. Assuming a packing fraction (fraction of aggregate volume that is cells) of about 0.64 - typical for a close random packing of spheres - yields our rough estimate of approximately 100 cells per aggregate. These histograms also corroborate our claim that the batch-culture conditions ($D = 0$ between washout events) result in little or no aggregation.

We next studied the dynamics of aggregate sizes over time. To do this we constructed distributions of aggregate area in the plane of focus for non-overlapping 3 hour time windows throughout the time series for all experiments. We then plotted the average of these distributions as a function of time and found that the average aggregate size decreased after washout events in all conditions (Fig. 4.15). We demonstrate that even following the first washout event, aggregates from systems undergoing higher amplitude washout events experience a greater decline in the mean size of aggregates (Fig. 4.16). These observations strongly support our modeling assumption that increases in nutrient levels drive aggregate dispersal.

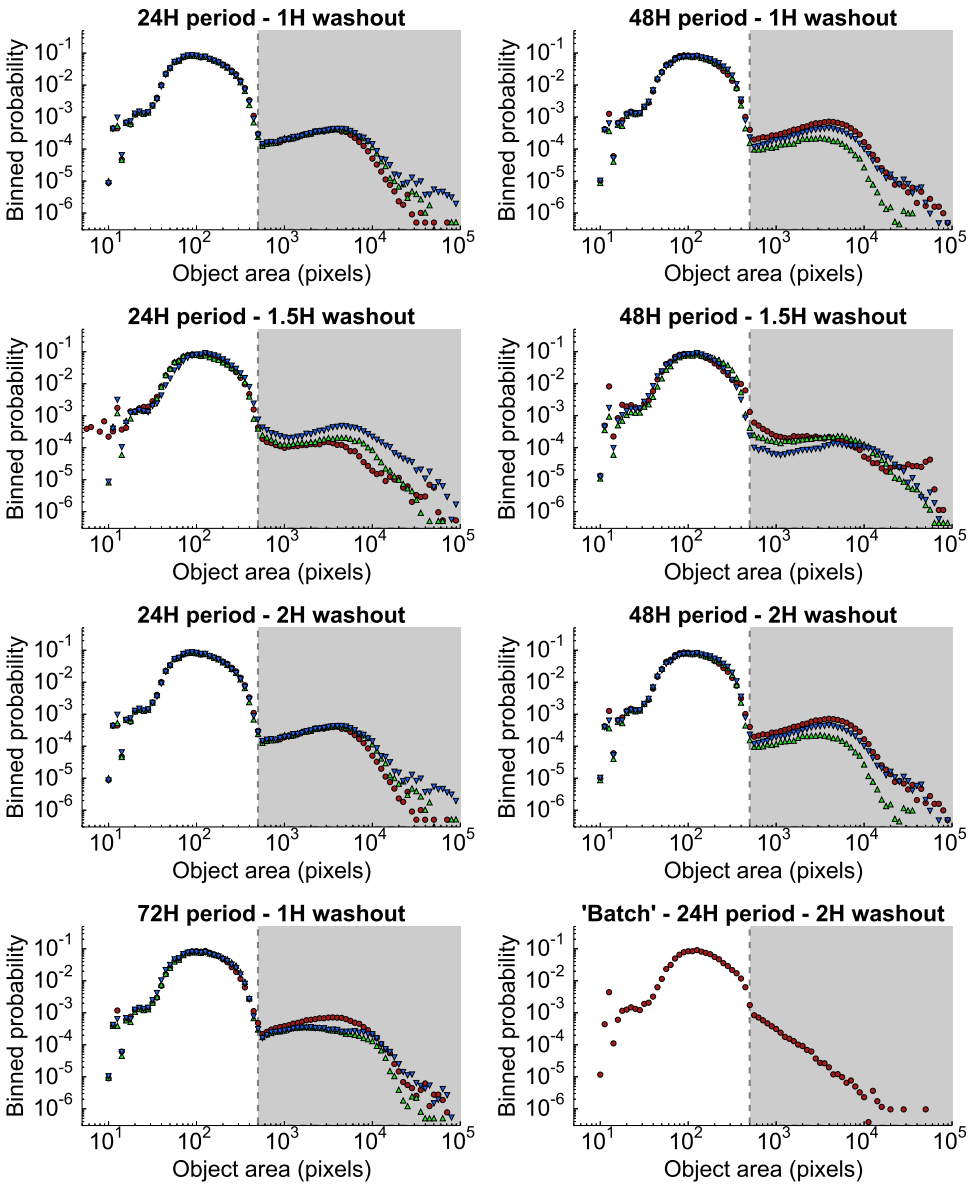


Figure 4.14: Binned probability histograms of sizes of all objects detected during image segmentation under different experimental conditions over the 9 day experiment window, with logarithmic bins of object area and each bin normalized by the total number of objects. Two distinct peaks in the distribution are clear under continuous-culture conditions, corresponding to the most common size ranges for single cells and aggregates, whereas in a batch experiment no higher mode of the distribution is observed. We note that to prevent double-counting of bright cells, because the tail of the distribution of single-cell sizes drops off rapidly by approximately 500 pixels (indicated by the dashed line), the aggregate image segmentation routine does not detect objects below 500 pixels in size. As a result, all objects shown here in unshaded regions are classified in abundance time series as single cells, and the vast majority of objects shown here in shaded regions are classified as aggregates.

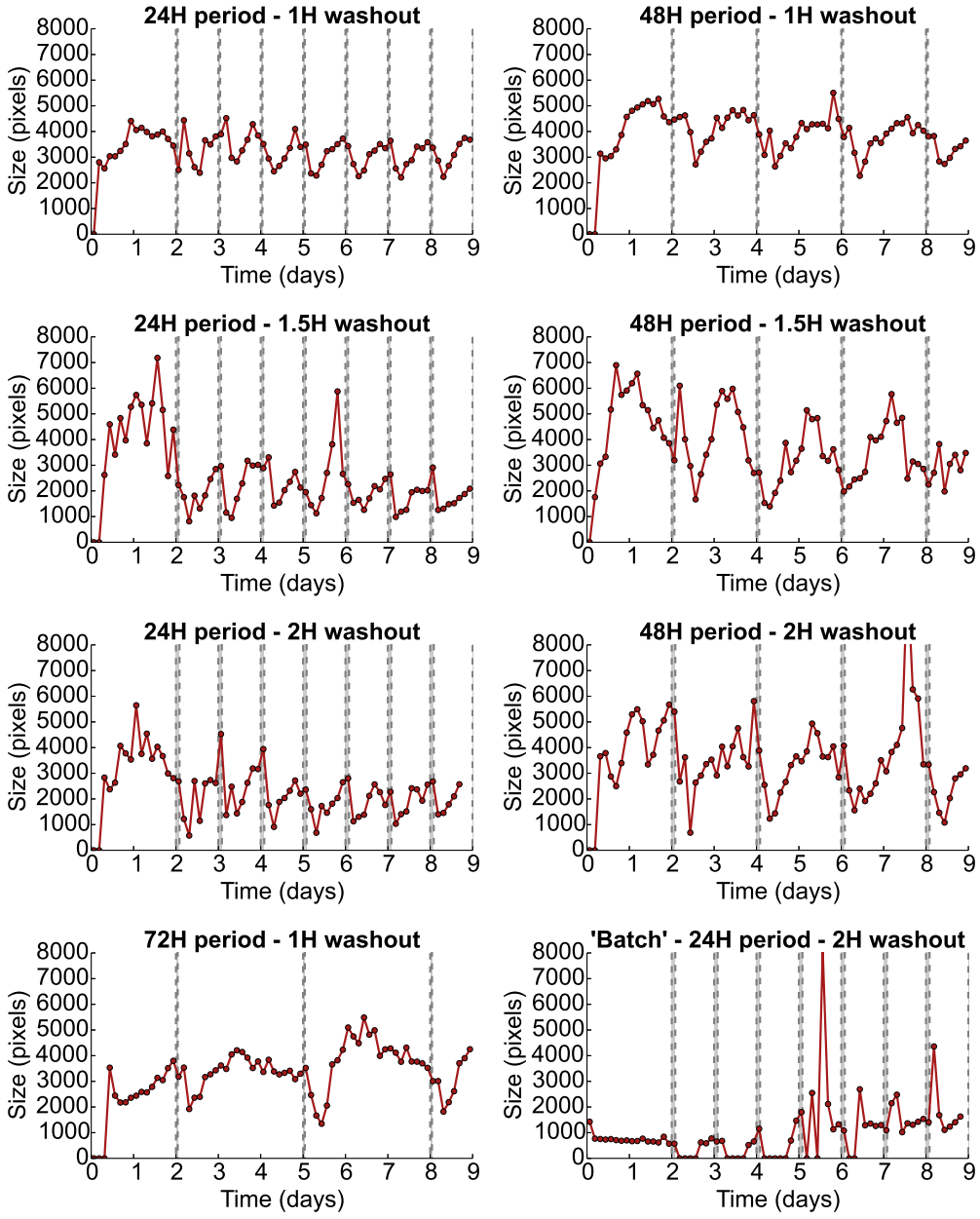


Figure 4.15: Aggregates decrease in size after washout events. Binned time series (3 hour windows) of average aggregate sizes across different experimental conditions, showing a rapid decrease in aggregate size following a washout event, followed by a steady increase, with additional dynamics present in systems with long washout periods. Shaded regions indicate washout events, and an average aggregate size of zero indicates the absence of aggregates. Note that the increase in aggregate size in the 'batch'-style experiment from between days 5 and 6 correlates to the rise in aggregate population in that experiment shown in Fig. 4.19(b) and a rise in the observed maximum recovery rate by optical density as shown in Fig. 4.19(c).

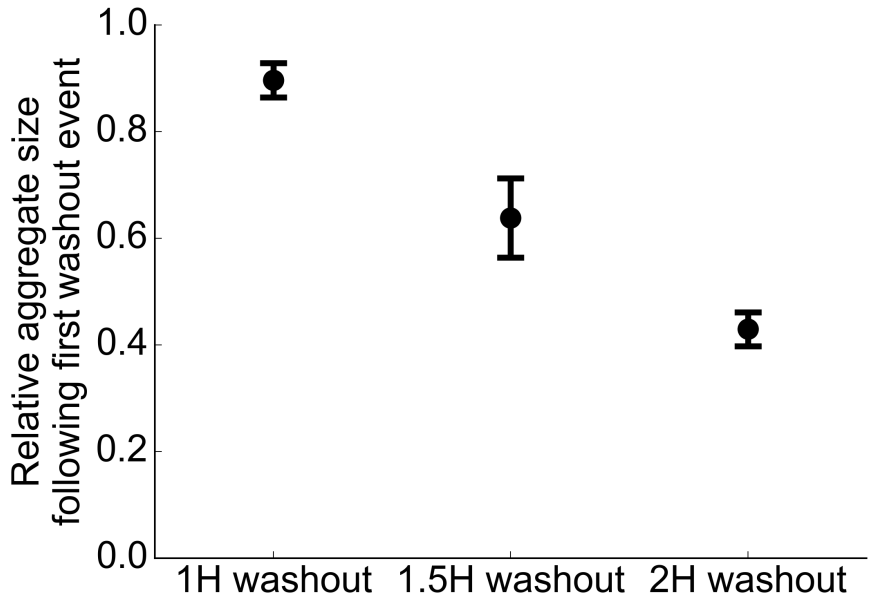


Figure 4.16: Change in average aggregate size before and after the first washout event in communities experiencing different washout event amplitudes. We compute the mean size of all aggregates detected in a six hour window before the first washout event (42 to 48 hours after start of the experiment) over all communities experiencing a particular washout event amplitude. Second, the average size of all aggregates in all communities for a given washout event amplitude is computed in a six hour window beginning three hours after the washout event begins (51 to 57 hours after the start of the experiment). Using these averages, we compute the fractional change in average aggregate sizes before and after washout events. Error bars show standard error of the mean. The increase in dispersal for populations experiencing larger amplitude washout events holds even if we disaggregate the data by community (data not shown).

### 4.6.2 Time series of aggregate abundances

For completeness, we present representative aggregate abundance time series (smoothed with a rolling average) under 48 h washout periods (at washout durations of 1 h, 1.5 h, and 2 h) and a 72 h washout period (at a washout duration of 1 h) in Fig. 4.17. Representative aggregate abundance time series under 24 h washout periods for all washout durations are presented in Fig. 4.2(b).

## 4.7 Recovery rate estimation

Spline fits are used to provide smoothed curves for estimating maximum growth rates during recovery (Figs. 4.1(c), 4.2(a)). Spline estimates for $N(t)$, the cell abundances recorded by the microscope as a function of time, were computed as detailed in Section 3.7, with spline estimates performed on raw (not rolling average) single-cell counts. Cubic splines returned an estimate of the number of single cells per image which we denote $\hat{N}(t)$. We performed these spline fits after each washout event for all of the data shown in Fig. 4.2. To estimate the instantaneous growth rate we computed $\frac{dln\hat{N}(t)}{dt}$.

### 4.7.1 Measurements of system dynamics by optical density

Our devices also record transmitted light intensity in real time during each experiment using a photodiode and infrared LED pair. These data permit us to measure abundance dynamics indirectly, and to corroborate our findings of frequency and amplitude dependent dynamics (Fig. 4.18(a)). However, our optical density measurement is complicated by a varying optical density value for 'zero' abundance - the expected measurement if the vial were filled with water. This value fluctuates over the course of each experiment, most likely due both to changes in the density of biofilm on the vial walls and physical disturbance of the vial itself, which can rotate somewhat freely and is periodically lifted from the system during operation to check for system failure.

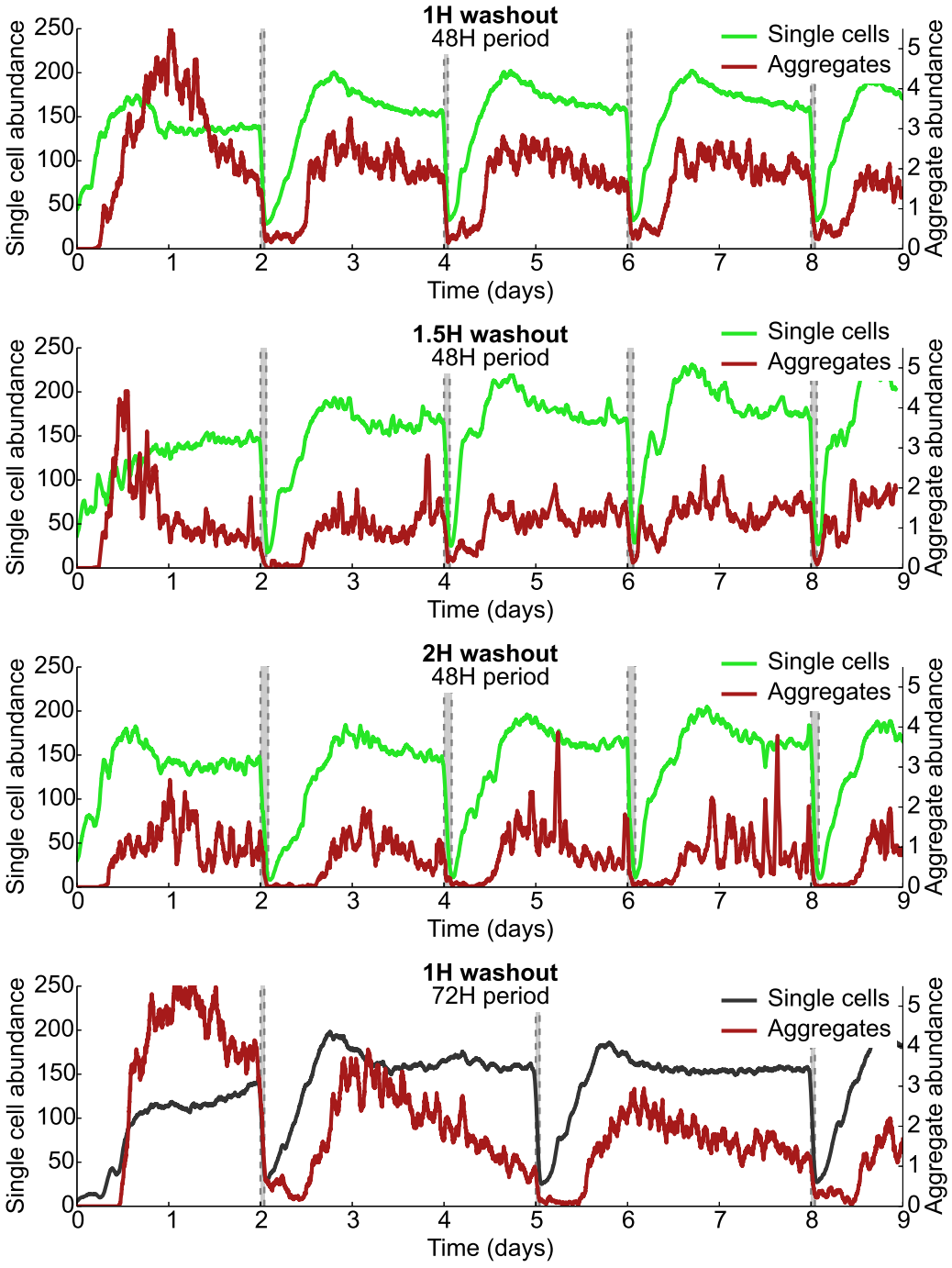


Figure 4.17: Example per-image abundance dynamics of single-cell populations and aggregates under washout conditions not shown in Fig. 4.2. Single-cell and aggregate abundances are each smoothed with a 1 hour rolling average. Shaded regions indicate washout events.

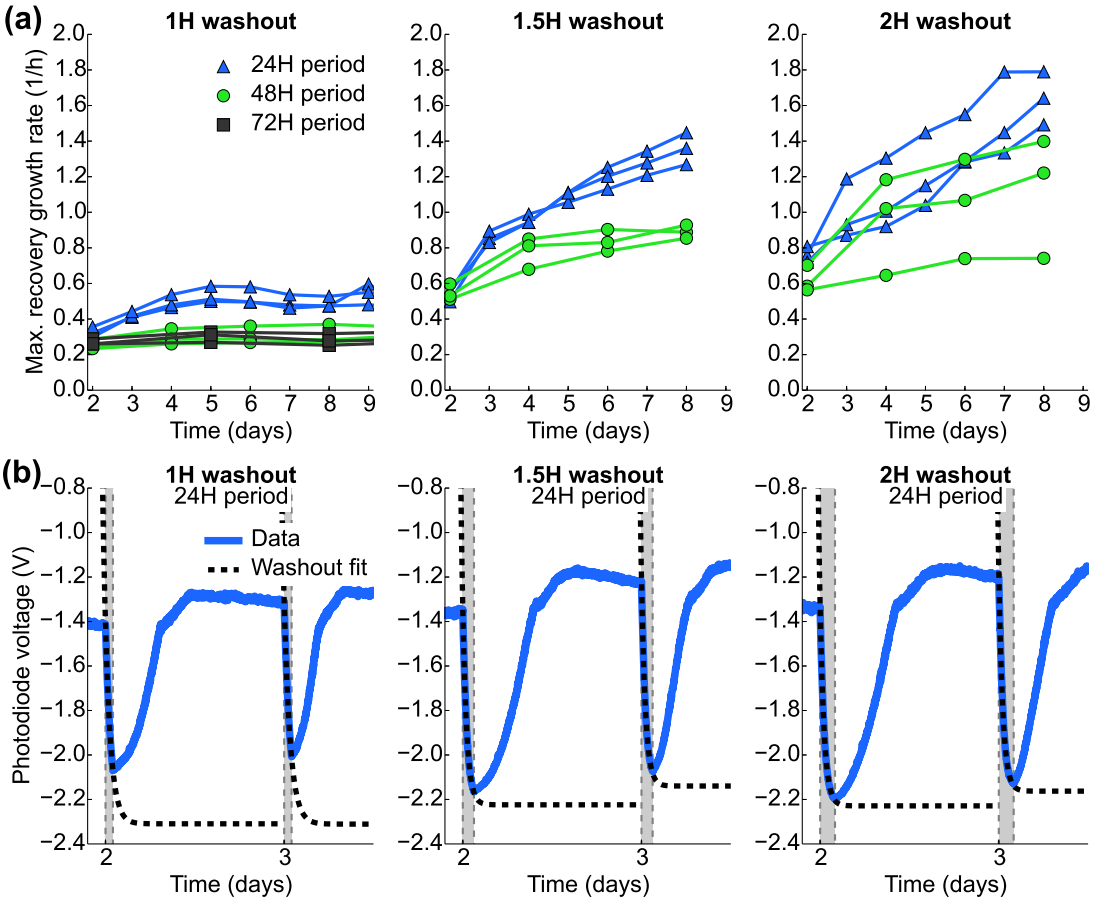


Figure 4.18: Frequency and amplitude dependent dynamics measured by optical density. (a) Estimated maximum population growth rates during recovery for 1 h, 1.5 h and 2 h washouts, based on optical density measurements alone, at different washout frequencies. (b) Representative optical density time series for one replicate each from experiments with 1 h, 1.5 h, and 2 h washouts, all with a 24 h washout period. Dashed lines indicate the decaying exponential fits to washout data used to determine the system 'zero' for optical density during the following recovery. Shaded regions indicate washout events.

### 4.7.2 Analysis of optical density data

To calculate the optical density recovery data shown in Fig. 4.18(a), we add an additional step to the spline-based recovery rate estimation mentioned above. Because growth during washout events is in general slow following hours of steady-state growth, we assume an exponential decay of the population during the brief washout period, and therefore use a decaying exponential fit during each washout to estimate the 'zero' abundance value the photodiode reading is asymptotically approaching (Fig. 4.18(b)). This 'zero' abundance value is subtracted from the recovery immediately following the washout event to generate an adjusted time series that can be used to estimate recovery growth rates. Splines are then applied to these adjusted time series to estimate maximum rates of recovery via the same analysis used for single-cell counts.

This measurement corroborates the central claim of this chapter with a measurement which is completely independent of our image acquisition and analysis, as shown by the similarity between Fig. 4.18(a) and Fig. 4.2(a).

## 4.8 Additional experiments

### 4.8.1 Repeated batch culture experiments

In addition to our standard continuous-culture experiments, consisting of standard chemostat operation interrupted by periods of rapid washout, we also performed several 'batch'-style experiments. These repeated batch experiments, which can roughly be interpreted as simulating repeated inoculations from one batch culture to another, are identical to our standard experiments, but with a basal dilution rate of zero outside of the scheduled washout event periods. As aggregates do not typically form in our systems in when $D = 0$ (batch culture conditions) (Fig. 4.12(a)), we view these experiments as a test on the role of cell aggregates and the history-dependent recovery dynamics we observe when $D > 0$ between washout events. However, cells are too dim in these conditions for our image segmentation to reliably detect during all stages of growth. Because we found optical density recovery dynamics (Fig. 4.18(a)) displayed the same trends as single-cell abundance recovery dynamics (Fig. 4.2(a)),

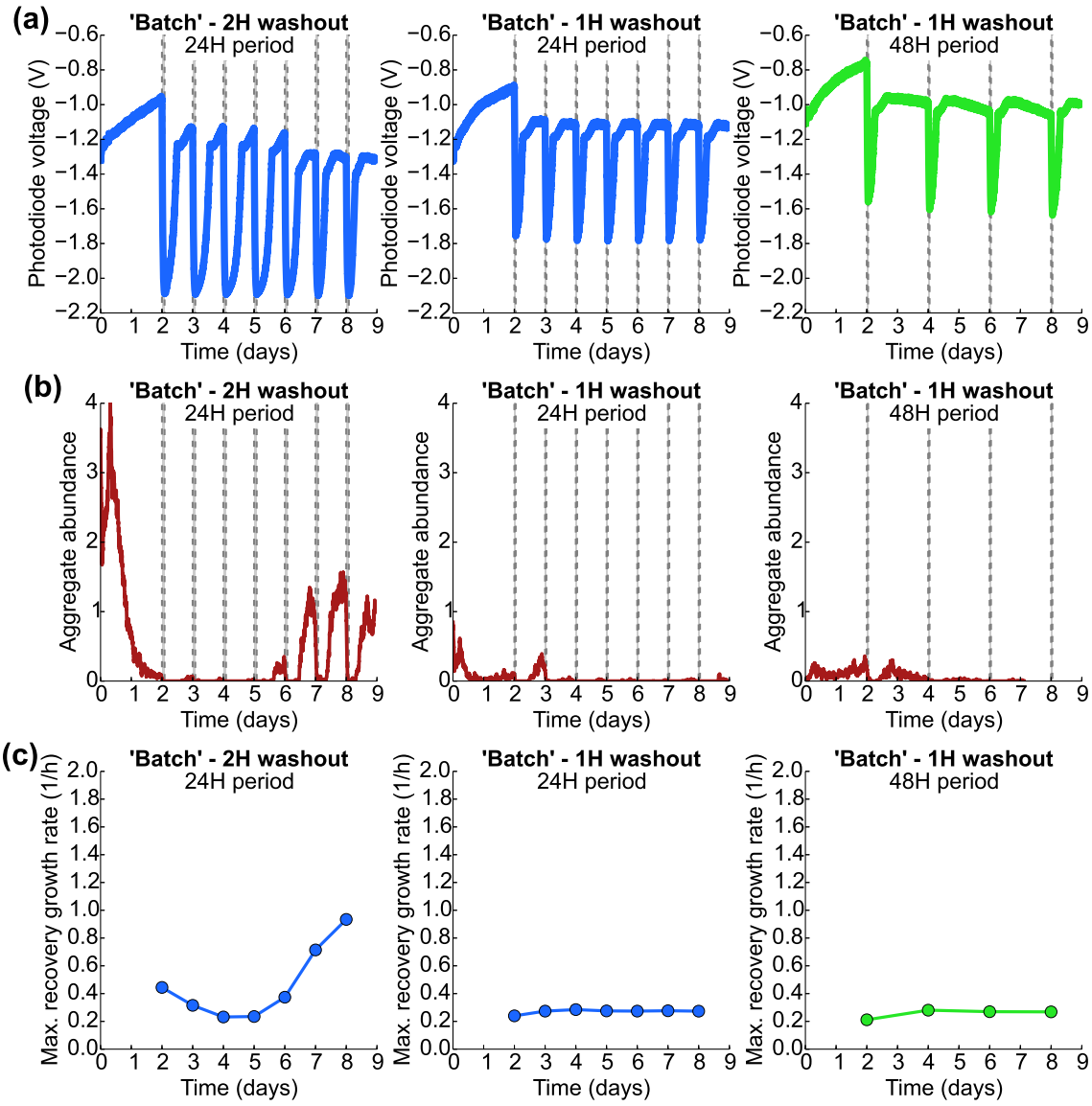


Figure 4.19: Batch-style experiment show no frequency or amplitude dependence. (a) Optical density time series of 'batch'-style experiments ($D = 0$ between washout events). Shaded regions indicate washout events. (b) Cell aggregate abundance (per image) time series, as determined by standard image processing. As the camera exposure time was increased substantially for these experiments, the brightness threshold for detection of aggregates was slightly increased to filter out uncommonly bright single cells. We note the eventual appearance of aggregates in the 2 h washout condition, correlated with a size increase in detected aggregates as shown in Fig. 4.15. (c) Maximum optical density recovery rates based on data shown in (a). We note that these do not show the strong frequency-dependence and amplitude-dependence of our continuous-culture experiments, shown in Fig. 4.18(a) and Fig. 4.2(a), but that the recovery rate does eventually begin to increase in the 2 h washout condition, correlating in time with the appearance of aggregates.

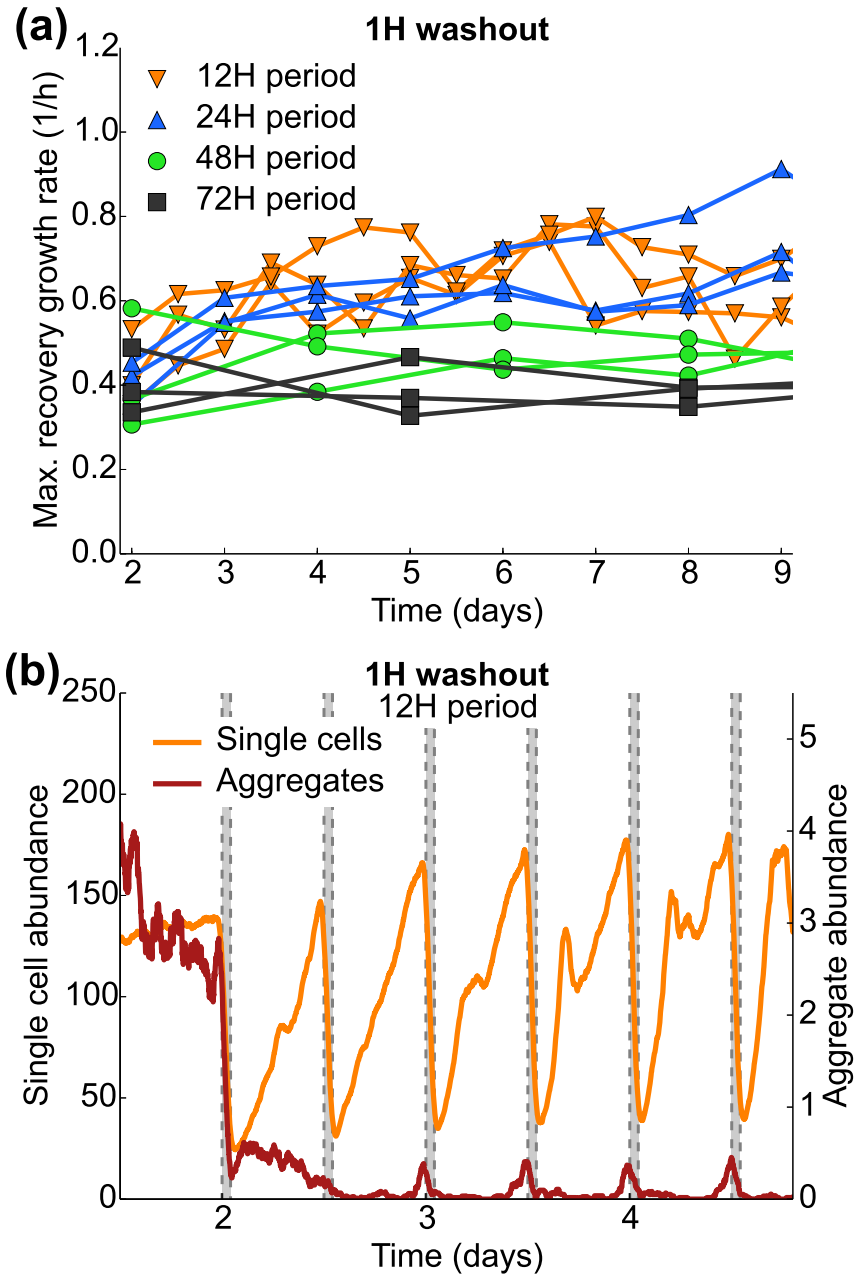


Figure 4.20: High frequency abundance dynamics. (a) Maximum recovery rates from 1 h washout experiments, with high-frequency 12 h washout period included. (b) Single-cell and aggregate abundance (per image) time series, each smoothed with a 1 hour rolling average, from a 12 h washout period replicate. Shaded regions indicate washout events. Fast recovery washouts are maintained despite the low abundance of detected cell aggregates.

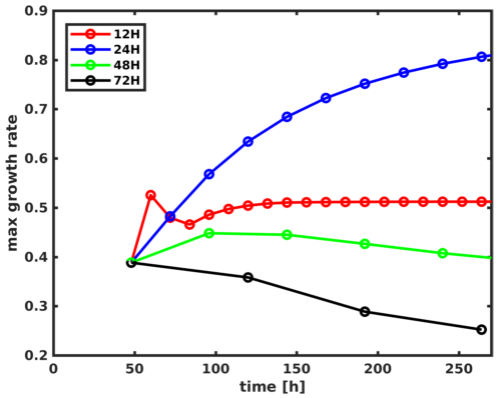


Figure 4.21: Simulations do not capture maximum per-hour recovery rate dynamics expected from experiment (Fig. 4.20(a)) in high frequency 12 h washout schedule with 1 h washout duration.

we instead relied on optical density measurements to analyze these 'batch'-style experiments, which were carried out with 1 h and 2 h washout events at a 24 h washout period, and 1 h washout events at a 48 h washout period (Fig. 4.19(a)).

Unlike our standard continuous-culture experiments, the expected frequency- and amplitude-dependence in recovery dynamics are essentially absent, except in the 2 h washout condition (Fig. 4.19(c)), where a fast recovery appears to correlate to the eventual arrival of aggregates in the system after 5 days (Fig. 4.19(b)).

These results show that the presence of aggregates are a necessary condition for the observation of fast recovery rates. They also suggest that higher average dilution rates drive aggregation, since we observe the formation of aggregates at late times in the 2 h condition. Our model does not include this phenomenon.

### 4.8.2 High frequency washout events: 12 hour data

We also carried out a high-frequency washout continuous-culture experiment, with 1 h washouts every 12 h, chosen to be roughly the same amount of time it takes one of our continuous-culture populations to fully recover following a 1 h washout event. Our preliminary work (detailed in Chapter 3) indicates the appearance of aggregates following a washout event is correlated to the onset of slow growth occurring when the population of single-cells nears maximum density. Consistent with this, the aggregate abundances we detect fail to reach appreciable levels during the 9-day experimental window, as the appearance of cell aggregates is also immediately cut off by the next washout event (Fig. 4.20(b)). However, the systems still maintain a fast growth rate

during recovery (Fig. 4.20(a)), possibly due to sources of aggregation not visible to our microscope, e.g. wall growth. Our model cannot capture the dynamics at these very high frequencies (Fig. 4.21) for the simple reason that there is insufficient time for aggregates to form when washout events occur at high frequency. One possible reason for this discrepancy is that high frequency washout events may drive more substantial and rapid adhesion to the culture vessel itself (e.g., decrease $\rho$). At present we cannot quantitatively test this conjecture.

## 4.9 Model parameters

Here we recapitulate the model presented in the Section. 4.3 and provide motivation for the parameter values chosen in the numerical simulation presented in Fig. 4.3. The model is as follows:

$$\dot{N} = \mu(S)N - DN - \alpha_1(1 - f(S))N + \alpha_2 \frac{Q}{1+Q} f(S) A Y_{NA}, \tag{4.4}$$

$$\dot{A} = \alpha_1(1 - f(S))\frac{N}{Y_{NA}} - \alpha_2 \frac{Q}{1+Q} f(S)A - \rho D A, \tag{4.5}$$

$$\dot{S} = (S_r - S)D - \frac{\mu(S)}{y} N, \tag{4.6}$$

$$\dot{Q} = \begin{cases} aQ & S \geq S_c \\ -bQ & S < S_c \end{cases}, \tag{4.7}$$

$$f(S) = \begin{cases} 0 & S \leq S_{th} \\ \frac{S - S_{th}}{S_r - S_{th}} & S > S_{th} \end{cases}, \tag{4.8}$$

$$\mu(S) = \frac{\mu_m S}{K + S}. \tag{4.9}$$

$N$ is the abundance of planktonic cells, $A$ is the abundance of aggregated or adherent cells, $S$ is the substrate (glucose) concentration, $Y_{NA}$ is the number of cells per aggregate, $D$ is the dilution rate of the continuous-culture device, $\alpha_1$ is the rate of

formation of aggregates, $\alpha_2$ is the rate of dispersal of aggregates, $0 \leq \rho \leq 1$ simulates the role of adherent populations not washed out of the system, $y$ is the yield of bacteria on the substrate, $S_c$ and $S_{th}$ are parameters.

Note that in the simulation we set $y = 1$ and $S_r = 100$ without loss of generality. Experimentally, $S_r = 2.2$mM which yields a maximum cell density of approximately $5 \times 10^8$ cells/mL. We perform simulations over a range of $S_c$, $S_{th}$, and $\rho$ to test the sensitivity of our conclusions to these unknown parameters. The results are shown in Fig. 4.22. We find little sensitivity of our conclusions to changes in $S_c$ and $S_{th}$, but stronger sensitivity to the value of $\rho$.

Below we present the value of each parameter used in the simulation and a justification.

| Parameter | value | justification |
|---|---|---|
| $\mu_m$ | $0.3\,\mathrm{h}^{-1}$ | [19] |
| $K$ | 45 $\mu$M | [78] |
| $\alpha_1$ | $0.04\,\mathrm{h}^{-1}$ | inferred |
| $\alpha_2$ | $0.125\,\mathrm{h}^{-1}$ | see below |
| $Y_{NA}$ | 100 cells/aggregate | Fig. 4.14 |
| $a$ | $0.07\,\mathrm{h}^{-1}$ | see below |
| $b$ | $0.0275\,\mathrm{h}^{-1}$ | see below |
| $S_c$ | 0.22 mM | see below |
| $S_{th}$ | 1.5 mM | see below |
| $\rho$ | 0.1 | see below |

Table 4.1: Model parameter values

### 4.9.1 Bounds on $\alpha_1$ and $\alpha_2$

Direct measurement of aggregation/adherence and dispersal rates in our experiment is not possible. However, from general considerations we can place some bounds on what these rates ($\alpha_1$ and $\alpha_2$) should be. We begin by considering the limit where $S << S_{th}$. In this case, growth is slow and the equations describing $N$ and $A$ become

$$\dot{N} = \mu(S)N - (D + \alpha_1)N, \tag{4.10}$$

$$\dot{A} = \alpha_1 \frac{N}{Y_{NA}} - \rho DA. \tag{4.11}$$

Aggregation then acts to increase the effective planktonic dilution rate by $\alpha_1$. This reduces the steady state abundance of planktonic cells in the system ($N^*$), which is a declining function of $D$. Experimentally we observe a decline in the planktonic abundances as the aggregation process proceeds after a washout event (for example, see Fig. 4.1 and Fig. 4.12(b)). This decline is on the order of 20 % of the maximum planktonic abundances we observe. By simulating the $S << S_{th}$ limit we find that for $D = 0.08\,\mathrm{h}^{-1}$, $\alpha_1 = 0.04\,\mathrm{h}^{-1}$ results in a roughly 20 % decline in steady state planktonic abundances due to aggregation. We therefore fix $\alpha_1$ to $0.04\,\mathrm{h}^{-1}$ for all simulations presented here (Table 4.1).

Next we consider the limit where $f(S) = 1$ ($S \to S_r$) and ask how big an effect on the planktonic population growth rate the dispersal of $A$ can have. To estimate this we consider the case where $f(S) = 1$ and $Q >> 1$:

$$\dot{N} = \mu_m N - DN + \alpha_2 A Y_{NA}. \tag{4.12}$$

Rewriting the density of the $A$ population by $N_A = AY_{NA}$ and dividing through by $N$ we get

$$\frac{dln(N)}{dt} = \mu_m - D + \alpha_2 \frac{N_A}{N}. \tag{4.13}$$

For dispersal to have an appreciable impact on the planktonic population growth rate we require that $\mu(S) \approx \alpha_2 \frac{N_A}{N}$ which requires either an $A$ population which dramatically exceeds $N$ or a dispersal rate that is of the same order as $\mu_m$. From our measurement of the aggregate densities (Fig. 4.1) and the average size of aggregates (Fig. 4.14) we assume that the ratio $\frac{N_A}{N}$ is of order 1 to 10, which suggests that the dispersal rate must be of order $\mu_m$. We choose a value for this parameter which satisfies this constraint (Table 4.1).

### 4.9.2 Values of $S_c$ and $S_{th}$

$S_{th}$ sets the substrate level controlling dispersal. We note that neither of these parameters are known. However, we do know that aggregation appears to increase substantially as growth rates slow during a recovery (see Chapter 3). Further, given the amplitude dependence of the recovery rate we observe in experiment (Fig. 4.2(a)) the dispersal rate of $A$ should be sensitive to the substrate concentration in the neigh-

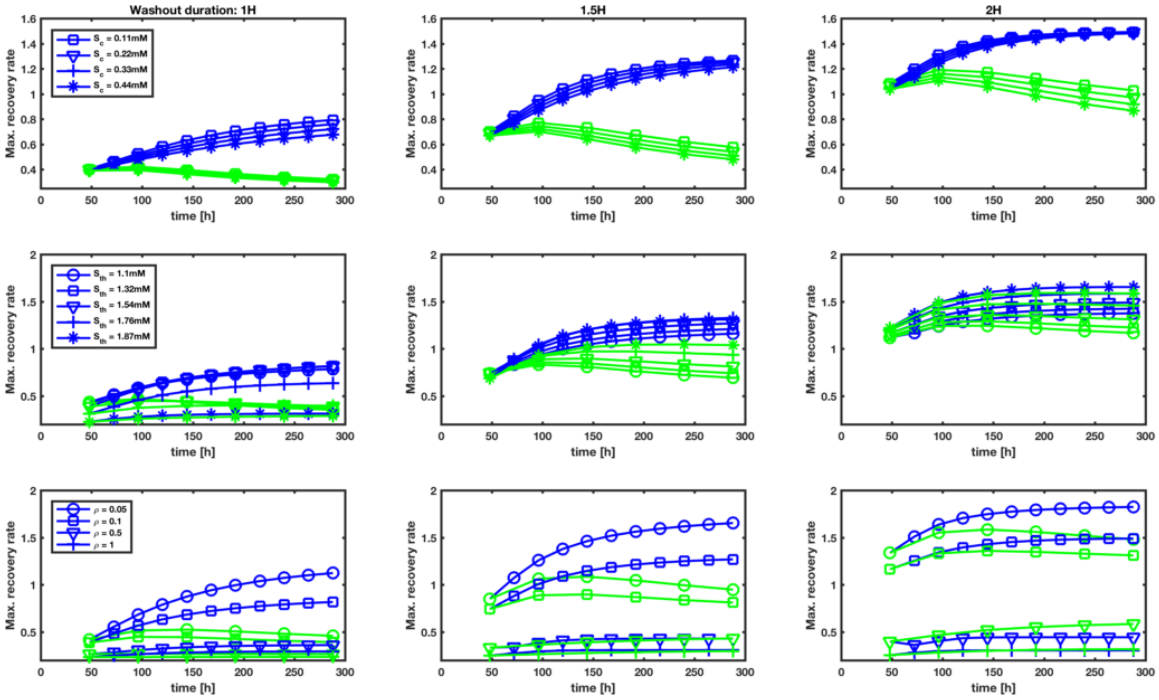


Figure 4.22: Simulations of maximum per-hour recovery rates with variable parameters. Three parameters were systematically varied to determine the sensitivity of our conclusions to chosen parameter values. Each row corresponds to a different parameter: $S_c$ (top), $S_{th}$ (middle), $\rho$ (bottom). Each column corresponds to a washout event duration: 1 h (left), 1.5 h (middle) and 2 h (right). Within each panel blue traces correspond to a 24 h washout event schedule and green traces to a 48 h washout event schedule. Different symbols ($\square$, $\circ$ etc) correspond to different parameter values as denoted by the legends in the left column. Green and blue traces with the same symbols are simulations with the same value of the relevant parameter. For example, in the lower right panel the blue and green traces plotted with $\circ$ are 24 and 48 hour conditions with $\rho = 0.05$. The values of $S_{th}$ and $S_c$ should be considered relative to the reservoir glucose concentration, $S_r = 2.2$mM.

borhood of 2 mM. Within these constraints we find that a wide range of values for $S_{th}$ recapitulate our observations (Fig. 4.22).

Although the processes regulating biofilm maturation in *E. coli* are complex, gene expression levels suggests the presence of effectively starved, stationary-phase cells may be necessary for biofilm maturation, and that penetration of nutrients into biofilms may directly hinder their formation [40]. For our model, we extend this idea to external substrate levels - assuming the amount of substrate penetrating into biofilms rises in proportion to rising external substrate levels - through the parameter $S_c$, which explicitly sets the substrate level at which the maturation process proceeds (or degrades). $S_c$ is chosen to be substantially smaller than $S_{th}$ as it is assumed to directly relate to nutrient limitation, but a similarly wide range of values of $S_c$ reproduce our results (Fig. 4.22).

### 4.9.3 Value of $\rho$

In our model $\rho$ is a proxy for the reduced effect of dilution on aggregated cells due to adherence to the wall; $\rho = 1$ would indicate a fully free-floating aggregate population, and $\rho = 0$ would indicate an entirely adherent population. While we cannot measure $\rho$ directly, simulations over a range of values show that our results are sensitive to the choice of $\rho$ (Fig. 4.22). We note that at $\rho \approx 1$ we fail to observe the strong amplitude and frequency dependence in simulation that we observed in experiment, and therefore conclude that some adherent populations are necessary to account for our results. Past this, $\rho$ was chosen as a free parameter; however, as discussed above, our model cannot capture the experimental dynamics at very high frequencies (Fig. 4.21), which may imply a decrease in $\rho$ (increased adherence) in rapid washout conditions.

### 4.9.4 Dynamics of $Q$: rates $a$ and $b$

In our model of abundance dynamics the frequency dependence results from a declining rate of dispersal for the $A$ population as the duration of famine increases. This process - biofilm maturation - is described by the variable $Q$. When $Q$ is small (long periods of $S < S_c$) the dispersal rate is proportional to $Q$. Conversely, when

$Q$ is large, dispersal is independent of this internal variable. The dynamics of $Q$ are assumed to be autocatalytic (see Section 4.3) with rates $a$ and $b$. In the 72 hour condition long periods of famine result in small $Q$ and limited dispersal and therefore slow recoveries. In the 24 hour condition we observe fast recoveries driven by $A$ dispersal because $Q >> 1$. Therefore, we set the values of $a$ and $b$ in our simulation (Table 4.1) such that $Q < 1$ for a 72 hour cycle and $Q >> 1$ for a 24 hour cycle.

# Chapter 5

# Multi-species dynamics in complex phototroph-heterotroph communities

This chapter contains descriptions of unpublished work by Kaumudi Prabhakara, Harry Mickalide, Jason Merritt and Seppe Kuehn.

This work was partially supported by the Center for the Physics of Living Cells, the National Science Foundation Physics Frontier Center (PHY 0822613 and PHY 1430124), the Carl R. Woese Institute for Genomic Biology, and the Department of Physics at the University of Illinois at Urbana-Champaign.

Contributions and Acknowledgements: Seppe Kuehn and Kaumudi Prabhakara conceived the direction for future research. Kaumudi Prabhakara contributed material and writing to the introduction of this chapter. Harry Mickalide developed the schematics and designs for the continuous-culture device adaptations made to enable growth of photosynthetic organisms. Kaumudi Prabhakara and Jason Merritt designed and tested the microscope adaptations for two-color imaging with multiple species. Jason Merritt developed the new software and performed machining and construction of system adaptations. *YFP*-fluorescent bacterial strain referenced was received from Suckjoon Jun's lab. Algal strain referenced was received from the UTEX Culture Collection of Algae.

## 5.1 Introduction

Recently, it has been found that communities in similar environments differ in their taxonomic composition, but are similar in their metagenome – the genetic material of the entire community [82,83]. Analysis of these ecosystems revealed that although the populations and identities of the species and families present in similar environments were diverse, the functional capabilities of the communities - such as fermentation, nitrogen fixation, and respiration - were conserved in similar environments, although

information about these capabilities could only be inferred from genetics. We seek to understand whether taxonomically diverse but metagenomically similar communities also exhibit similar dynamics. While the relation between the structure and dynamics of communities has been the subject of many studies, these have resulted in contradictory conclusions; while some works [84, 85] find that the structure and dynamics of the communities in similar environments are variable despite the net function being stable, Tyson *et al.* [86] find both deterministic dynamics and similar function in different communities. The continuous-culture devices built in our lab are ideal tools to investigate these questions in ecosystems.

In the future, our lab will isolate samples from natural environments such as soils or lakes. Some isolated species may be naturally fluorescent, which could be used to trace their dynamics in our systems. We can also insert additional fluorescent species such as naturally fluorescent algae and *YFP*-labelled *E. coli* and trace their dynamics along with that of the isolates. After perturbing the communities via the automatic addition of chemicals, such as excess nitrogen or phosphorous, the response of the system can be efficiently studied by imaging the tracer species' response. Samples collected from our systems can be further analyzed to check for chemical consumption, providing a quantitative measure of the community function - ability to degrade nitrogen and phosphorous - that does not rely on genomic data. In this chapter, we briefly present preliminary work in adapting our systems to carry out experiments measuring simultaneous population dynamics in *YFP*-labeled *E. coli* - which is significantly brighter than our *dTomato*-labeled strain - and chlorophyll-containing algae, which can be measured with the same excitation source.

## 5.2 Strains

Before we begin collecting natural isolates, our prototype systems will be propagating organisms other than the *dTomato*-labeled strains of *E. coli* used in the experiments presented in previous chapters. By using cells expressing *YFP* rather than *dTomato*, it is possible to simultaneously excite fluorescent protein in bacterial cells and chlorophyll in photosynthetic organisms with cyan light, obviating the need for complex designs with moving parts. For testing our systems, we use the *YFP*-labeled SJ102

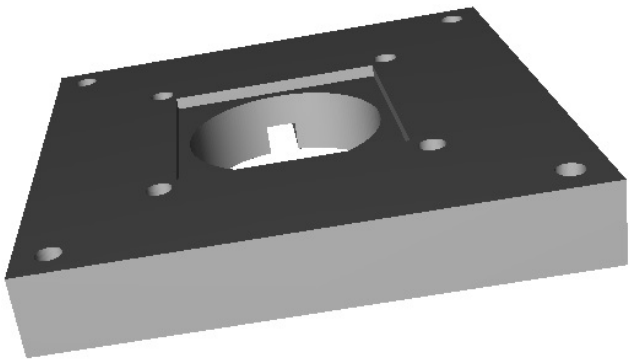

Figure 5.1: 3D-printed part for system photosynthetic growth adaptation. Circular cutout and channel in bottom provide room for LED and path for wiring. Square cutout provides room for thin transparent acrylic strip to support culture vial. Inner holes match hole spacing on bottom of machined holder part (see Fig. A.1); outer holes are not used in this design.

strain of *E. coli*, received from SuckJoon Jun's lab, and the UTEX2244 strain of the alga *Chlamydomonas reinhardtii*, received from the UTEX Culture Collection of Algae.

## 5.3 Adaptations for photosynthetic growth

A design already used in our lab for growing photosynthetic organisms in culture propagation devices similar to the continuous-culture devices described in this work was adapted for integration into our systems. Key features of this design include the addition of a CREEXPE2-740-1 white LED for growth of fluorescent organisms (mounting modification described in Appendix A), driven by a newly added on-wire 350 mA BuckPuck LED driver with a connection to the LabJack for dimming (Fig. B.3). A custom 3D-printed part (produced by Illinois MakerLab), shown in Fig. 5.1 and visible mounted in Fig. 2.2, is used to allow the the LED to illuminate the culture vial from below, with space for insertion of a slip of transparent acrylic to support the vial and a CL211 ND 0.9 neutral density filter sheet to further dim the high-power LED output.

## 5.4 Adaptations for two-color imaging

After exciting our *YFP*-labeled *E. coli* and algae with the same cyan light source, we can image them separately using two cameras behind different optics allowing for

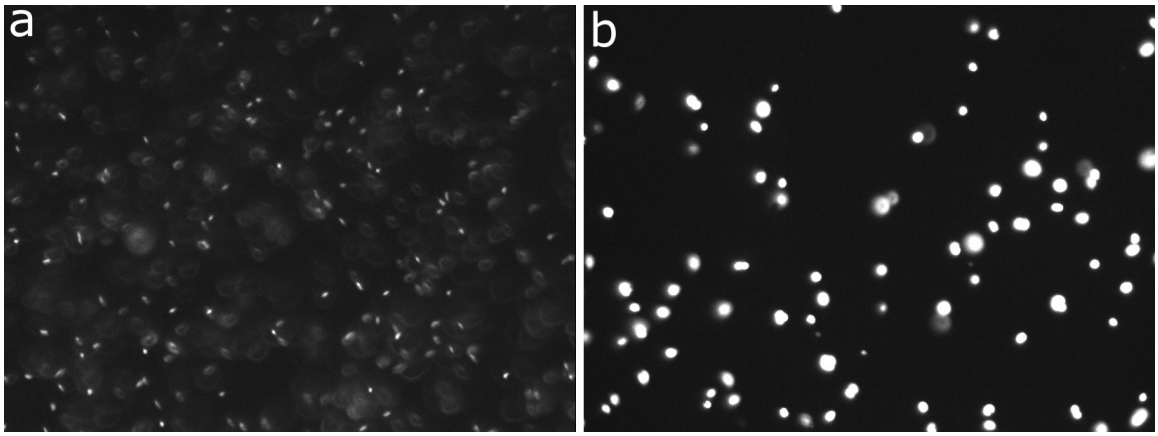


Figure 5.2: Images from two-color microscope design. a) Reflected 20x images of *YFP*-labeled *E. coli* using a 2 mm dichroic mirror, showing only minor aberration. b) Transmitted 10x images of chlorophyll signal of *C. reinhardtii*.

different image magnifications. To this end, we replaced our fluorescence illumination source with a ThorLabs M505D2 505 nm high-power LED, and our *dTomato* filter set with a Chroma 39003 YFP filter set, and added a AC254-100-A-ML achromatic doublet for imaging algae at a lower (10x) magnification.

By splitting the sample emission spectrum just above the range of the *YFP* emission filter (AT540/30m), it is possible to split most of the significantly brighter chlorophyll emission spectrum away from the *YFP* camera. The T565lpxr dichroic mirrors from our *dTomato* filter sets split at 565 nm and were therefore added to the microscope using a custom part to mount two ThorLabs CM1-DCH filter cubes in sequence (Fig. A.4(e)). However, dramatic aberration in the reflected (*YFP*-fluorescent *E. coli*) image resulting from curvature in the dichroic surface necessitates the replacement of existing mirrors with Chroma 2 mm UF ('ultra-flat') variants meeting a <0.5 wavelengths/inch curvature specification (see Fig. 5.2 for representative images, and Fig. 5.3 for microscope design).

Finally, camera control code was updated with the optional capacity to reference cameras by serial number, enabling image capture from multiple cameras attached to the same computer for multi-color fluorescent imaging in the same experiment. To ensure system ease of use for future experimenters, a Python (TkInter) GUI was added to allow direct component control of continuous-culture devices, and all FlyCapture SDK C camera control code was ported to the PyCapture (Python) SDK.

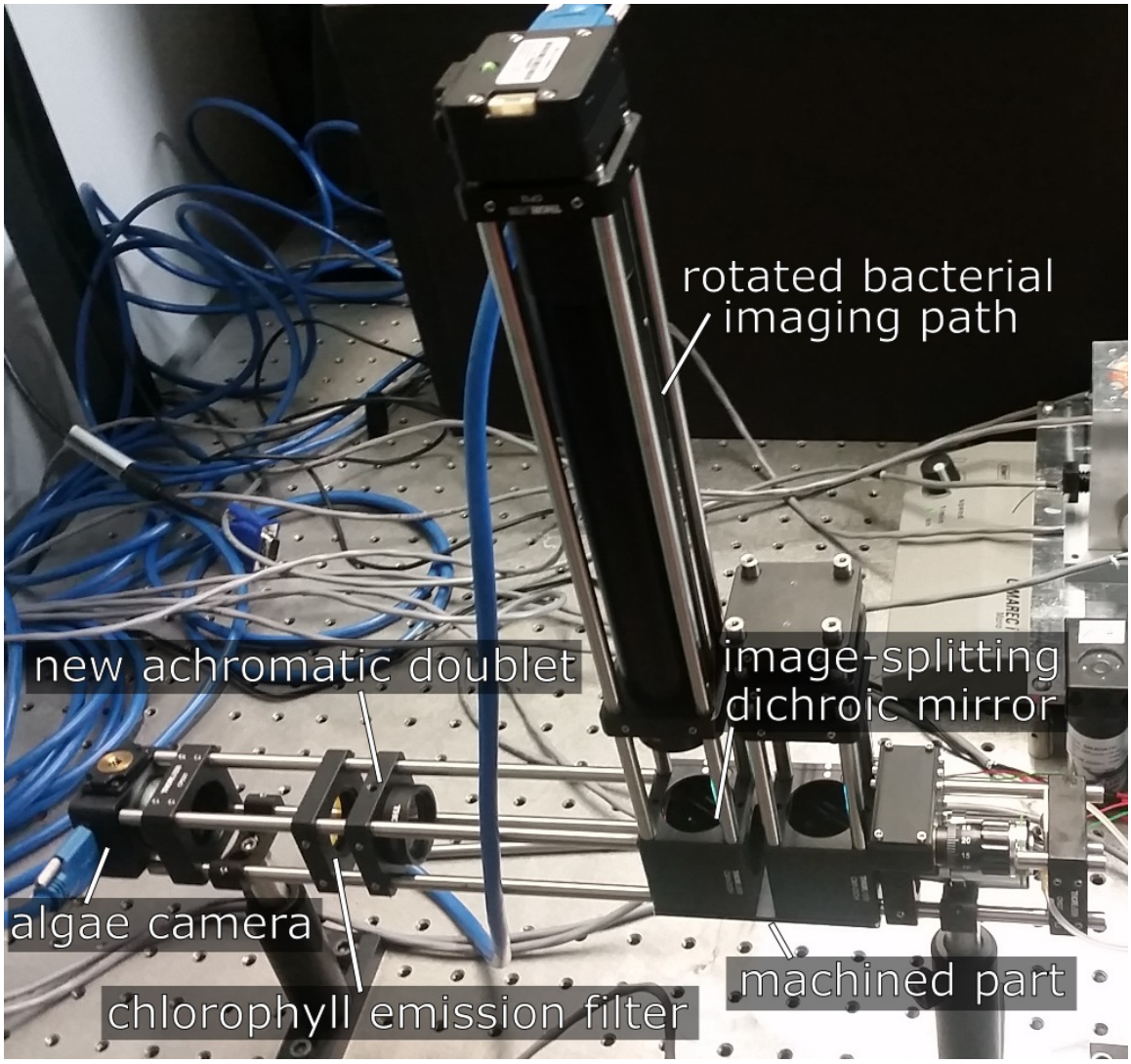


Figure 5.3: Chlorophyll/*YFP* epifluorescence microscope (functional prototype). Excitation/objective design is identical to that of original microscope design, Fig. 2.4. Bacterial (*YFP*) imaging path is identical to that of original design, rotated vertically to receive *YFP* signal, split from chlorophyll signal by ultra-flat dichroic mirror connected to setup with custom machined part (Fig. A.4(e)). Achromatic doublet with shorter focal length ($f = 100\,\mathrm{mm}$) permits lower magnification at detector of added algae camera. Bacterial imaging path design physically blocks excitation light from reaching algae camera.

# Appendix A

# Machined parts

Because the continuous-culture device and microscope used in our experiments were custom-designed, many structural elements had to be custom-machined for our needs. The bulk of the structural elements constituting the continuous-culture device itself were manufactured by the CNC machining service eMachineShop. These include:

- The custom "holder" part (Fig. A.1), which houses the culture vial and basic measurement equipment, including the temperature probe used for temperature control and the IR LED and photodiode used for density measurements. The holder itself is also the direct object of the temperature control used in the experiments, with thermal contact to the culture vial increased by adding strips of copper tape to the vial hole (visible in Fig. 2.2) for a tighter fit.
- The custom "connector" part (Fig. A.2), which is used to mount the peltier heat pump used for temperature control to the holder, and which connects to a large heat sink at the other end. The length of this part is set by the distance from the holder to fans mounted to the optical table, which requires projecting some distance past the edge of the stir plates.
- The custom "plate" part (Fig. A.3), which provides support for the otherwise unbalanced holder-connector system and mounts directly to the optical table. After centering the stir plate, screwing the plate down on top also helps clamp the stir plate into plate. Later modifications to this part (described in the figure caption and highlighted in Fig. 2.2(c)) allow for direct mounting of the inflow and outflow peristaltic pumps, and easier measurement of the stir plate rpm with a Hall probe.

We machined a number of additional parts ourselves, primarily for the microscope. These include the parts shown in Fig. A.4 (see caption for detailed descriptions) and

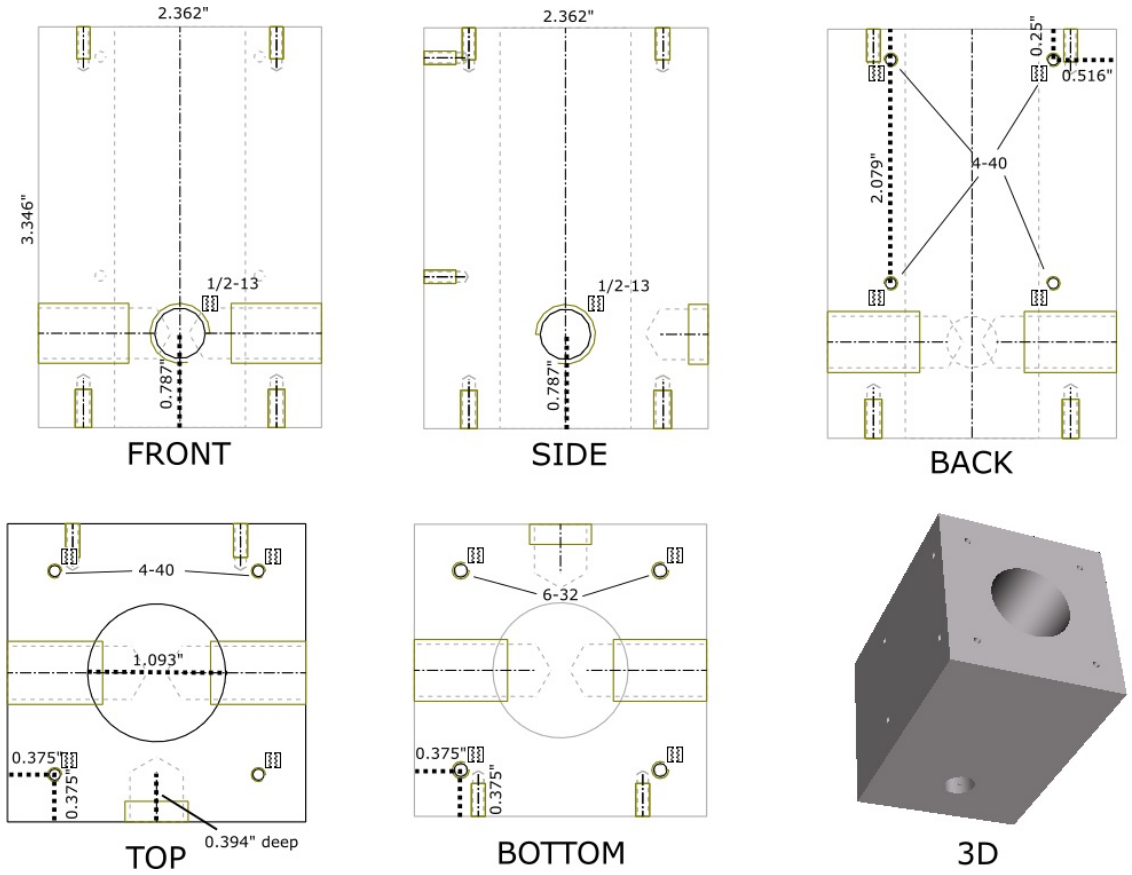


Figure A.1: Custom "holder" machined part manufactured by eMachineShop. Holder houses vial houses Chemglass CG-4902-08 40 mL vial containing bacterial culture, with 1/2"-13 mounting holes for measurement components in the sides. Temperature control is achieved using a Peltier heat pump mounted on the back and a temperature probe mounted in a 1/2"-13 nylon screw in thermal contact with the holder mounted in front. Side 1/2"-13 mounting holes allow attachment of a matched IR LED-photodiode pair for optical density measurement. 6/32 holes at bottom mount to machined "plate" part.

the thin capillary insert whose design is outlined in Appendix D. Most of these parts are for mounting equipment, but the T-slotted aluminum extrusions stabilize imaging by damping vibrations in the flexible tubes leading to the microscope.

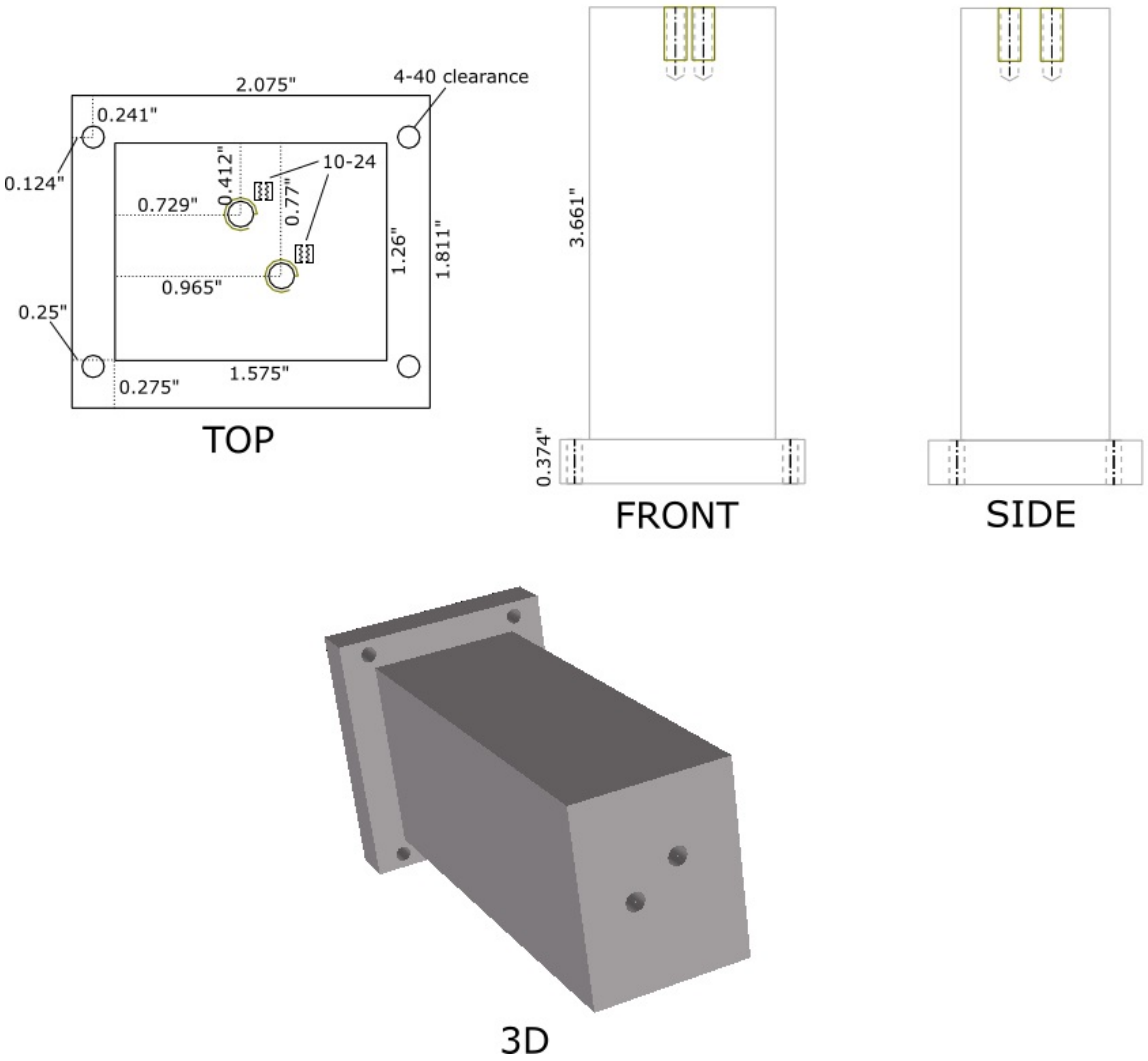


Figure A.2: Custom "connector" machined part manufactured by eMachineShop. Connector functions as a heat conductor from one side of a Peltier heat pump to a Wakefield-Vette 401A heat sink affixed via 10-24 holes at the end. Through-holes at base allow connecting to the machined "holder" part housing the vial, with the Peltier element held between the two by compression.

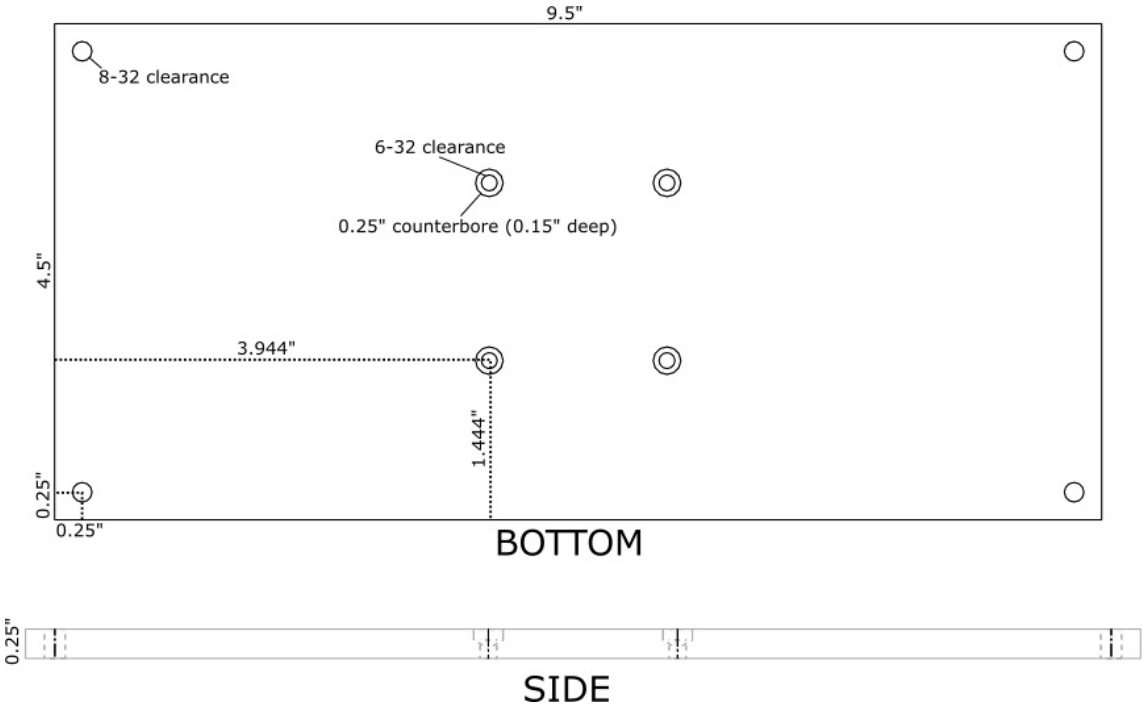


Figure A.3: Custom "plate" machined part manufactured by eMachineShop. Counterbored holes at center allow mounting custom "holder" part at top, and 8-32 clearance holes on sides allow mounting plate over stir plate onto optical table using optical posts. Later modifications to this part include increasing counterbore depth to the 0.15" measurement shown in the figure, and additional features circled in Fig. 2.2, which include mounting holes for peristaltic pumps matching the pattern shown in Fig. A.4(c), and a 3/16" trench milled through to the center to enable fast measurement of stir plate rpm with a Hall probe. Two tapped 6-32 holes were additionally added at center 13/16" apart to allow mounting a white LED for photosynthetic organisms.

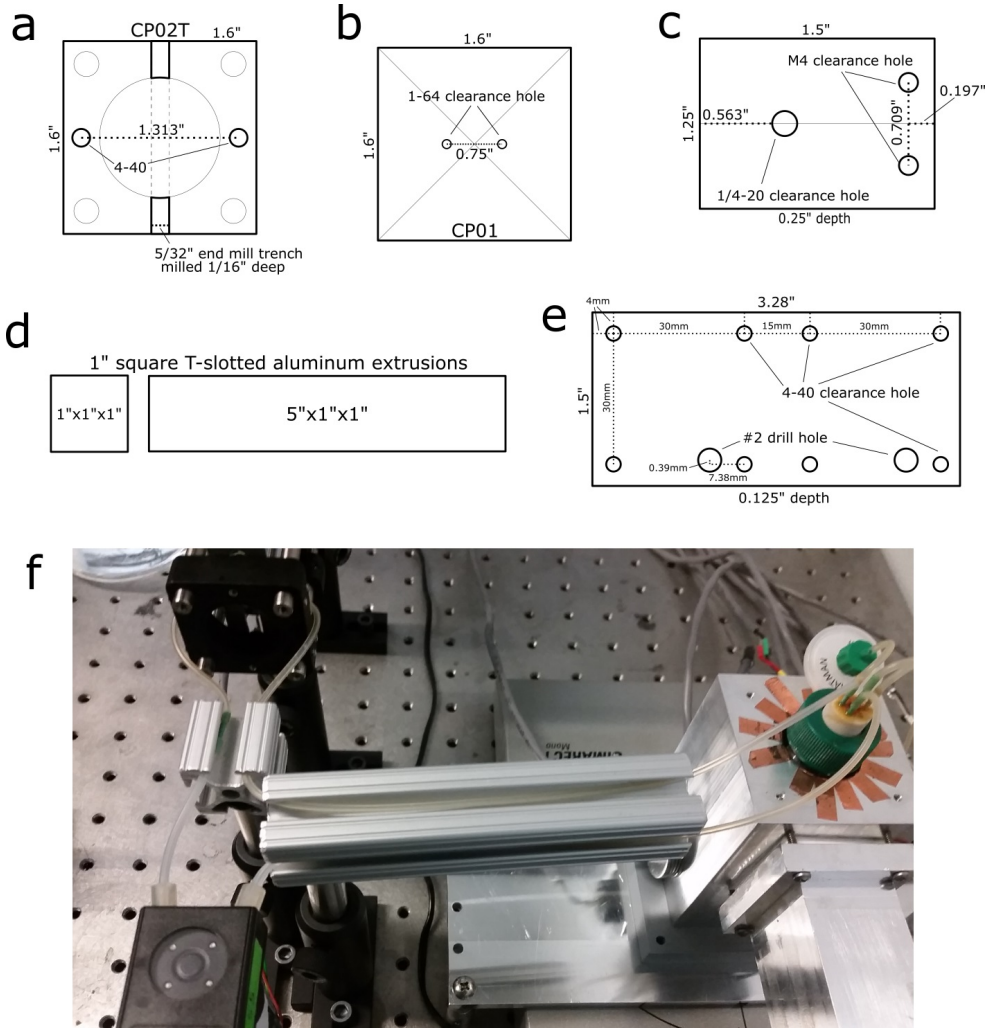


Figure A.4: Various custom structural machined parts. (a) Capillary block. Two tapped 4-40 holes added to a Thorlabs CP02T cage plate allow mounting capillary inserts in front of the microscope objective. Milled trench for tubing attached to capillary insert allows capillary insert to lay fully flat. (b) LED mount. Two 1-64 clearance holes drilled into a Thorlabs CP01 plate allow mounting the high-power microscope color LED. (c) Optical table pump mount. 1/4"-20 through hole allows mount to attach to inverted optical post, and M4 clearance holes enable mounting of Watson-Marlow 400F/A pump. Suspending this pump above the optical table is necessary to reduce dead volume of microscope lines. (d) T-slotted aluminum extrusions function as support for microscope lines, as shown in (f). Without this part, vibrations in unsupported microscope lines prevent reliable imaging. Due to the complex geometry of T-slotted extrusions, cut edges must be deburred carefully to prevent cutting into microscope lines. (e) Dichroic cube connector. Not part of original microscope design; added later to allow directly mounting two separate Thorlabs CM1-DCH dichroic cage cubes for simultaneous imaging of algae and bacteria. #2 drill holes are structurally unimportant, but allow dichroic mirrors to be unscrewed and replaced without disassembling microscope. (f) Image showing proper use of T-slotted aluminum extrusions from (d), leading from continuous-culture device to pump mounted on machined part shown in (c) and capillary block shown in (a).

# Appendix B

# Electronics box schematics

A custom electronics box was designed to house the electronics used to control each continuous-culture device. The electronics box itself was cut out of 4.5 mm acrylic (Fig. B.1) by the laser cutting company Ponoko, with mounting tabs tapped by hand and epoxied in place to allow the sides to be connected with screws. The electronics box holds five main components:

- A LabJack U3-LV DAQ device for control of other circuitry and internal parts, with attached CB15 terminal board for additional outputs.
- A custom circuit board (Fig. B.6) which contains the circuits used for temperature control, OD measurement, and the microscope LED driver. The motor driver controlling the Peltier heat pump also mounts directly to this part.
- A low-cost 8 channel relay module, controlled by the LabJack, for switching pumps and LEDs on and off. Our modules were Kootek-branded, but use a design common to many other companies (e.g. SainSmart, JBtek). Although the electronics box design includes optional mounts for an additional module, only one relay module was used in the experiments.
- A high-current VDRS-100-12 12 V power supply which powers most of the basic parts used in the continuous-culture device, including the peltier heat pump, fans, pumps, and high-power LEDs. To work properly with the LabJack-driven motor driver, the power supply output must be manually grounded by connecting ground to the low voltage output.
- A low-current LS25-12 12 V power supply totally isolated from all other components to provide a stable voltage to the IR LED used for optical density measurement. This power supply output is also manually grounded in our design.

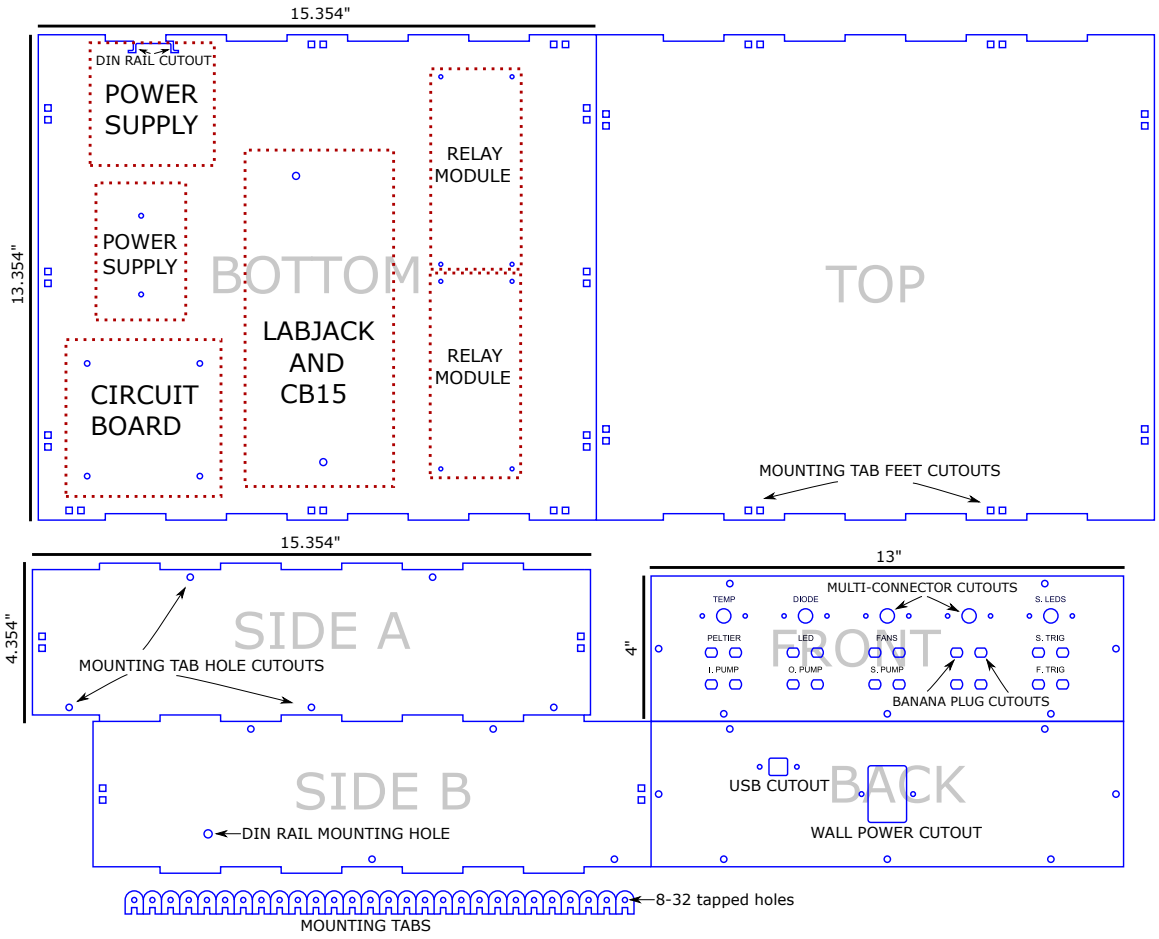


Figure B.1: Electronics box laser cutting schematics. Basic layout of components inside electronics box presented at top left, missing an on-wire LED driver added to the system as a modification for enabling growth of photosynthetic organisms. The top right relay module mounting holes are optional and unused in the electronics boxes used in experiment. Laser cut parts produced by Ponoko in 4.5 mm acrylic sheets.

Because the internals of the electronics box are fairly complex (Fig. 2.3), we provide separate schematics for the primary internal circuits: pump control (Fig. B.3), high-power LED control (Fig. B.3), optical density measurement (Fig. B.4), and temperature control (Fig. B.5). We also present a diagram of the custom circuit board used in the experiment (Fig. B.6).

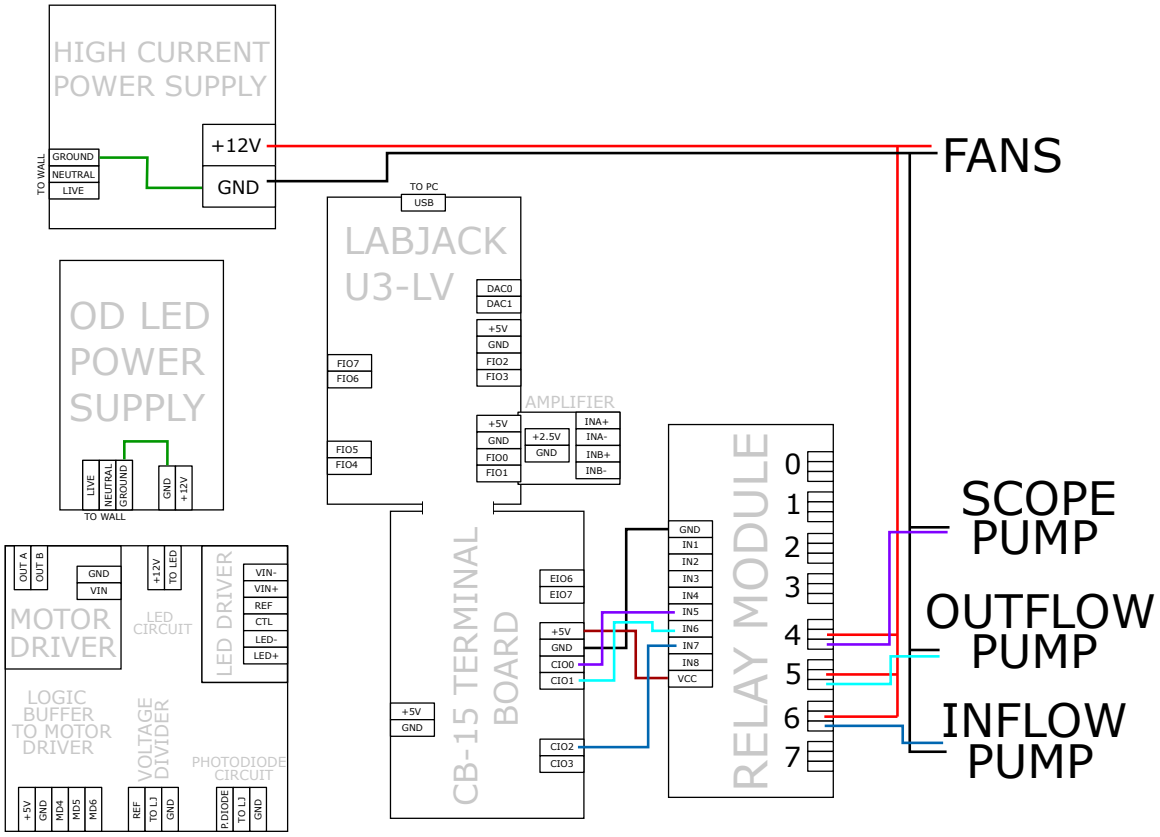


Figure B.2: Schematic for fan and pump wiring inside electronics box. Fans are always on, pumps are switched via LabJack signals to relay modules.

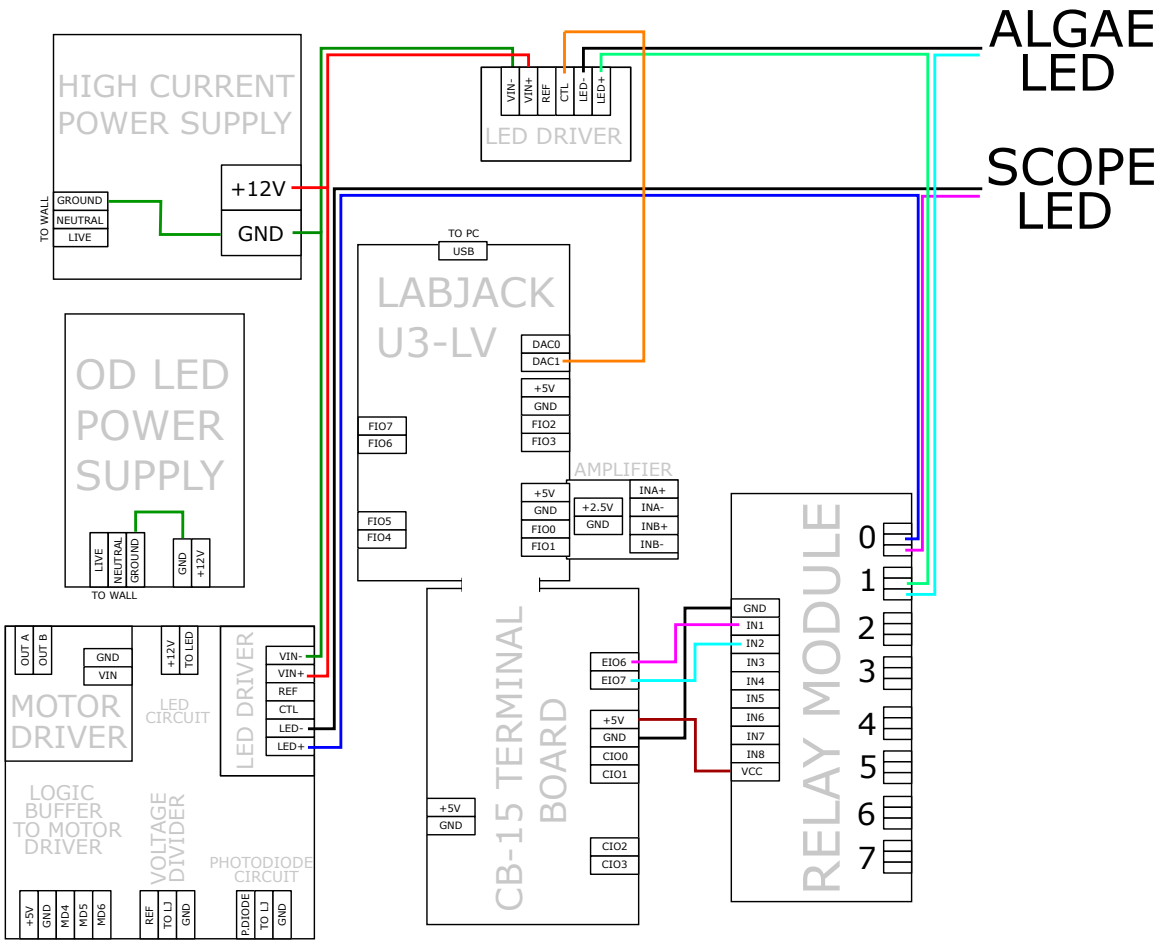


Figure B.3: Schematic for LED power inside electronics box. Both LEDs are controlled by relay module. Microscope LED operates at constant brightness through LED driver mounted on circuit board; "algae LED" for photosynthetic organisms uses on-wire LED driver with dimming controlled by analog output from LabJack.

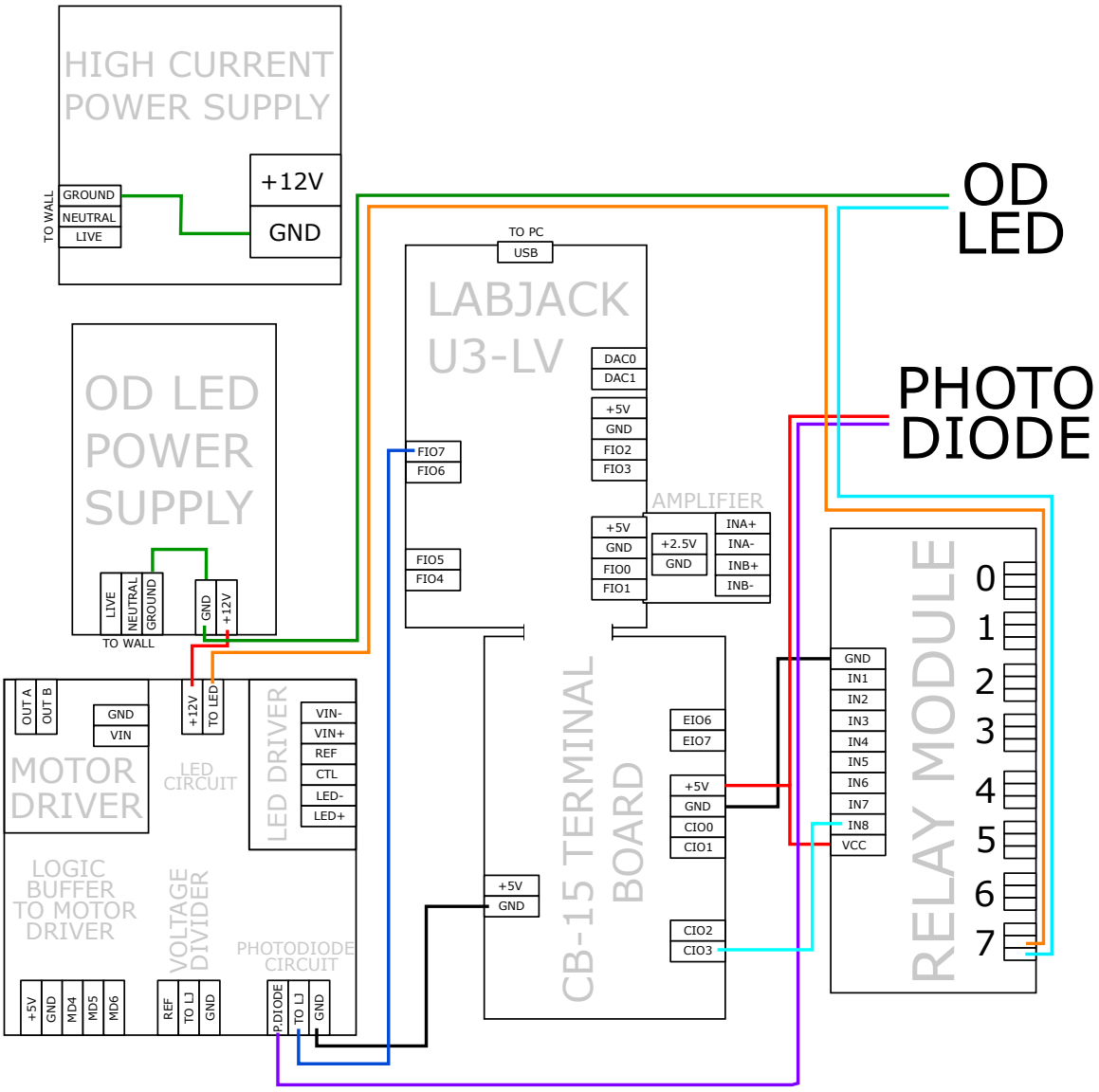


Figure B.4: Schematic for optical density measurement wiring inside electronics box. IR LED is switched through relay module, and a simple circuit allows measuring output voltage from photodiode.

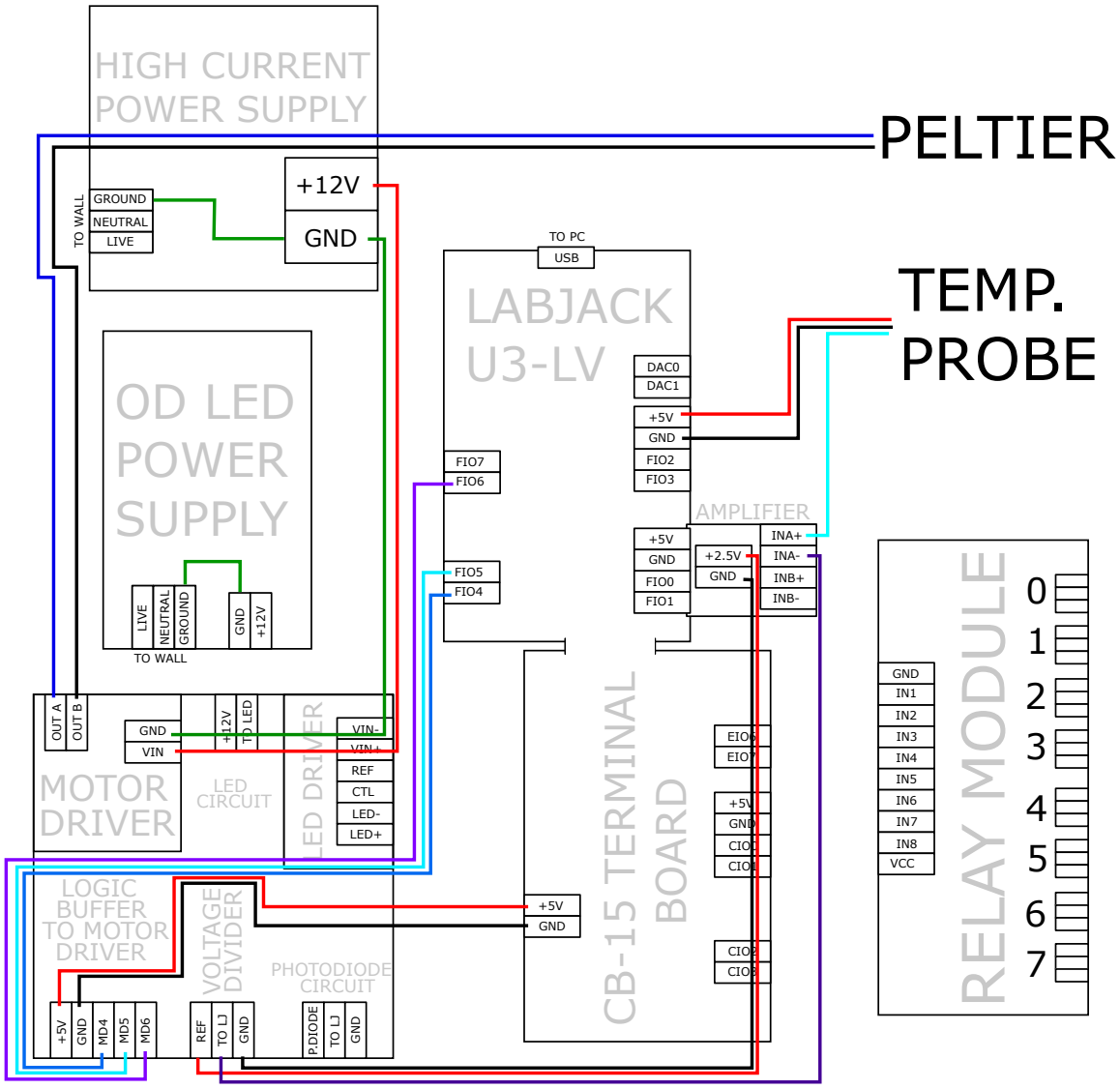


Figure B.5: Schematic for temperature control wiring inside electronics box. LabJack signals to motor driver control direction of Peltier heat pump, with PWM signal controlling Peltier duty cycle. The difference between the output of a voltage divider and the reading from a temperature probe is amplified to obtain an accurate temperature measurement from the continuous-culture device.

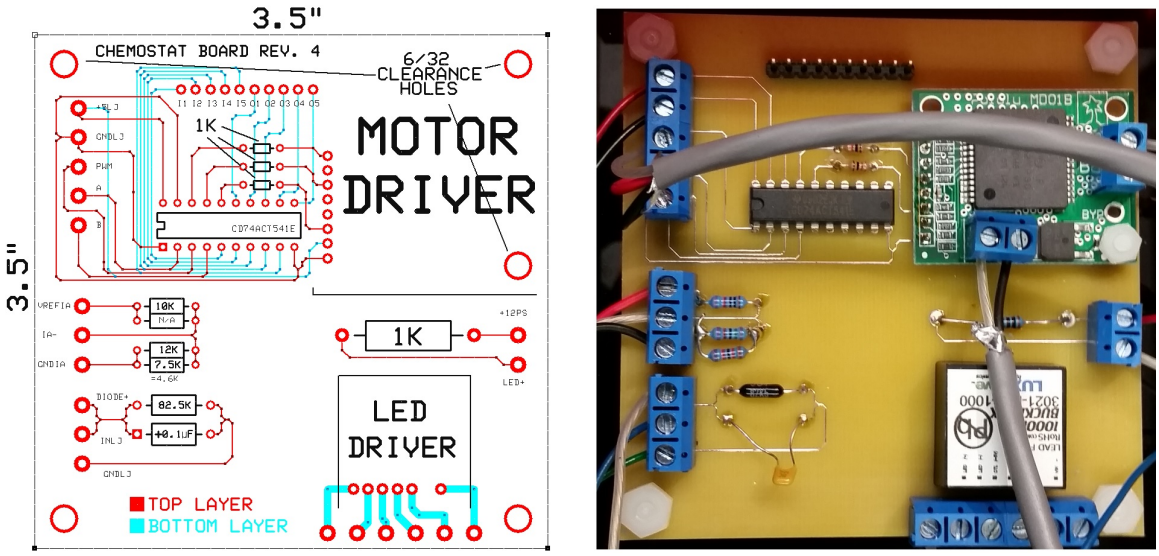


Figure B.6: Continuous-culture device custom circuit board. Left: final revision of circuit board schematic, with minor changes including improved hole arrangement and added holes for mounting voltage divider resistors in parallel. Right: actual circuit board appearance as used in experiments.

# Appendix C

# Custom caps and tube elements

## C.1 3D-printed vial caps

To connect the various tubing needed to flow liquid in and out of the culture vial in a continuous-culture experiment, we designed a custom vial cap (Fig. C.1(a)) and had it 3D-printed in autoclavable Nylon 12 PA by Stratasys. The cap itself is designed to support up to 7 rigid ∼1.6 mm OD PEEK tubing connections, and the cap holes have a nominal 2 mm inner diameter, but imprecision in the 3D-printing process often results in holes too small for the PEEK tubing to be inserted. In these cases, a thin metal implement (such as a needle or pin) is used to scrape material off the inner surface of the holes until the PEEK tubing can fit. PEEK tubing is affixed with to the cap with OD2002 epoxy from Epoxy Technology, with 730 epoxy used to cover unused holes. Both epoxies are cured at 121 °C to avoid exposing the 3D-printed cap to higher temperatures than it would experience in the autoclave. As shown in Fig. C.1(c), the PEEK tubing sticking out the top of the cap can be directly connected to 1 mm ID silicone tubing, and as shown in Fig. C.1(d), the 3D-printed cap can be mounted on our culture vials with a Chemglass CG-4910-04 open top screw cap. The five PEEK tubing connections used in our experiments (shown in Fig. C.1(b)) are cut with a specialized PEEK tubing cutter producing flat edges, and have lengths, inner diameters and functions as follows:

- A 0.04" ID PEEK tubing section extending ∼3/8" into the vial, providing an tube hooked up to an autoclavable 0.1 µm filter for gas exchange.
- A 0.04" ID PEEK tubing section extending ∼$2\frac{1}{8}$"into the vial for liquid outflow to the waste bottle. This section sets the liquid level in the water; as the only way for liquid to leave the vial, the culture level cannot drop below it, and as

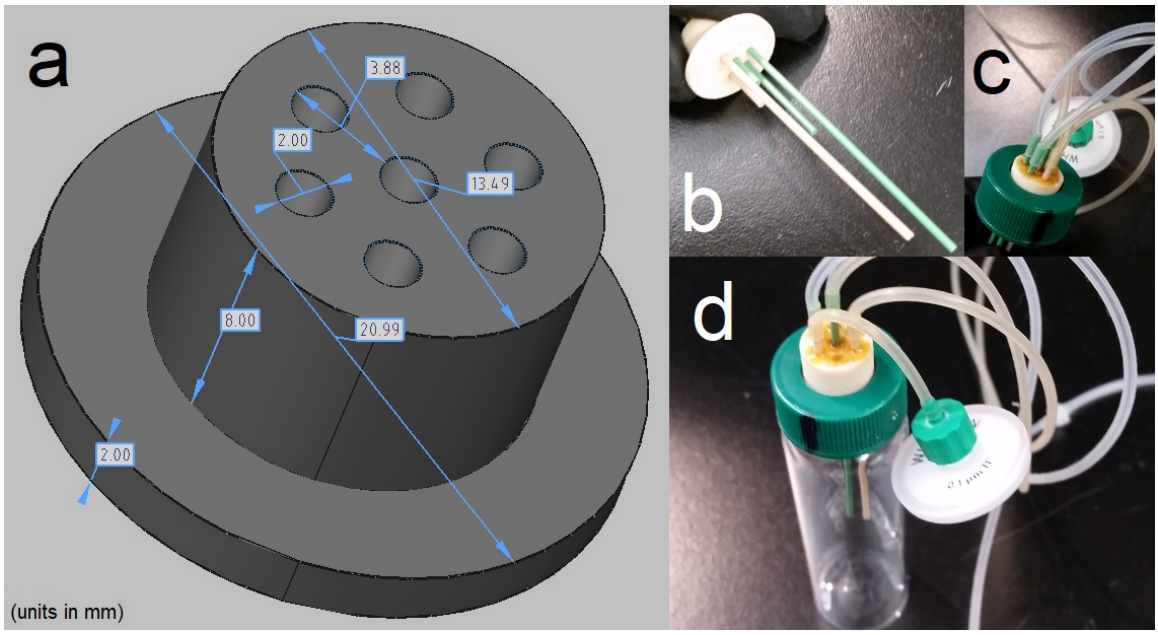


Figure C.1: Autoclavable 3D-printed Nylon 12 PA vial cap. (a) Vial cap specifications sent to Stratasys. (b) Vial cap supports 1.6 mm (1/16") OD PEEK tubing descending into culture vial. (c) Flexible 1 mm ID silicone tubing attaches directly to PEEK tubing on cap top. (d) Chemglass CG-4910-04 open top screw caps mount 3D printed cap to 40 mL CG-4902-08 culture vials.

long as the output pump removes any excess liquid, the culture level cannot rise above it. As a result, the actual length for this segment is set by using a scale to add 20 mL of water to a vial and lowering the PEEK tubing until it touches the surface of the liquid.

- A 0.03" ID PEEK tubing section extending ∼1/4" into the vial, for liquid inflow of fresh growth medium. To reduce the risk of contamination, this connection terminates highest and is located at the center (farthest from the culture vial walls).

- A 0.03" ID peek tubing section extending $\sim 2\frac{5}{16}$" into the vial. This tube always terminates below the liquid level, and is used to sample culture into the microscope line.

- A 0.03" ID peek tubing section extending ∼7/8" into the vial, for returning culture to the system as it exits the microscope line.

## C.2 Media bottle caps

Special custom media bottle caps are used to connect tubes to and from the 1 L media bottles used for media input to and waste output from our culture vials. The input cap uses rigid PEEK tubing of length matched to the 1 L media bottles and connected with OD2002 and 730 epoxy from Epoxy Technology, and the output cap directly affixes flexible 1 mm silicone tubing with Red Devil heat-resistant silicone to optionally allow for culture sampling with a syringe. Culture sampling was performed rarely in our experiments, typically only for plating experiments, and was carried out by manually activating the output pump (by briefly connecting the output pumps plugs to the always-on fan outputs) to nearly empty the output line (placing the freshest culture nearest to the output cap), affixing a syringe to a female Luer attached to the silicone tubing, opening the output pump to release the pressure holding liquid in the line in place, and extending the syringe to draw in the culture sample before closing the output pump and returning the fan and pump wiring to normal.

## C.3 Tube elements

The Watson-Marlow 400F/A pumps used in our experiments operate at a fixed rate of 26 rpm, but are capable of achieving different flow rates via the use of different "tube elements." Tube elements are small sections of tubing, held in place via attached luers or stoppers, inserted into the pump and acted on by the peristaltic rollers. Because tube elements are under a great deal of stress and the part of our continous-culture systems most prone to failure they must be replaced on a semi-regular basis to avoid leaks and experiment failure. Unfortunately, manufacturer-produced tube elements are expensive and very few kinds of tubing are suitable for use as tube elements in 400F/A pumps. To avoid the expense of repeatedly purchasing individual tube elements, we developed a protocol to make new tube elements ourselves (Fig. C.3).

- Inflow tube elements determine the overall dilution rate of the system. 5 cm sections of Universal Biologicals 070497-10-F tubing (1.02 mm ID, 2.72 mm OD) are suitable for use as tube elements in our systems, with resulting flow rates of approximately $0.81\,\mathrm{mL\,min^{-1}}$ under constant pump operation. To lock the

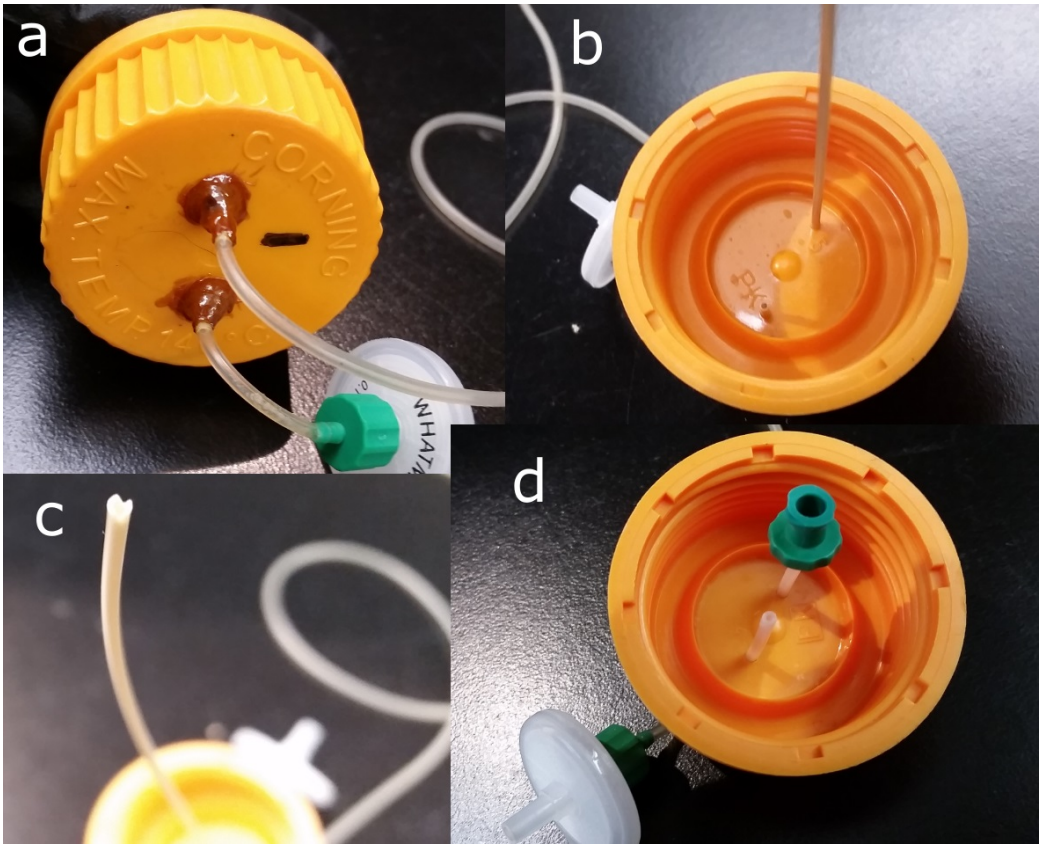


Figure C.2: Custom media bottle caps. (a) Custom media bottle caps consist of two tubes passing through machined holes, one for liquid flow and one attached to a 0.1 µm autoclavable filter for gas exchange. Input/media caps consist of rigid PEEK tubing attached to silicone tubes with Epoxy Technology OD2002 epoxy, secured to the cap itself with 730 epoxy. Output/waste caps use Red Devil heat-resistant silicone. (b) Input bottle caps use rigid internal PEEK tubing to reach the bottom of 1 L media bottles. (c) Internal PEEK tubing is notched at the end to prevent suction onto bottle surfaces. (d) Output bottle caps have short flexible internal silicone tubing, which can be attached to a female Luer to allow sterile sampling mid-experiment with a syringe.

tube elements in place we use the original plastic components supplied to us by Watson-Marlow, which connect to 2 mm ID tubing, requiring the use of a Luer lock to connect back to our standard silicone tubing. This is in part to make different tube elements distinguishable immediately on visual inspection, but the Watson-Marlow component uses an identical barb style to our standard Nordson Medical 500 series 1/16" tubing luer barbs (as used on our outflow tube elements) and can be easily replaced.

- Outflow tube elements were originally identical to inflow tube elements, with volume control handled by having output pumps run longer every minute and by having systematically faster pumps handling output. However, we found that after several years, under extreme circumstances, outflow pumps could rarely pass less volume per minute than inflow pumps, so we switched to larger ID tubing for our tube elements. 5 cm sections of Universal Biologicals 070497-13-F tubing (1.42 mm ID, 3.12 mm ID) - the largest tubing appropriate for use in our pumps - theoretically pass nearly twice the volume per minute as our inflow tube elements, and can be attached to our systems using Luer locks with Nordson Medical 500 series 1/16" tubing barbs.

- Microscope tube elements must run substantially slower than other tube elements to avoid over-pressurizing the tube leading to the capillary, which is small enough to strongly resist the flow of liquid. An additional concern is that Luer locks are not suitable for attaching to microscope tube elements, as they add substantial dead volume to the line - resulting in slower measurements. As a result, we can use Universal Biologicals 070497-08-F tubing (0.76 mm ID, 2.46 mm OD) - which theoretically passes roughly half the volume per minute as our inflow tube elements - combined with low-dead-volume Nordson Medical AA-6005 "straight-through" fittings for tube elements. However, the longer Nordson Medical classic series barbs on these fittings slightly interfere with pump operation, requiring these tube elements be cut to a slightly longer 5.5 cm.

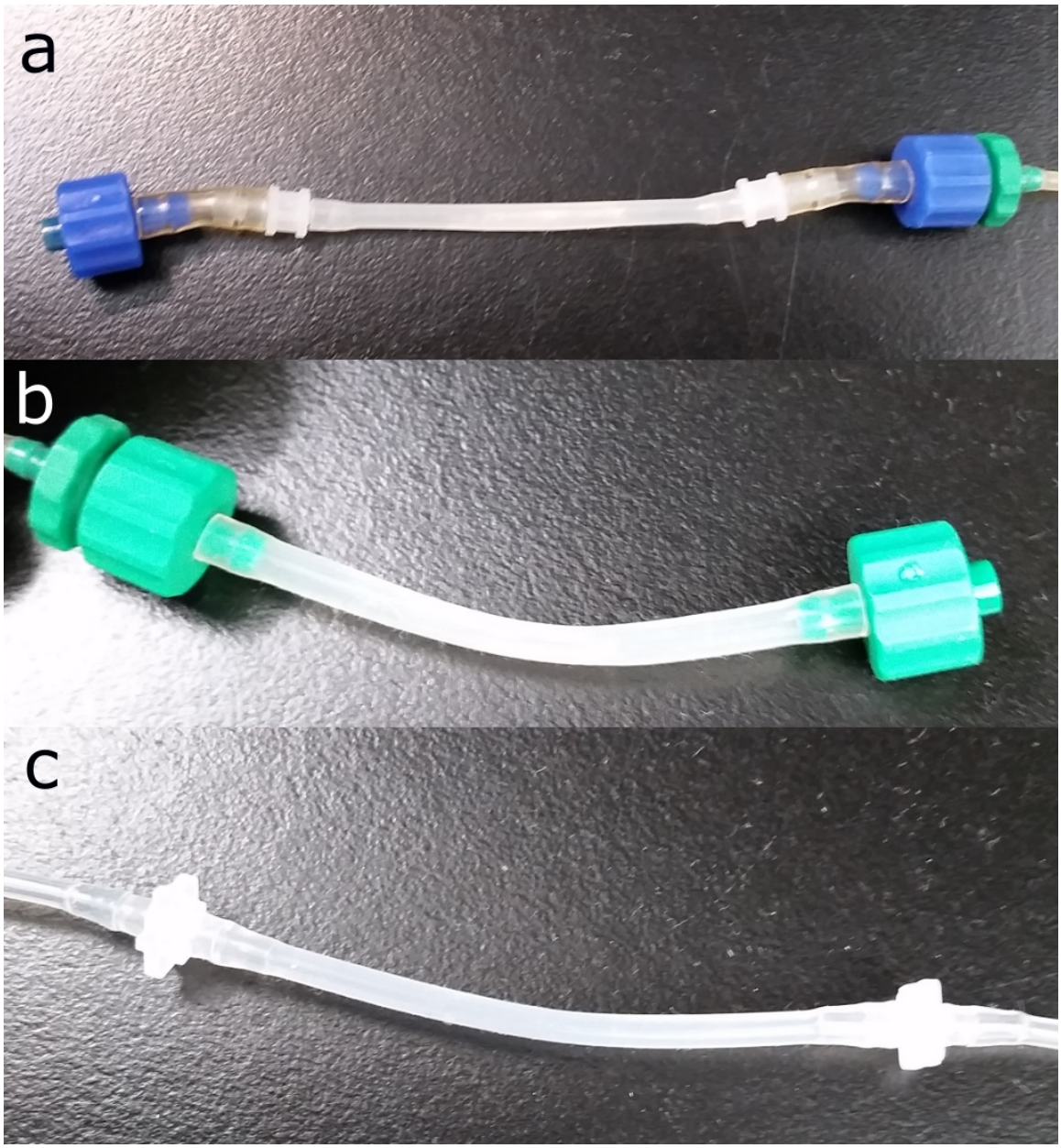


Figure C.3: Custom tube element design. (a) Inflow tube element (1.02 mm ID tubing). (b) Outflow tube element (1.42 mm ID tubing). (c) Microscope pump tube element (0.76 mm ID tubing).

# Appendix D

# Capillary insert design

The design and careful construction of the unique capillary inserts we use is extremely important to our overall experimental design. PDMS microfluidic devices suffer from aging effects and tend to quickly delaminate from glass under the high pressures used in our experiments, and other potentially suitable microfluidic designs (such as clamped glass microfluidic devices) are costly and difficult to produce. In contrast, our capillary inserts are cheap, simple to make, can be repeatedly bleached, washed, and autoclaved for re-use without noticeable aging or degradation, and typically last for years before needing to be replaced. As a result we present a detailed protocol for the design and construction of these capillaries.

Our complete capillary system uses VitroCom 5015 rectangular glass capillaries (nominal 1 x 0.05 mm internal dimensions), 1 mm ID silicone tubes, 6062K1 black-anodized 2" x 0.04" aluminum stock, a ThorLabs CP02T cage mount ("capillary block") with custom machining to mount the capillary inserts, and OD2002 and 730 epoxy from Epoxy Technology. The basic capillary insert structural element (Fig. D.1(a), shaded part) is produced by the following protocol:

1. The 6062K1 aluminum stock is cut into ∼11/16" strips on a bandsaw, and the edges of each strip are filed down.

2. A 3/16" trench is milled through the strip, with the mill traveling a minimum 1.5" distance. Although the hole spacing on the capillary block only mandates a ∼1.3"-length trench, the additional length reduces the accuracy needed to later mount the capillary. Note that tightening the clamp too far can cause the part to snap, and during milling the thin 6062K1 stock nearly always suffers from some amount of small buckling.

3. Both the outside and inside edges must be carefully filed down to remove any

burrs. The edges must be particularly smooth near the center of the milled trench, where the capillary attaches; even tiny raised burrs can tilt the capillary, making it useless for imaging, or in the worst case actually cut through the 0.05 mm capillary wall.

4. The part is put into a steel clamp and flattened to ameliorate the buckling that occurs during milling.

5. Using a ruler and diamond scribe, a thin line is etched across the black-anodized surface over the center of the trench, as shown and explained in Fig. D.1(a). This serves as a guide for attaching the capillary, as shown in Fig. D.1(b).

With the capillary insert plate machined, the capillary itself is produced and attached as follows:

1. VitroCom 5015 capillaries are cut into 1" lengths as shown in Fig. D.1(a) (the nominal 50 mm 5015 stock length can be cut in half to produce two capillaries suitable for use). Attempting to the cut the capillary directly will cause it to shatter; instead, we use a diamond scribe to carefully and gently etch a thin notch across the capillary at the 1" mark. Wetting the notch with a drop of water and bending the capillary away from it will cause it to cleanly cleave in two.

2. The capillary is centered on the guide notched in the capillary insert plate. OD2002 epoxy from Epoxy Technology is mixed (1:20 mass ratio between components A and B), and gently spread over the top of the capillary - carefully avoiding touching the capillary itself with whatever implement is used to spread the epoxy - on both sides of the trench in thin strips. As shown in the picture in Fig. D.1(b), this layer of epoxy must be spread out until it is very thin. The actual epoxy layer thickness cannot typically be measured, but must be $\sim$0.6 mm at most because the working distance of our microscope objective is 0.7 mm and the capillary walls are themselves $\sim$0.05 mm thick. Epoxy should not actually reach the edges of the capillary insert plate, because it will spread outwards over the imaging volume if too close to the inner edges, and tends to complicate later steps if too close to the outer edges. After applying the epoxy, the capillary

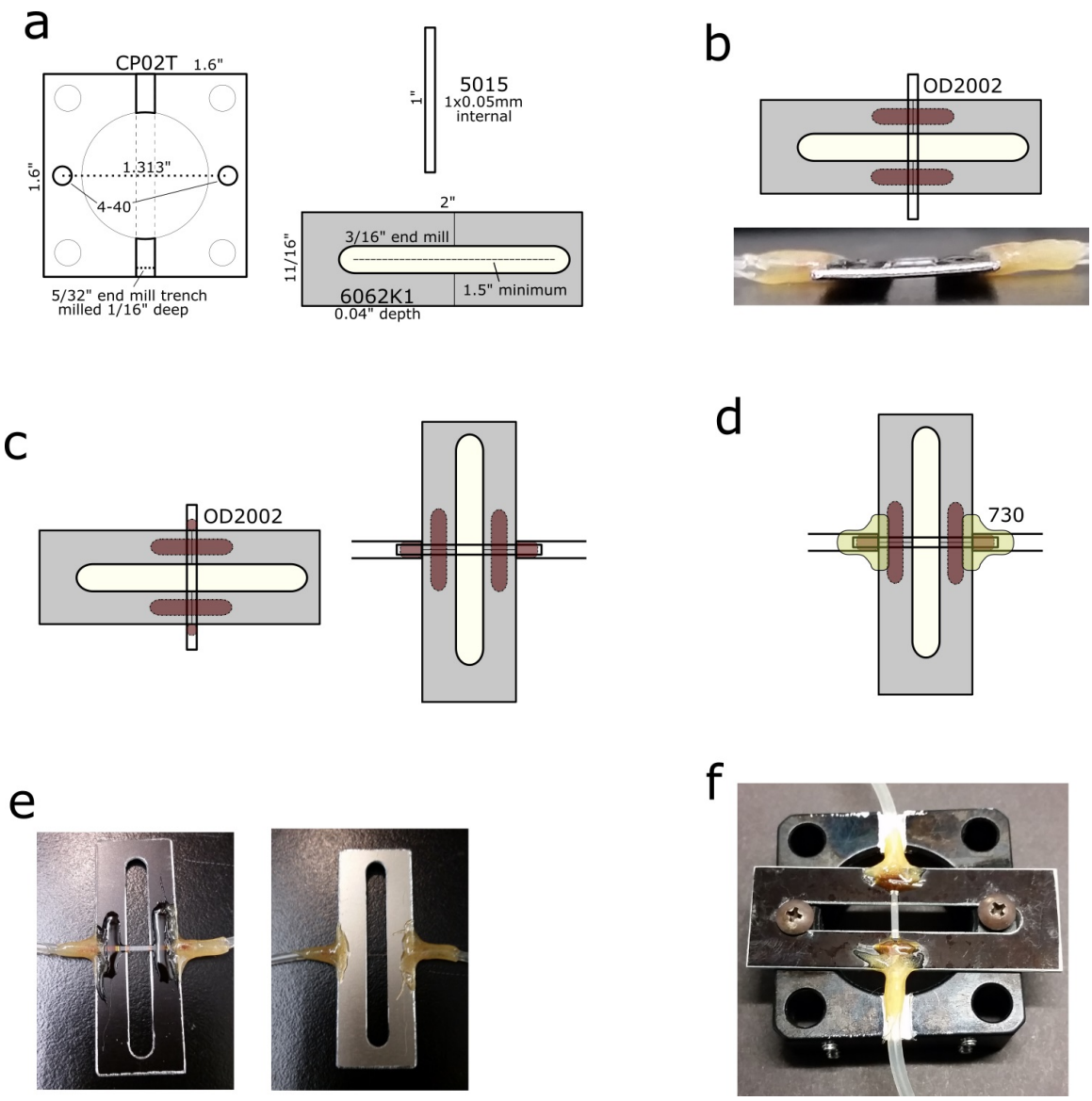


Figure D.1: Capillary insert design. (a) Capillary mounting components, including capillary block (Fig. A.4(a)), black anodized capillary insert, and the capillary itself. Milled trench through capillary insert intentionally off-center of insert to show relevant center line is center of trench. (b) In the first capillary assembly step, capillary is laid over center line and affixed with very thin (<0.6 mm) layer of Epoxy Technology OD2002 epoxy. (c) In the second capillary assembly step, small amounts of additional OD2002 epoxy are used to affix 1 mm ID silicone tubing to capillary ends. (d) In the final capillary assembly step, Epoxy Technology 730 epoxy is used to reinforce tube-capillary connections. (e) Appearance of finished capillary insert. (f) Capillary insert mounted to capillary block. Once correctly positioned, entire assembly can be autoclaved together.

insert is cured in an oven at 150 °C for ∼24 hours. Note that whenever curing epoxy, we use small tabs to slightly elevate the insert above whatever surface it rests on to prevent the epoxy from gluing the insert to the surface.

3. After the capillary insert cools to room temperature, OD2002 epoxy is mixed again, and two small beads are applied to the top surface only of the capillary just off both ends of the plate as shown in Fig. D.1(c). Actually measuring the size of these beads is difficult, but a good rule of thumb is using the minimal amount necessary to cover the top surface from the edge of the plate to the midpoint of the capillary's extension away from the plate. Next, sections of 1 mm silicone tubing are slowly inserted over the capillaries, deliberately rotating the tubes in one direction to spread the epoxy to the lower half of the capillary. The tubes should not be removed after this point, as they will draw epoxy towards the capillary opening, which results in epoxy drawn into the capillary blocking the entrance. The inserts are again cured at 150 °C for 24 hours, with the transfer to the oven carried out carefully - usually in a glass Petri dish - as the long, heavy tubes can easily slip off the capillary ends or cause the capillary ends to snap. Note that capillary action at this stage draw can draw excess epoxy outside the tube inside it and, with enough epoxy supplied, into the capillary itself. In contrast, applying too little epoxy will result in an incomplete seal and leaks.

4. After the capillary inserts cool to room temperature, water is pushed through the tubes from both ends using a syringe with a Luer attached. If the capillary is blocked by epoxy, water cannot flow through, and if the seal is incomplete, the capillary will immediately leak. An improperly made capillary cannot generally be fixed, and while in theory the capillary and epoxy can be scraped from the plate to make a new one, in practice the metal pushed up by this process tends to ruin new inserts made using the same plate. A properly made capillary insert can withstand surprisingly high pressures; in years of use of many capillaries, the capillary-tube interface has never directly been a point of failure. However, at this stage the capillary insert must be handled extremely carefully, as the tube-plate 'joint' is extremely weak and can cause the capillary itself to snap.

5. To strengthen the joint, Epoxy Technology 730 epoxy (mixed at a 1:1 mass ratio between components A and B) is applied liberally to the joint as shown in Fig. D.1(d). The epoxy should be applied in bulk on all sides of the joint, including the empty space to the sides of the tube along the plate edge. Because the capillary insert is centered over a large hole, epoxy can be applied in bulk to the bottom of the plate near the tube (see Fig. D.1(e)); however, epoxy should only be applied for a small distance away from the edge on the top of the plate, to avoid the issues with the objective working distance mentioned in step 2. While 730 epoxy is recommended to be cured at 100 °C, to ensure it could endure repeated autoclaving without substantially changing, we cure 730 epoxy in this step at 121 °C for 24 hours.

6. The capillary insert is attached to the capillary block with 4-40 screws, aligning the silicone tubes with the milled trenches in the block and centering the capillary itself on the center of the hole. While centering the capillary requires careful placement, it can usually be successfully centered on the first or second try. However, it must be tested in the microscope itself before being used in an experiment.

7. Once correctly centered and verified as appropriate for imaging, the capillary insert never needs to be removed from the capillary block until it needs to be replaced. The two parts can be moved and autoclaved together as a single unit.

# Appendix E

# Manual time series cleanup

Images in our experiments are automatically segmented and labeled, and the resulting data is automatically run through several quality-checking programs designed to remove low-quality data, culminating in the generation of a 'final' automatically-generated time series (see Fig. 2.5 and Section 2.4.6). However, to preserve as much data as possible, the thresholds for automatically throwing out data are intentionally chosen conservatively, and data from seriously flawed images may still make it into this 'final' automatic time series. Therefore, the automatically-generated time series are manually examined for anomalies, which are typically easily visible by eye, and low-quality data is stripped out by hand (see Fig. E.1) before growth rate estimation is attempted. To confirm that apparent anomalies in the time series are actually due to low-quality or irrelevant data, images from the seemingly-anomalous region are examined to confirm the presence of one or more of the following five problems:

1. Bubbles in the imaging volume. While extremely large bubbles seriously distort the spatial distribution of cells, the thresholds chosen for automatic detection of this problem are so conservative that smaller bubbles are frequently not detected. Bubbles in the imaging volume can persist for many minutes (in rare cases, several hours), and images containing all but the smallest bubbles can generally be discarded as they can easily lower cell counts by over half. This is by far the most common problem in images discarded by hand, accounting for well over half of anomalous regions discarded from time series.

2. Extremely large bubbles near the imaging volume (Fig. E.2). In some cases, bubbles are not visible in the imaging volume, but their presence can be inferred by the distorted flow of cells around them. Typically this also results in a reduction in apparent cell counts as cells will be moving too fast near the bubble

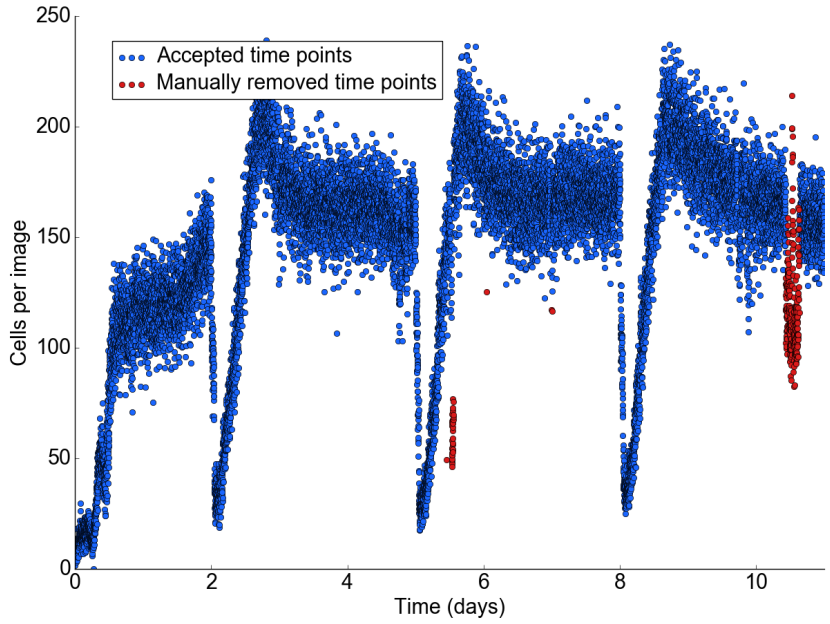


Figure E.1: Manual removal of poor data from computer-generated time series. All time points are present in computer-generated time series. Red time points were removed by hand due to imaging problems apparent on manual inspection of time series and microscope images, but not properly handled by the conservative automatic quality assessment algorithms.

to be properly segmented, but in some cases bubbles can cause a spike in the apparent number of cells detected, as some cells may become stuck in or near the liquid-air interface, without the void in the imaging volume when the bubble actually appears within it. This problem makes up most of the remaining anomalous regions in automatically-generated time series.

3. An immediate, dramatic spike in cell density, populated by extremely bright cells. The exact cause of this problem is not known, but because cells adhered to the vial walls or tubes are expected to be in or near stationary-phase and extremely bright, and because these events are extremely localized in time (sometimes characterized by cells entering and leaving the imaging volume in a near-opaque 'sheet' over the course of several minutes), we suspect they are caused by the sudden breakup or 'release' of wall growth in the tubes. Smaller-scale versions of this problem can generally be confirmed by the presence of a large subpopulation of extremely bright cells over a brief period of time, along with rapid increase then drop in cell density.

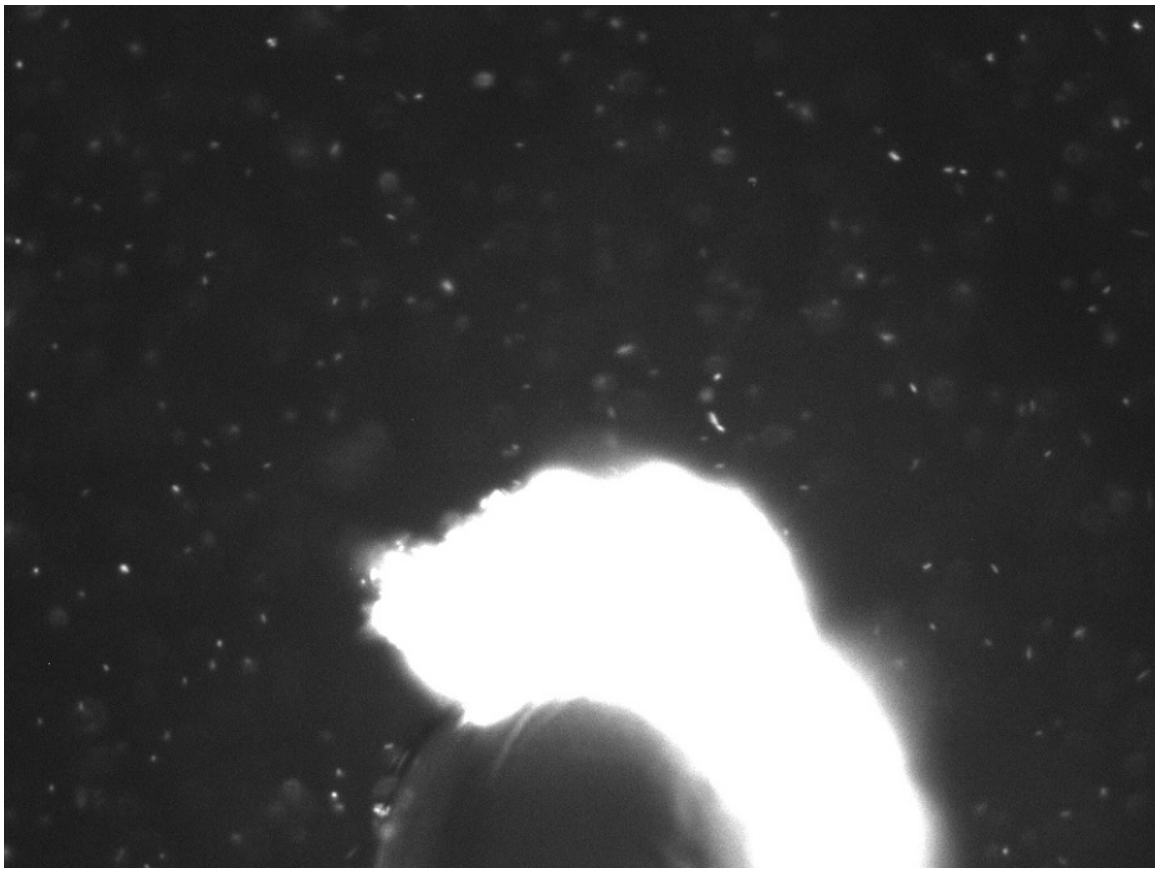

Figure E.2: Example image from first anomalous time series section removed by hand in Fig. E.1. Image contains both a large bubble temporarily trapped in the imaging volume and a large cluster of aggregated cells wedged between the capillary walls and the liquid-air interface of the bubble. Presence of bubble and cell aggregate dramatically reduced measured abundance of planktonic cells (Fig. E.1), but disturbance persisted long enough for data to be included in automatically-generated time series (Section 2.4.6).

4. Rarely, cell aggregates can get 'stuck' in the imaging volume (Fig. E.2). Depending on the structure and placement of the cell aggregate, this can cause a drop in the number of detected cells as the aggregate saturates the detector over a large region, or a spike in the number of detected cells as other cells get stuck at the aggregate boundary. In several instances an aggregate has become permanently attached to the capillary, effectively ending the experiment so that the capillary can be bleached to remove it.

5. Rarely, imaging quality overall may drop for unexplained reasons for an extended period of time, as vibrations in the line result in cells moving so fast they cannot be detected, or causing them to oscillate in place, resulting in an apparent 'doubling' in some cell counts. While this problem likely occurs with some regularity on the scale of one or two minutes, it makes up a small portion of anomalous regions removed by hand because it is uncommon for it to persist long enough or have an effect dramatic enough to be apparent by looking at a time series. However, a random sampling of images taken in each experiment confirms that this problem is not present in the vast majority of images, and the potential impact of scattered, individual low-quality images on our results is minimal.

# Appendix F

# Experimental protocols

## F.1 Media preparation protocol

1. The following solutions are prepared ahead of time:
    - 10x $(NH_4)_2SO_4$ stock solution ($20\,g\,L^{-1}$, autoclaved, stored at room temperature)
    - 10x $KH_2PO_4$ stock solution ($136\,g\,L^{-1}$, titrated to pH 7 with KOH, autoclaved, stored at room temperature; only Fisher Scientific $KH_2PO_4$ was used as other nominally equivalent brands were found to precipitate out of solution over time)
    - 1M $MgSO_4{\cdot}7H_2O$ stock solution (autoclaved, stored in refrigerator)
    - $FeSO_4{\cdot}7H_2O$ stock solution (500 mg/200 mL, filter-sterilized, made fresh every time M63 media was made)
    - 20 % w/v glucose stock solution (filter-sterilized, stored in refrigerator)
    - $25\,mg\,mL^{-1}$ chloramphenicol stock solution in ethanol (filter-sterilized, stored in -20 °C freezer)
2. Due to the large quantity of media used in each experiment, M63 media was prepared in 1 L bottles. The final mixing quantities added were in order:
    - 800 mL autoclaved Millipore water
    - 100 mL $(NH_4)_2SO_4$ stock solution (final concentration: 15 mM)
    - 100 mL $KH_2PO_4$ stock solution (final concentration: 100 mM)
    - 1 mL $MgSO_4{\cdot}7H_2O$ stock solution (final concentration: 1 mM)
    - 0.2 mL $FeSO_4{\cdot}7H_2O$ stock solution (final concentration: $0.5\,mg\,L^{-1}$)

- 2 mL glucose stock solution (final concentration: 0.04 % w/v)
- 0.5 mL chloramphenicol stock solution (final concentration: 12.5 µg $mL^{-1}$)

3. Media was vigorously mixed after each liter was prepared, and placed in the environmental room at least one day in advance of use to thermalize to 30 °C.

## F.2 Continuous-culture experiment setup protocol

1. For each system being run, the following are prepared:

   - One sterilized 1 L media bottle with sterile M63 media, thermalized to 30 °C in the environmental room at least one day in advance of the experiment start date.
   - One sterilized 1 L media bottle with cleaned input bottle cap, with a tube terminating in a male Luer attached to an inflow pump tube element wrapped in aluminum foil.
   - One sterilized 1 L media bottle with cleaned output bottle cap, with a tube terminating with a female Luer and no tube element, also wrapped in aluminum foil.
   - One sterilized 40 L Chemglass CG-4902-08 vial, containing one cleaned 15 mm × 4.5 mm SBM-15045-PLA stir bar and covered with a plastic flask cap. Although Chemglass sells nominally autoclavable solid screw caps for the vials, they were found to degrade after many rounds of autoclave sterilization.
   - One sterilized 40 mL CG-4902-08 vial, with attached custom 3D-printed cap and cleaned tubing and capillary, with two open tube ends covered in foil: a tube terminating in a male Luer attached to an outflow pump tube element, and a tube terminating in a female Luer and no tube elements. Terminating the tubes in different Luer types ensures the correct bottle (input or output) is attached to the correct line.

   In addition, a separate sterilized media bottle with identically-prepared sterile M63 media, referred to as the inoculation media bottle, is also allowed to thermalize to 30 °C in the environmental room at least one day in advance of flask culture inoculation.

2. Three days prior to experiment start, frozen *E. coli* stock is streaked onto LB plates and placed in an incubator at 30 °C.

3. Two days prior to experiment start, single colonies are taken from the LB plates and used to inoculate two flasks filled with 75 mL of inoculation media each. The flasks are placed in a 30 °C shaker operating at 200 rpm, in which 2 days should be sufficient time for the cultures to grow to be optically dense by eye. If the culture is not visibly optically dense, the density of bacteria in the culture is typically too low to observe in the microscope. Temperature control code on the continuous-culture control computers is activated to make sure the systems start near 30 °C on the day of the experiment.

4. On the day of the experiment, at least one of the flask cultures should be optically dense. For each sterilized vial containing a stir bar, 10 mL of sterile inoculation media is added, followed by 10 mL of culture from the optically dense flask, with the 2-fold dilution intended to ensure the cells aren't in the process of entering stationary phase at the beginning of the experiment. These 6 vials are taken into the environmental room and placed in the continuous-culture devices with pumps already operating at 800 rpm, so that the separate vials stay at 30 °C and under identical conditions for as long as possible.

5. One at a time, vials are taken out of the environmental room, and the custom cap (and associated tubing) from the separate sterile vial are swapped with the cap on the vial containing bacterial culture. The outside of the culture vial is rinsed with isopropyl alcohol and wiped with a Kimwipe to make it as clear as possible for optical density measurement, then the culture vial (and tubes and capillaries) are returned to its system in the environmental room. The capillary is temporarily affixed to the microscope to reduce the odds of it breaking. The remaining vial, which is now empty but still sterile, is kept until the end of the experiment.

6. One at a time for each system, the following tasks are completed:

    - The input media bottle cap is switched with the cap on the media bottle containing actual M63 media (although contamination did not occur in any

experiment, this step is performed so late to reduce the odds and impact of accidental contamination and subsequent growth in the media bottle).

- The tube ends from the input and output media bottle caps are attached to the tube ends from the culture vial.
- The input pump is manually activated to draw media from the input bottle to the input vial before being stopped, to ensure that when the pump first activates in the experiment it is already adding media to the culture.
- The microscope pump is manually activated to draw bacterial culture into the capillary.

7. The microscopes are focused on the center of the capillary. First, the microscope LED is turned on and FlyCapture GUI software is activated to show video from the microscope cameras. The capillary blocks are slowly moved by hand until cells or debris on the capillary exterior are visible, at which point the capillary block is screwed into place, with the Z stage controlling objective position carefully adjusted to keep objects visible in the camera. Once the capillary block is fully screwed in place, the center of the capillary is brought into focus by using the micron-scale knob on the objective Z stage to find both inside edges of the capillary, then returning to the midpoint. Note that this procedure is only possible in the presence of fluorescent cells, as the edges of the capillary can only be detected by the presence of physically stationary or very slow-moving cells.

8. When all systems have been fully set up, camera software is closed and the continuous-culture control code is run on all systems simultaneously, beginning the experiment. Initial images saved from the microscope are checked for potential problems before the experiment is allowed to run unattended.

9. Experiment vials, input and output bottles, and recent microscope images are checked daily for problems. Direct optical observation of the experiment vials requires lifting them out of the continuous-culture device for a few seconds. This disrupts the optical density measurement, but is necessary to avoid rare but serious problems (such as culture overflow, leaks in tubes, etc.).

10. At the end of the experiment, if desired, the sterile vial caps from the leftover

vials can be used again to cap the final bacterial culture for transfer out of the environmental room to take samples for freezing.

## F.3 Equipment cleaning protocols

1. After an experiment finishes, the input media bottle is removed and all three pumps are manually activated until all liquid is emptied from the lines (typically 3 minutes of operation).

2. Leftover culture in attached vial is bleached and discarded, then the vial is filled with 40 mL of at least 20 % bleach solution, and the microscope and output pumps are manually activated for 10 minutes to sterilize the inside of the contaminated tubing. Attempting this step with ethanol solution was found early on to be inappropriate as it does not break up accumulated biofilm on the walls of the tubes. Afterwards, all liquid is emptied from the lines again, and the bleach solution remaining in the vial is discarded.

3. Vials and input bottles are filled with 30-50 mL each of Millipore water, and all three pumps are manually activated for 15 minutes to rinse the tubing of various salts, leftover bleach, etc. Afterwards, all liquid is emptied from the lines again.

4. Media bottles and vials are washed in the lab dishwasher. Stir bars are too small for this step, and are cleaned by hand via scrubbing with bleach, followed by ethanol, followed by Millipore water.

5. Immediately prior to sterilization for an experiment, all surfaces except tube interiors undergo a final cleaning step. Glassware is rinsed with Millipore water to remove any residue left behind by tap water from the dishwasher. Stir bars are scrubbed again with ethanol and Millipore water. Finally, the PEEK tubing attached to the input bottle and custom vial caps, which is in direct contact with media or bacterial culture, is cleaned by rinsing with ethanol and wiping with a Kimwipe, followed by rinsing with Millipore water.

# References


[1] Savageau, M. A. *Escherichia coli* habitats, cell types, and molecular mechanisms of gene control. *The American Naturalist 122*, 6 (Dec. 1983), 732–744.

[2] Seymour, J. R., Amin, S. A., Raina, J.-B., and Stocker, R. Zooming in on the phycosphere: the ecological interface for phytoplankton–bacteria relationships. *Nature Microbiology 2*, 17065 (May 2017), 1–12.

[3] Howes, B. L., and Goehringer, D. D. Porewater drainage and dissolved organic carbon and nutrient losses through the intertidal creekbanks of a New England salt marsh. *Marine Ecology Progress Series 114* (Nov. 1994), 289–301.

[4] Vaulot, D., Marie, D., Olson, R. J., and Chisholm, S. W. Growth of *Prochlorococcus*, a photosynthetic prokaryote, in the equatorial Pacific Ocean. *Science 268*, 5216 (June 1995), 1480–1482.

[5] Fisher, T. R., Gustafson, A. B., Sellner, K., Lacouture, R., Haas, L. W., Wetzel, R. L., Magnien, R., Everitt, D., Michaels, B., and Karrh, R. Spatial and temporal variation of resource limitation in Chesapeake Bay. *Marine Biology 133*, 4 (May 1999), 763–778.

[6] Thompson, J. R., Randa, M. A., Marcelino, L. A., Tomita-Mitchell, A., Lim, E., and Polz, M. F. Diversity and dynamics of a North Atlantic coastal *Vibrio* community. *Applied and Environmental Microbiology 70*, 7 (July 2004), 4103–4110.

[7] Trainer, V. L., Adams, N. G., Bill, B. D., Anulacion, B. F., and Wekell, J. C. Concentration and dispersal of a *Pseudo-nitzschia* bloom in Penn Cove, Washington, USA. *Natural Toxins 6*, 3-4 (May 1998), 113–126.

[8] van Elsas, J. D., Chiurazzi, M., Mallon, C. A., Elhottovā, D., Krištůfek, V., and Salles, J. F. Microbial diversity determines the invasion of soil by a bacterial pathogen. *Proceedings of the National Academy of Sciences of the United States of America 109*, 4 (Jan. 2012), 1159–1164.

[9] Lennon, J. T., and Cottingham, K. L. Microbial productivity in variable resource environments. *Ecology 89*, 4 (Apr. 2008), 1001–1014.

[10] Young, T. B., Bruley, D. F., and Bungay, H. R. 3rd. A dynamic mathematical model of the chemostat. *Biotechnology and Bioengineering 12*, 5 (Sept. 1970), 747–769.

[11] Notley-McRobb, L., King, T., and Ferenci, T. *rpoS* mutations and loss of general stress resistance in *Escherichia coli* populations as a consequence of conflict between competing stress responses. *Journal of Bacteriology 184*, 3 (Feb. 2002), 806–811.

[12] Zambrano, M. M., and Kolter, R. GASPing for life in stationary phase. *Cell 86*, 2 (July 1996), 181–184.

[13] Novick, A., and Weiner, M. Enzyme induction as an all-or-none phenomenon. *Proceedings of the National Academy of Sciences of the United States of America 43*, 7 (July 1957), 553–566.

[14] Loomis, W. F., and Magasanik, B. Glucose-lactose diauxie in *Escherichia coli*. *Journal of Bacteriology 93*, 4 (Apr. 1967), 1397–1401.

[15] Helling, R. B., Vargas, C. N., and Adams, J. Evolution of *Escherichia coli* during growth in a constant environment. *Genetics 116*, 3 (July 1987), 349–358.

[16] Prüss, B. M., Nelms, J. M., Park, C., and Wolfe, A. J. Mutations in NADH:ubiquinone oxidoreductase of *Escherichia coli* affect growth on mixed amino acids. *Journal of Bacteriology 176*, 8 (Apr. 1994), 2143–2150.

[17] Battesti, A., Majdalani, N., and Gottesman, S. The RpoS-mediated general stress response in *Escherichia coli*. *Annual Review of Microbiology 65* (Oct. 2011), 189–213.

[18] Lévi-Meyrueis, C., Monteil, V., Sismeiro, O., Dillies, M.-A., Monot, M., Jagla, B., Coppée, J.-Y., Dupuy, B., and Norel, F. Expanding the RpoS/$\sigma^s$-network by RNA sequencing and identification of $\sigma^s$-controlled small RNAs in *Salmonella*. *PLOS ONE 9*, 5 (May 2014), e96918.

[19] Scott, M., Gunderson, C. W., Mateescu, E. M., Zhang, Z., and Hwa, T. Interdependence of cell growth and gene expression: origins and consequences. *Science 330*, 6007 (Nov. 2010), 1099–1102.

[20] Scott, M., Klumpp, S., Mateescu, E. M., and Hwa, T. Emergence of robust growth laws from optimal regulation of ribosome synthesis. *Molecular Systems Biology 10*, 747 (Aug. 2014).

[21] Levin-Reisman, I., Gefen, O., Fridman, O., Ronin, I., Shwa, D., Sheftel, H., and Balaban, N. Q. Automated imaging with ScanLag reveals previously undetectable bacterial growth phenotypes. *Nature Methods 7*, 9 (Sept. 2010), 737–739.

[22] Madar, D., Dekel, E., Bren, A., Zimmer, A., Porat, Z., and Alon, U. Promoter activity dynamics in the lag phase of *Escherichia coli*. *BMC Systems Biology 7*, 136 (Dec. 2013), 1–13.

[23] Lambert, G., and Kussell, E. Memory and fitness optimization of bacteria under fluctuating environments. *PLOS Genetics 10*, 9 (Sept. 2014), e1004556.

[24] Min, T. L., Mears, P. J., Golding, I., and Chemla, Y. R. Chemotactic adaptation kinetics of individual *Escherichia coli* cells. *Proceedings of the National Academy of Sciences of the United States of America 109*, 25 (June 2012), 9869–9874.

[25] Bennett, A. F., Lenski, R. E., and Mittler, J. E. Evolutionary adaptation to temperature. I. Fitness responses of *Escherichia coli* to changes in its thermal environment. *Evolution: International Journal of Organic Evolution 46*, 1 (Feb. 1992), 16–30.

[26] Leroi, A. M., Lenski, R. E., and Bennett, A. F. Evolutionary adaptation to temperature. III. Adaptation of *Escherichia coli* to a temporally varying environment. *Evolution: International Journal of Organic Evolution 48*, 4 (Aug. 1994), 1222–1229.

[27] Widder, S., Allen, R. J., Pfeiffer, T., Curtis, T. P., Wiuf, C., Sloan, W. T., Cordero, O. X., Brown, S. P., Momeni, B., Shou, W., Kettle, H., Flint, H. J., Haas, A. F., Laroche, B., Kreft, J.-U., Rainey, P. B., Freilich, S., Schuster, S., Milferstedt, K., van der Meer, J. R., Gro$\beta$kopf, T., Huisman, J., Free, A., Picioreanu, C., Quince, C., Klapper, I., Labarthe, S., Smets, B. F., Wang, H., Isaac Newton Institute Fellows, and Soyer, O. S. Challenges in microbial ecology: building predictive understanding of community function and dynamics. *The ISME Journal 10*, 11 (Nov. 2016), 2557–2568.

[28] Smalley, D., Conway, T., and Chang, D. Gene expression profiling of *Escherichia coli* growth transitions: an expanded stringent response model. *Molecular Microbiology 45*, 2 (July 2002), 289–306.

[29] Suarez-Mendez, C., Sousa, A., Heijnen, J., and Wahl, A. Fast "feast/famine" cycles for studying microbial physiology under dynamic conditions: a case study with *Saccharomyces cerevisiae*. *Metabolites 4*, 2 (June 2014), 347–372.

[30] Balaban, N. Q., Merrin, J., Chait, R., Kowalik, L., and Leibler, S. Bacterial persistence as a phenotypic switch. *Science 305*, 5690 (Sept. 2004), 1622–1625.

[31] Larsen, S. H., Reader, R. W., Kort, E. N., Tso, W.-W., and Adler, J. Change in direction of flagellar rotation is the basis of the chemotactic response in *Escherichia coli*. *Nature 249*, 452 (May 1974), 74–77.

[32] Métris, A., Lemarc, Y., Elfwing, A., Ballagi, A., and Baranyi, J. Modelling the variability of lag times and the first generation times of single cells of *E. coli*. *International Journal of Food Microbiology 100*, 1-3 (Apr. 2005), 13–19.

[33] Dai, X., Zhu, M., Warren, M., Balakrishnan, R., Patsalo, V., Okano, H., Williamson, J. R., Fredrick, K., Wang, Y.-P., and Hwa, T. Reduction of translating ribosomes enables *Escherichia coli* to maintain elongation rates during slow growth. *Nature Microbiology 2*, 16231 (Dec. 2016).

[34] Zundel, M. A., Basturea, G. N., and Deutscher, M. P. Initiation of ribosome degradation during starvation in *Escherichia coli*. *RNA 15*, 5 (May 2009), 977–983.

[35] Vázquez-Laslop, N., Lee, H., and Neyfakh, A. A. Increased persistence in *Escherichia coli* caused by controlled expression of toxins or other unrelated proteins. *Journal of Bacteriology 188*, 10 (May 2006), 3494–3497.

[36] Patra, P., and Klumpp, S. Population dynamics of bacterial persistence. *PLOS ONE 8*, 5 (May 2013), e62814.

[37] Leszczynska, D., Matuszewska, E., Kuczynska-Wisnik, D., Furmanek-Blaszk, B., and Laskowska, E. The formation of persister cells in stationary-phase cultures of *Escherichia coli* is associated with the aggregation of endogenous proteins. *PLOS ONE 8*, 1 (Jan. 2013), e54737.

[38] Schleheck, D., Barraud, N., Klebensberger, J., Webb, J. S., McDougald, D., Rice, S. A., and Kjelleberg, S. *Pseudomonas aeruginosa* PAO1 preferentially grows as aggregates in liquid batch cultures and disperses upon starvation. *PLOS ONE 4*, 5 (May 2009), e5513.

[39] McDougald, D., Rice, S. A., Barraud, N., Steinberg, P. D., and Kjelleberg, S. Should we stay or should we go: mechanisms and ecological consequences for biofilm dispersal. *Nature Reviews Microbiology 10*, 1 (Nov. 2011), 39–50.

[40] Ito, A., May, T., Kawata, K., and Okabe, S. Significance of *rpoS* during maturation of *Escherichia coli* biofilms. *Biotechnology and Bioengineering 99*, 6 (Apr. 2008), 1462–1471.

[41] Ito, A., Taniuchi, A., May, T., Kawata, K., and Okabe, S. Increased antibiotic resistance of *Escherichia coli* in mature biofilms. *Applied and Environmental Microbiology 75*, 12 (June 2009), 4093–4100.

[42] Liu, J., Prindle, A., Humphries, J., Gabalda-Sagarra, M., Asally, M., Lee, D.-y. D., Ly, S., Garcia-Ojalvo, J., and Süel, G. M. Metabolic co-dependence gives rise to collective oscillations within biofilms. *Nature 523*, 7562 (July 2015), 550–554.

[43] Goguen, J. D. *The population biology of bacteria and their plasmids: some effects of surface populations*. PhD thesis, University of Massachusetts, 1980.

[44] Dykhuizen, D. E., and Hartl, D. L. Selection in chemostats. *Microbiol. Rev. 47*, 2 (June 1983), 150–168.

[45] Yan, J., Nadell, C. D., and Bassler, B. L. Environmental fluctuation governs selection for plasticity in biofilm production. *The ISME Journal 11*, 7 (July 2017), 1569–1577.

[46] Unanue, M., Ayo, B., Azúa, I., Barcina, I., and Iriberri, J. Temporal variability of attached and free-living bacteria in coastal waters. *Microbial Ecology 23*, 1 (Jan. 1992), 27–39.

[47] Novick, A., and Szilard, L. Description of the chemostat. *Science 112*, 2920 (Dec. 1950), 715–716.

[48] Lenski, R. E., Rose, M. R., Simpson, S. C., and Tadler, S. C. Long-term experimental evolution in *Escherichia coli*. I. Adaptation and divergence during 2,000 generations. *The American Naturalist 138*, 6 (Dec. 1991), 1315–1341.

[49] Phillips, J. N., and Myers, J. Measurement of algal growth under controlled steady-state conditions. *Plant Physiology 29*, 2 (Mar. 1954), 148–152.

[50] Toprak, E., Veres, A., Michel, J.-B., Chait, R., Hartl, D. L., and Kishony, R. Evolutionary paths to antibiotic resistance under dynamically sustained drug selection. *Nature Genetics 44*, 1 (Jan. 2012), 101–105.

[51] Balagaddé, F. K., You, L., Hansen, C. L., Arnold, F. H., and Quake, S. R. Long-term monitoring of bacteria undergoing programmed population control in a microchemostat. *Science 309*, 5731 (July 2005), 137–140.

[52] Groisman, A., Lobo, C., Cho, H., Campbell, J. K., Dufour, Y. S., Stevens, A. M., and Levchenko, A. A microfluidic chemostat for experiments with bacterial and yeast cells. *Nature Methods 2*, 9 (Sept. 2005), 685–689.

[53] Chiesa, S. C., Irvine, R. L., and Manning, J. F. Feast/famine growth environments and activated sludge population selection. *Biotechnology and Bioengineering 27*, 5 (May 1985), 562–568.

[54] Eppley, R. W., Holmes, R. W., and Paasche, E. Periodicity in cell division and physiological behavior of *ditylum brightwellii*, a marine planktonic diatom, during growth in light-dark cycles. *Archiv für Mikrobiologie 56*, 4 (Dec. 1967), 305–323.

[55] Nelson, D. M., and Brand, L. E. Cell division periodicity in 13 species of marine phytoplankton on a light: dark cycle. *Journal of Phycology 15*, 1 (Mar. 1979), 67–75.

[56] Chisholm, S. W., Stross, R. G., and Nobbs, P. A. Light/dark-phased cell division in *Euglena gracilis* (z) (euglenophyceae) in $PO_4$-limited continuous culture. *Journal of Phycology 11*, 4 (Dec. 1975), 367–373.

[57] Bohannan, B. J. M., and Lenski, R. E. Effect of resource enrichment on a chemostat community of bacteria and bacteriophage. *Ecology 78*, 8 (Dec. 1997), 2303–2315.

[58] Storer, F. F., and Gaudy, A. F. Jr. Computational analysis of transient response to quantitative shock loadings of heterogeneous populations in continuous culture. *Environmental Science & Technology 3*, 2 (Feb. 1969), 143–149.

[59] Yoshida, T., Ellner, S. P., Jones, L. E., Bohannan, B. J. M., Lenski, R. E., and Hairston, N. G. Jr. Cryptic population dynamics: rapid evolution masks trophic interactions. *PLOS Biology 5*, 9 (Sept. 2007), e235.

[60] Toprak, E., Veres, A., Yildiz, S., Pedraza, J. M., Chait, R., Paulsson, J., and Kishony, R. Building a morbidostat: an automated continuous-culture device for studying bacterial drug resistance under dynamically sustained drug inhibition. *Nature Protocols 8*, 3 (Mar. 2013), 555–567.

[61] Wang, P., Robert, L., Pelletier, J., Dang, W. L., Taddei, F., Wright, A., and Jun, S. Robust growth of *Escherichia coli*. *Current Biology 20*, 12 (June 2010), 1099–1103.

[62] Moore, L. S., Stolovicki, E., and Braun, E. Population dynamics of metastable growth-rate phenotypes. *PLOS ONE 8*, 12 (Dec. 2013), e81671.

[63] Frentz, Z., Kuehn, S., and Leibler, S. Strongly deterministic population dynamics in closed microbial communities. *Physical Review X 5*, 4 (Oct. 2015), 041014.

[64] Frentz, Z., Kuehn, S., Hekstra, D., and Leibler, S. Microbial population dynamics by digital in-line holographic microscopy. *Review of Scientific Instruments 81*, 8 (Aug. 2010), 084301.

[65] Merritt, J., and Kuehn, S. Quantitative high-throughput population dynamics in continuous-culture by automated microscopy. *Scientific Reports 6* (Sept. 2016), 33173.

[66] Merritt, J., and Kuehn, S. Frequency- and amplitude-dependent microbial population dynamics during cycles of feast and famine. *Physical Review Letters 121* (Aug. 2018), 098101.

[67] Lindeberg, T., and Eklundh, J. O. Scale detection and region extraction from a scale-space primal sketch. *International Conference on Computer Vision 1990* (Dec. 1990), 416–426.

[68] Tsai, W.-H. Moment-preserving thresolding: a new approach. *Computer Vision, Graphics, and Image Processing 29*, 3 (Mar. 1985), 377–393.

[69] Ferraris, R. P., Yasharpour, S., Lloyd, K. C., Mirzayan, R., and Diamond, J. M. Luminal glucose concentrations in the gut under normal conditions. *The American Journal of Physiology 259*, 5 Pt 1 (Nov. 1990), G822–837.

[70] Rothe, M., Alpert, C., Engst, W., Musiol, S., Loh, G., and Blaut, M. Impact of nutritional factors on the proteome of intestinal *Escherichia coli*: induction of OxyR-dependent proteins AhpF and Dps by a lactose-rich diet. *Applied and Environmental Microbiology 78*, 10 (May 2012), 3580–3591.

[71] Boyer, E. W., Hornberger, G. M., Bencala, K. E., and McKnight, D. M. Response characteristics of DOC flushing in an alpine catchment. *Hydrological Processes 11*, 12 (Oct. 1997), 1635–1647.

[72] Wick, L. M., Weilenmann, H., and Egli, T. The apparent clock-like evolution of *Escherichia coli* in glucose-limited chemostats is reproducible at large but not at small population sizes and can be explained with Monod kinetics. *Microbiology 148*, Pt 9 (Sept. 2002), 2889–2902.

[73] Maharjan, R., Seeto, S., Notley-McRobb, L., and Ferenci, T. Clonal adaptive radiation in a constant environment. *Science 313*, 5786 (July 2006), 514–517.

[74] Pin, C., and Baranyi, J. Single-cell and population lag times as a function of cell age. *Applied and Environmental Microbiology 74*, 8 (Apr. 2008), 2534–2536.

[75] Sauer, K., Cullen, M. C., Rickard, A. H., Zeef, L. A. H., Davies, D. G., and Gilbert, P. Characterization of nutrient-induced dispersion in *Pseudomonas aeruginosa* PAO1 biofilm. *Journal of Bacteriology 186*, 21 (Nov. 2004), 7312–7326.

[76] Reisner, A., Haagensen, J., Schembri, M. A., Zechner, E. L., and Molin, S. Development and maturation of *Escherichia coli* K-12 biofilms. *Molecular Microbiology 48*, 4 (May 2003), 933–946.

[77] Laganenka, L., Colin, R., and Sourjik, V. Chemotaxis towards autoinducer 2 mediates autoaggregation in *Escherichia coli*. *Nature Communications 7* (Sept. 2016), 12984.

[78] Senn, H., Lendenmann, U., Snozzi, M., Hamer, G., and Egli, T. The growth of *Escherichia coli* in glucose-limited chemostat cultures: a re-examination of the kinetics. *Biochimica et Biophysica Acta 1201*, 3 (Dec. 1994), 424–436.

[79] Olsén, A., Jonsson, A., and Normark, S. Fibronectin binding mediated by a novel class of surface organelles on *Escherichia coli*. *Nature 338*, 6217 (Apr. 1989), 652–655.

[80] Shapiro, B. J., Friedman, J., Cordero, O. X., Preheim, S. P., Timberlake, S. C., Szabó, G., Polz, M. F., and Alm, E. J. Population genomics of early events in the ecological differentiation of bacteria. *Science 336*, 6077 (Apr. 2012), 48–51.

[81] Datta, M. S., Sliwerska, E., Gore, J., Polz, M. F., and Cordero, O. X. Microbial interactions lead to rapid micro-scale successions on model marine particles. *Nature Communications 7* (June 2016), 11965.

[82] Louca, S., Polz, M. F., Mazel, F., Albright, M. B. N., Huber, J. A., O'Connor, M. I., Ackermann, M., Hahn, A. S., Srivastava, D. S., Crowe, S. A., Doebeli, M., and Parfrey, L. W. Function and functional redundancy in microbial systems. *Nature Ecology & Evolution 2*, 6 (June 2018), 936–943.

[83] Louca, S., Parfrey, L. W., and Doebeli, M. Decoupling function and taxonomy in the global ocean microbiome. *Science 353*, 6305 (Sept. 2016), 1272–1277.

[84] Fernandez, A. S., Hashsham, S. A., Dollhopf, S. L., Raskin, L., Glagoleva, O., Dazzo, F. B., Hickey, R. F., Criddle, C. S., and Tiedje, J. M. Flexible community structure correlates with stable community function in methanogenic bioreactor communities perturbed by glucose. *Applied and Environmental Microbiology 66*, 9 (Sept. 2000), 4058–4067.

[85] Gentile, M., Yan, T., Tiquia, S. M., Fields, M. W., Nyman, J., Zhou, J., and Criddle, C. S. Stability in a denitrifying fluidized bed reactor. *Microbial Ecology 52*, 2 (Aug. 2006), 311–321.

[86] Vanwonterghem, I., Jensen, P. D., Dennis, P. G., Hugenholtz, P., Rabaey, K., and Tyson, G. W. Deterministic processes guide long-term synchronised population dynamics in replicate anaerobic digesters. *The ISME Journal 8*, 10 (Oct. 2014), 2015–2028.